



# Predicting the morphology of ice particles in deep convection using the super-droplet method: development and evaluation of SCALE-SDM 0.2.5-2.2.0/2.2.1

Shin-ichiro Shima<sup>1,2</sup>, Yousuke Sato<sup>3,2</sup>, Akihiro Hashimoto<sup>4</sup>, and Ryohei Misumi<sup>5</sup>

<sup>1</sup>Graduate School of Simulation Studies, University of Hyogo, Kobe, Japan

<sup>2</sup>RIKEN Center for Computational Science, Kobe, Japan

<sup>3</sup>Department of Earth and Planetary Sciences, Faculty of Science, Hokkaido University, Sapporo, Japan

<sup>4</sup>Meteorological Research Institute, Japan Meteorological Agency, Tsukuba, Japan

<sup>5</sup>National Research Institute for Earth Science and Disaster Resilience, Tsukuba, Japan

**Correspondence:** Shin-ichiro Shima (s\_shima@sim.u-hyogo.ac.jp)

**Abstract.** The super-droplet method (SDM) is a particle-based numerical scheme that enables accurate cloud microphysics simulation with lower computational demand than multi-dimensional bin schemes. Using SDM, a detailed numerical model of mixed-phase clouds is developed in which ice morphologies are explicitly predicted without assuming ice categories or mass-dimension relationships. Ice particles are approximated using porous spheroids. The elementary cloud microphysics processes considered are advection and sedimentation; immersion/condensation and homogeneous freezing; melting; condensation and evaporation including cloud condensation nuclei activation and deactivation; deposition and sublimation; collision-coalescence, -riming, and -aggregation. To evaluate the model's performance, a 2D large-eddy simulation of a cumulonimbus was conducted, and the results well capture characteristics of a real cumulonimbus. The mass-dimension and velocity-dimension relationships the model predicted show a reasonable agreement with existing formulas. Numerical convergence is achieved at a super-particle number concentration as low as 128/cell, which consumes 30 times more computational time than a two-moment bulk model. Although the model still has room for improvement, these results strongly support the efficacy of the particle-based modeling methodology to simulate mixed-phase clouds.

## Contents

1	<b>Introduction</b>	<b>4</b>
15	<b>2 Attributes of atmospheric particles</b>	<b>8</b>
	2.1 Notion of a particle . . . . .	8
	2.2 Liquid water amount . . . . .	8
	2.3 Masses of soluble and insoluble substances . . . . .	8
	2.4 Freezing temperature and ice nucleation active surface site . . . . .	8
20	2.5 Porous spheroid approximation of ice particles . . . . .	9



	2.6	Rime mass and number of monomers . . . . .	9
	2.7	Velocity . . . . .	9
	2.8	Effective number of attributes . . . . .	10
	<b>3</b>	<b>Variables for moist air</b>	<b>10</b>
5	<b>4</b>	<b>Time evolution equations of mixed-phase clouds</b>	<b>10</b>
	4.1	Cloud microphysics . . . . .	10
	4.1.1	Advection and sedimentation . . . . .	11
	4.1.2	Droplet terminal velocity . . . . .	11
	4.1.3	Ice particle terminal velocity . . . . .	11
10	4.1.4	Immersion/condensation and homogeneous freezing . . . . .	12
	4.1.5	Melting . . . . .	12
	4.1.6	Condensation and evaporation . . . . .	13
	4.1.7	Deposition and sublimation . . . . .	13
	4.1.8	Stochastic description of collision-coalescence, -riming, and -aggregation . . . . .	16
15	4.1.9	Coalescence between two droplets . . . . .	17
	4.1.10	Riming between an ice particle and a droplet . . . . .	17
	4.1.11	Aggregation between two ice particles . . . . .	20
	4.1.12	Limitations of our cloud microphysics model . . . . .	22
	4.2	Fluid dynamics of moist air . . . . .	22
20	4.3	Summary of the section . . . . .	23
	<b>5</b>	<b>Numerical schemes and implementation</b>	<b>24</b>
	5.1	Spatial discretization of moist air . . . . .	24
	5.2	Super-particles and real particles . . . . .	24
	5.3	Initialization of super-particles . . . . .	25
25	5.4	Operator splitting of the time integration . . . . .	26
	5.5	Time integration of cloud microphysics . . . . .	26
	5.5.1	Advection and sedimentation . . . . .	27
	5.5.2	Freezing and melting . . . . .	27
	5.5.3	Condensation and evaporation . . . . .	27
30	5.5.4	Deposition and sublimation . . . . .	28
	5.5.5	Collision-coalescence, -riming, and -aggregation . . . . .	28
	5.6	Time integration of moist air fluid dynamics . . . . .	28



	<b>6 Design of numerical experiments for model evaluation: 2D simulation of an isolated cumulonimbus</b>	<b>29</b>
	6.1 Control ensemble (CTRL)	29
	6.1.1 Initial moist air conditions	29
	6.1.2 Moist air boundary conditions	29
5	6.1.3 Initial conditions of particles	29
	6.1.4 Boundary conditions for particles	31
	6.1.5 Surface heating	31
	6.1.6 Grid size and time steps	32
	6.1.7 Initialization of super-particles	32
10	6.1.8 Pseudo-random numbers	33
	6.2 Other ensembles for investigating numerical convergence	33
	6.2.1 NSP ensembles for super-particle number convergence	33
	6.2.2 DX ensembles for grid convergence	33
	6.2.3 DT ensembles for time step convergence	34
15	<b>7 Typical behavior of CTRL ensemble</b>	<b>34</b>
	7.1 Hydrometeor categorization	34
	7.2 Spatial structure of the cloud, water path, and precipitation amount	35
	7.3 Ice particle morphology and fall speeds	35
	<b>8 Results of the numerical convergence tests</b>	<b>43</b>
20	8.1 NSP ensembles and super-particle number convergence	43
	8.2 DX ensembles and grid convergence	44
	8.3 DT ensembles and time step convergence	45
	<b>9 Discussions</b>	<b>47</b>
	9.1 Origins of odd particles	49
25	9.1.1 Long, slowly falling hailstones	49
	9.1.2 Columns with steep mass-dimension relationship	49
	9.1.3 Low-density hailstones	50
	9.1.4 Long graupel particles	51
	9.1.5 Results after corrections	51
30	9.2 Further sophistication of the model	51
	9.2.1 Ice nucleation pathways	57
	9.2.2 Onset of melting	58
	9.2.3 Partially frozen/melted particles	58



	9.2.4	Condensation and evaporation . . . . .	58
	9.2.5	Deposition and sublimation . . . . .	59
	9.2.6	Riming . . . . .	60
	9.2.7	Aggregation . . . . .	60
5	9.2.8	Spontaneous/collisional breakup . . . . .	61
	9.2.9	Sub-grid scale turbulence . . . . .	62
	9.3	Numerical convergence and computational cost . . . . .	62
	<b>10</b>	<b>Conclusions</b>	<b>64</b>
		<b>Appendix A: List of symbols</b>	<b>65</b>
10		<b>Appendix B: List of abbreviations</b>	<b>70</b>

## 1 Introduction

Mixed-phase clouds, which are clouds consisting of droplets and ice particles, appear under multiple atmospheric conditions, from the tropics to the poles, and throughout the year (Shupe et al., 2008). Accurately simulating the evolution of droplets and ice particles in mixed-phase clouds is crucial to understanding cloud dynamics, precipitation formation, water transport, radiative properties, aerosol-cloud interaction, cloud electrification, and lightning. These features are all crucial to many environmental and societal issues, such as climate change and variability, numerical weather prediction, weather modification, and icing on infrastructure (e.g., wind turbines and power lines) and aircraft (e.g., Korolev et al., 2017).

Through its 70-year history, numerical models of cloud microphysics have become increasingly sophisticated (e.g., Khain et al., 2015; Khain and Pinsky, 2018; Grabowski et al., 2019). However, recent model intercomparison studies have revealed that the models do not show any sign of converging toward the truth. Even the most sophisticated models do not agree well, and the divergence in model results is as large in sophisticated models as in simple models (VanZanten et al., 2011; Xue et al., 2017). Mixed-phase cloud microphysics modeling is particularly challenging because we still lack sufficient scientific understanding of mixed-phase cloud microphysics and an algorithm appropriate for mixed-phase cloud microphysics does not exist. This study aims to address the second problem.

Every numerical model is an approximation of a phenomenon’s mathematical model, which is a theoretical description that supposedly accurately expresses the system’s behavior. We apply a numerical scheme to construct a numerical model, which we use to produce an approximate solution of the phenomenon’s underlying mathematical model for given spatiotemporal boundary conditions.

There are several types of cloud microphysics numerical models, which are based on different levels of theoretical description.



The first of these is the bulk model, which is the most widely used cloud microphysics model type (e.g., Khain et al., 2015; Morrison and Milbrandt, 2015; Khain and Pinsky, 2018; Grabowski et al., 2019). Bulk models consider only the particle population's statistical features, and are thus based on macroscopic description. They solve a mathematical model that is closed in lower moments of the distribution function of cloud droplets, rain droplets, and ice particle categories (e.g., total mass and total number of particles). Currently, bulk models do not have a rigorous theoretical foundation and must rely on empirical parameterizations. A more bottom-up approach to construct more accurate and reliable numerical models would thus be desired.

Kinetic description provides a more detailed microscopic mathematical model of cloud microphysics, with the evolution and motion of individual aerosol, cloud, and precipitation particles being explicitly considered. Assuming that particles are locally well-mixed, particle collisions are regarded as a stochastic process. Each particle is characterized by its position and internal state, the latter of which is specified by variables, known as attributes, such as size, mass, aspect ratio, velocity, and chemical compositions.

Mixed-phase cloud microphysics are far more complicated than those of liquid-phase clouds, with various ice crystal formation mechanisms, diffusional growth, diverse ice particle morphologies, ice melting and shedding, spontaneous breakup, riming and wet growth, aggregation, collisional breakup, and rime splintering at play (e.g., Pruppacher and Klett, 1997; Hashino and Tripoli, 2007, 2008, 2011a, b; Khvorostyanov and Curry, 2014; Khain and Pinsky, 2018). Though our scientific understanding is not yet sufficient, it is plausible that mixed-phase cloud microphysics can be accurately described under a kinetic description framework. Indeed, direct comparison with laboratory data suggests that ice particle morphology evolution can be accurately expressed by a kinetic description (Jensen and Harrington, 2015). This is important as ice particle morphology significantly influences the fall speed, growth by diffusion and collision, and radiative properties of ice particles. Because of their direct correspondence to elementary processes, it should also be easier to refine kinetic descriptions using laboratory measurements.

Two numerical scheme types exist for kinetic descriptions: bin schemes and particle-based schemes.

The development of bin schemes started independently of bulk models in the 1950s (e.g., Khain et al., 2015; Khain and Pinsky, 2018; Grabowski et al., 2019).

Particle-based cloud microphysics modeling is a new approach that has emerged since the mid-2000s (e.g., Paoli et al., 2004; Jensen and Pfister, 2004; Shirgaonkar and Lele, 2006; Andrejczuk et al., 2008, 2010; Shima et al., 2009; Sölch and Kärcher, 2010; Riechelmann et al., 2012; Brdar and Seifert, 2018; Seifert et al., 2019; Jaruga and Pawlowska, 2018; Grabowski and Abade, 2017; Abade et al., 2018; Hoffmann et al., 2019; Grabowski et al., 2018). During particle-based modeling's early development, calculating the collision-coalescence process was a numerical challenge. Shima et al. (2009), Andrejczuk et al. (2010), Sölch and Kärcher (2010), and Riechelmann et al. (2012) proposed different algorithms, and among those four schemes, the super-droplet method (SDM) developed by Shima et al. (2009) provides a computationally efficient Monte Carlo algorithm (Unterstrasser et al., 2017; Dziekan and Pawlowska, 2017). Several other collision-coalescence algorithms have been proposed in different research areas such as the weighted flow algorithm for aerosol dynamics (DeVille et al., 2011); O'Rourke's method (1981), and the no-time counter method (Schmidt and Rutland, 2000) for spray combustion; and Ormel and Spaans's method



(2008) and Zsom and Dullemond's method (2008) for astrophysics. However, a performance comparison of these algorithms remains to be conducted.

The essential difference between bin schemes and particle-based schemes is in the representation of particles. Bin schemes adopt an Eulerian approach and the particle distribution function is approximated by a histogram. In contrast, particle-based schemes rely on a Lagrangian approach and the population of real particles is approximated using a population of weighted samples, sometimes referred to as super-droplets or super-particles. As discussed in Grabowski et al. (2019), bin schemes face problems that are difficult to overcome such as numerical diffusion, computational cost (curse of dimensionality), and the breakdown of the Smoluchowski equation (Smoluchowski, 1916). However, SDM can resolve, or at least mitigate, those problems.

Therefore, SDM and similar particle-based schemes should be more suitable for mixed-phase cloud microphysics simulations than bin schemes. Mainly because of computational costs, it is practically impossible to apply bin schemes to the most comprehensive form of kinetic description, which inevitably involves multiple attributes to express each particle's internal state. Instead, many existing bin models solve a simplified kinetic description that uses particle distribution functions with a one-dimensional attribute space approximation. For example, most rely on artificially separated categories of ice particles, with predefined mass-dimension and area-dimension relationships in each category. Another approach is adopted in the SHIPS model developed by Hashino and Tripoli (2007, 2008, 2011a, b), which is a bin model that solves sophisticated and comprehensive kinetic description and does not use ice categories or mass-dimension relationships. However, to justify using the one-dimensional particle distribution function, they rely on an "implicit mass sorting assumption" that states that different solid hydrometeor species do not belong to the same bin because they are naturally sorted by mass. Such simplifications can be a significant source of errors. SDM and similar particle-based schemes should be able to directly simulate comprehensive kinetic descriptions with lower computational demand.

This study's primary objective is to assess particle-based modeling methodology's capability to simulate mixed-phase clouds. For this purpose, we develop and evaluate the performance of a detailed numerical mixed-phase cloud model using SDM, in which ice particle morphologies are explicitly predicted.

We first construct a mixed-phase cloud microphysics mathematical model, which is based on kinetic description. The fluid dynamics of moist air is described by the compressible Navier-Stokes equation and aerosol, cloud, and precipitation particles are represented by point particles. Following Chen and Lamb (1994a, b) and Misumi et al. (2010), ice particles are approximated using porous spheroids. The elementary cloud microphysics processes considered in the model are advection and sedimentation; immersion/condensation and homogeneous freezing; melting; condensation and evaporation including the cloud condensation nuclei (CCN) activation and deactivation; deposition and sublimation; and collision-coalescence, -riming, and -aggregation. The mathematical models used for those elementary processes are based on revised versions of existing formulas. Additionally, our model does not rely on ice categories or predefined mass-dimension relationships. For simplicity, and because of lack of appropriate algorithms, we do not consider spontaneous/collisional breakup or rime splintering. We then develop a numerical model called SCALE-SDM to solve the mathematical model. Mixed-phase cloud microphysics are solved using the SDM and the fluid dynamics of moist air is solved fully explicitly using a finite volume method with an



Arakawa-C staggered grid. To evaluate our model's performance, we conduct a two-dimensional (2D) simulation of an isolated cumulonimbus, and find that the results well capture characteristics of a real cumulonimbus. The mass-dimension and velocity-dimension relationships our model predicts show a reasonable agreement with existing formulas based on laboratory measurements and field observations. We also investigate the simulation's numerical convergence and confirm that our model can produce an accurate approximate solution with lower computational demand than multi-dimensional bin schemes. We then explore the possibility of further refining and sophisticating the model; however, advancing our understanding of mixed-phase cloud microphysics is beyond the scope of this study.

Several previous works are closely relevant to this study. Chen and Lamb (1994a, b) developed a detailed multi-dimensional bin model, which Misumi et al. (2010) extended and added ice volume as a new particle attribute. We follow that strategy and approximate ice particles as porous spheroids; however, their kinetic description is more detailed than ours as they also considered spontaneous/collisional breakup, shedding, rime splintering, and surface chemical reactions. They solved the model using a multi-dimensional bin scheme, hence their numerical model carries a high computational cost. Hashino and Tripoli (2007, 2008, 2011a, b) further extended Chen and Lamb (1994a, b)'s kinetic description to account for polycrystals that can form below  $-20^{\circ}\text{C}$ . They solve the mathematical model using a one-dimensional bin scheme; however, careful validation is needed to justify their "implicit mass sorting assumption". Paoli et al. (2004), Jensen and Pfister (2004), and Shirgaonkar and Lele (2006) separately developed a particle-based model for ice-phase clouds, but neither the evolution of ice particle morphologies nor the aggregation of ice particles were considered in their models. Sölch and Kärcher (2010) also developed a particle-based model for ice-phase clouds, but that model relies on ice categories and mass-dimension relationships. Brdar and Seifert (2018) developed McSnow, the first particle-based model for mixed-phase clouds. McSnow is a multidimensional expansion of the P3 bulk model (Morrison and Milbrandt, 2015; Milbrandt and Morrison, 2016), and thus free from ice categories; however, it still relies on mass-dimension relationships. Further, a kinetic approach is applied to ice particles, but not droplets or aerosol particles.

In this study we demonstrate that a large-eddy simulation of a cumulonimbus that predicts ice particle morphologies without assuming ice categories or mass-dimension relationships is possible if we use SDM. Future studies to advance the understanding of elementary mixed-phase cloud microphysics processes are desired, as such knowledge can be directly incorporated into particle-based cloud models.

The organization of the remainder of this paper is as follows. In Secs. 2–4, our mixed-phase cloud mathematical model is described in detail. Cloud microphysics is based on kinetic description and is coupled with moist air fluid dynamics. Note that this model is an expansion of Shima et al. (2009)'s warm cloud model. In Sec. 5, we develop a numerical model, called SCALE-SDM, by applying SDM. To evaluate SCALE-SDM's performance, we conduct a 2D simulation of an isolated cumulonimbus. Sec. 6 presents the design of the numerical experiments, and in Sec. 7, the overall properties of the simulated cumulonimbus and ice particle morphologies are analyzed. The numerical convergence characteristics of the model are investigated in Sec. 8. In Sec. 9, possible improvements of the model are discussed and a summary and conclusions are presented in Sec. 10. Lastly, list of symbols and abbreviations are provided in Appendixes A and B, respectively.



## 2 Attributes of atmospheric particles

### 2.1 Notion of a particle

Let us represent aerosol, cloud, and precipitation particles as point particles. Particle state is then characterized by two types of variables: position  $\boldsymbol{x}$  and attributes  $\boldsymbol{a}$ . Attributes consist of several variables representing the particle's internal state, and the attributes considered in this study are  $\boldsymbol{a} = \{r, \{m_{\alpha}^{\text{sol}}\}, \{m_{\beta}^{\text{insol}}\}, T^{\text{fz}}, a, c, \rho^i, m^{\text{rime}}, n^{\text{mono}}, \boldsymbol{v}\}$ , i.e., liquid water amount, masses of soluble substances, masses of insoluble substances, freezing temperature, equatorial radius, polar radius, apparent density, rime mass, number of monomers, and velocity.

In the remainder of this section, we provide a detailed explanation of each attribute.

### 2.2 Liquid water amount

The amount of liquid water contained in a particle is expressed by the volume-equivalent sphere's radius  $r$ . That is, the volume of water in a particle is  $(4/3)\pi r^3$ .

### 2.3 Masses of soluble and insoluble substances

Let  $m_{\alpha}^{\text{sol}}, \alpha = 1, 2, \dots, N^{\text{sol}}$  be the masses of soluble substances contained in the particle, and let  $m_{\beta}^{\text{insol}}, \beta = 1, 2, \dots, N^{\text{insol}}$  be the masses of insoluble substances.

### 2.4 Freezing temperature and ice nucleation active surface site

We only consider homogeneous freezing and condensation/immersion freezing in this study because these are dominant in mixed-phase clouds (e.g., Cui et al., 2006; De Boer et al., 2011; Murray et al., 2012).

Based on the “singular hypothesis” (Levine, 1950), we consider that each insoluble particle has its own freezing temperature  $T^{\text{fz}}$ , and that a supercooled droplet freezes as soon as the ambient temperature  $T$  decreases below  $T^{\text{fz}}$ . The freezing process is described in detail in Sec. 4.1.4.

When particles  $j$  and  $k$  collide and coalesce, rime, or aggregate, we assume that the new particle's  $T^{\text{fz}}$  is given by  $\max(T_j^{\text{fz}}, T_k^{\text{fz}})$ , i.e., the higher freezing temperature of the two constituent particles.

A particle's  $T^{\text{fz}}$  is directly connected to the ice nucleation active surface site (INAS) density concept (e.g., Fletcher, 1969; Connolly et al., 2009; Niemand et al., 2012; Hoose and Möhler, 2012).

An INAS is a localized structure, such as lattice mismatches, cracks, and hydrophilic sites, on an insoluble substance's surface that catalyzes ice formation at temperatures lower than a specific temperature. INAS density  $n_{\text{S}}(T)$  gives the accumulated number of INAS per unit surface area of the insoluble substance. Therefore,  $n_{\text{S}}(T)$  is a function that increases as  $T$  decreases. The freezing temperature  $T^{\text{fz}}$  corresponds to the highest temperature at which the first INAS appears on the insoluble substance's surface. Let  $A^{\text{insol}}$  be the insoluble substance's surface area. Then, the probability that  $T^{\text{fz}}$  is larger than  $T$  can be



calculated as  $P(T^{\text{fz}} > T) = 1 - \exp[-A^{\text{insol}}n_S(T)]$ . The probability density function of  $T^{\text{fz}}$  then becomes

$$p(T) = -\frac{dP(T^{\text{fz}} > T)}{dT} = -A^{\text{insol}}\frac{dn_S}{dT}e^{-A^{\text{insol}}n_S}. \quad (1)$$

We can determine  $T^{\text{fz}}$  by selecting a random number using this probability distribution.

For mineral dust, biogenic substances, and soot, we can use the INAS density formulas of Niemand et al. (2012), Wex et al. (2015), and Ullrich et al. (2017), respectively. If a particle consists of multiple insoluble substances, we assume that  $T^{\text{fz}}$  is the highest of all.

It is possible that a single INAS does not appear until  $-38^\circ\text{C}$ , meaning that the particle is ice nucleation (IN) inactive and will not freeze by immersion/condensation freezing and only by homogeneous freezing. To account for this, we set  $T^{\text{fz}} = -38^\circ\text{C}$ . If a particle contains only soluble substances, we also set  $T^{\text{fz}} = -38^\circ\text{C}$ .

There are various ice nucleation pathways (e.g., Kanji et al., 2017); however, in this study we do not consider other ice nucleation pathways, such as deposition nucleation, deliquescent freezing, pore freezing, and contact freezing. The possibility of extending our model to incorporate these mechanisms is discussed in Sec. 9.2.1.

## 2.5 Porous spheroid approximation of ice particles

Ice particles have diverse morphologies such as columns, hexagonal plates, dendrites, rimed crystals, graupel, hailstones, and aggregates (e.g., Magono and Lee, 1966; Kikuchi et al., 2013). Following the strategies of Chen and Lamb (1994a, b), Misumi et al. (2010), and Jensen and Harrington (2015), let us approximate each ice particle as a porous spheroid, which is characterized by three variables: equatorial radius  $a$ , polar radius  $c$ , and apparent density  $\rho^i$ . That is, the ice particle's apparent volume is  $V = (4\pi/3)a^2c$  and its mass can be evaluated as  $m = \rho^iV$ . The two radii  $a$  and  $c$  represent the ice particle's spatial extent and  $\rho^i$  represents its internal structure. Let us define the aspect ratio as  $\phi := c/a$ . A spheroid is considered a prolate spheroid if  $\phi > 1$ , and columns can be approximated by prolate spheroids. In contrast, plates and dendrites are approximated by oblate spheroids, i.e.,  $\phi < 1$ . If an ice particle is hollowed out or intricately branched,  $\rho^i$  becomes smaller than the ice crystal's true density  $\rho_{\text{true}}^i \approx 916.8\text{kg/m}^3$ .

## 2.6 Rime mass and number of monomers

Following Brdar and Seifert (2018) we introduce two additional ice particle attributes: rime mass  $m^{\text{rime}}$  and number of monomers  $n^{\text{mono}}$ . Rime mass  $m^{\text{rime}}$  records the mass of ice a particle has obtained through the riming process. Number of monomers  $n^{\text{mono}}$  is an integer representing the number of primary ice crystals in the particle. In this study,  $m^{\text{rime}}$  and  $n^{\text{mono}}$  are used only for analyzing simulation results. Unlike the McSnow model of Brdar and Seifert (2018), this study's time evolution equations do not depend on  $m^{\text{rime}}$  or  $n^{\text{mono}}$ , as will be detailed in Sec. 4.1.

## 2.7 Velocity

We consider that each particle is always moving at its terminal velocity. Therefore, a particle's velocity  $v$  is a diagnostic attribute.



## 2.8 Effective number of attributes

In summary, particle attributes consist of  $\mathbf{a} = \{r, \{m_\alpha^{\text{sol}}\}, \{m_\beta^{\text{insol}}\}, T^{\text{fz}}, a, c, \rho^i, m^{\text{rime}}, n^{\text{mono}}, \mathbf{v}\}$ . We need the mass of insoluble substances  $\{m_\beta^{\text{insol}}, \beta = 1, 2, \dots, N^{\text{insol}}\}$  (and corresponding INAS densities) to specify freezing temperature  $T^{\text{fz}}$ . However, as described in Sec. 4.1, time evolution equations do not depend on  $\{m_\beta^{\text{insol}}\}$ . Rime mass  $m^{\text{rime}}$  and number of monomers  $n^{\text{mono}}$  do not affect time evolution either. Particle velocity  $\mathbf{v}$  is a diagnostic attribute. Therefore, the attributes directly relevant to time evolution can be reduced to  $\{r, \{m_\alpha^{\text{sol}}\}, T^{\text{fz}}, a, c, \rho^i\}$ . Compared to the warm cloud SDM model of Shima et al. (2009), four new attributes are introduced.

Note that either the equivalent droplet radius  $r$  or ice particle attributes  $\{a, c, \rho^i\}$  are always zero in our model as we assume that each particle completely freezes or melts instantaneously (see Secs. 4.1.4 and 4.1.5). However, we assume that all particles contain soluble substances and are always deliquescent even when the humidity is low, thus both cannot be simultaneously zero (see Sec. 4.1.6).

## 3 Variables for moist air

We only consider dry air and water vapor for the gas phase and ignore other trace gases. In this section, we introduce several variables that describe the state of moist air: wind velocity  $\mathbf{U} = (U, V, W)$ , density of dry air  $\rho_d$ , density of water vapor  $\rho_v$ , density of moist air  $\rho := \rho_d + \rho_v$ , specific humidity  $q_v := \rho_v / \rho$ ,  $q_d := \rho_d / \rho$ , temperature  $T$ , pressure  $P$ , and potential temperature of moist air  $\theta := T / \Pi := T / (P / P_0)^{R / c_p}$ . Here,  $P_0 = 1000$  hPa is a reference pressure;  $R_d$ ,  $R_v$ , and  $R := q_d R_d + q_v R_v$  are the gas constants of dry air, water vapor, and moist air, respectively; and  $c_{pd}$ ,  $c_{pv}$ , and  $c_p := q_d c_{pd} + q_v c_{pv}$  are the isobaric specific heats of dry air, water vapor, and moist air, respectively. To simplify notation, we introduce a variable representing the state of moist air:  $\mathbf{G} = \{\mathbf{U}, \rho, q_v, \theta, P, T\}$ .

## 4 Time evolution equations of mixed-phase clouds

In this section we describe our model's time evolution equations, first from cloud microphysics and then moist air fluid dynamics.

### 4.1 Cloud microphysics

Let us assign a unique index  $i$  to each particle. This section explains the time evolution equations of particles  $\{\{\mathbf{x}_i(t), \mathbf{a}_i(t)\}, i = 1, 2, \dots, N_r^{\text{WP}}\}$ . Here,  $N_r^{\text{WP}}$  represents the total number of particles accumulated over the whole period. However, because of coalescence, precipitation, and other processes, some particles may not exist all the time, thus we let  $I_r(t)$  be the set of particle indices existing in the domain at time  $t$ .



#### 4.1.1 Advection and sedimentation

Particle  $i$ 's motion equation is

$$\frac{d}{dt}(m_i \mathbf{v}_i) = \mathbf{F}_i^{\text{drg}} - m_i g \hat{\mathbf{z}}, \quad \frac{d\mathbf{x}_i}{dt} = \mathbf{v}_i, \quad (2)$$

where  $m_i$  is the particle's mass,  $\mathbf{F}_i^{\text{drg}}$  is the force of drag from moist air,  $g$  is Earth's gravity, and  $\hat{\mathbf{z}}$  is the unit vector in the  $z$  axis direction. Note that  $-\mathbf{F}_i^{\text{drg}}$  gives the reaction force acting on moist air. The momentum of moist air changes following Eqs. (72) and (80).

If terminal velocity is instantaneously reached, the motion equation becomes

$$\mathbf{v}_i = \mathbf{U}_i - \hat{\mathbf{z}} v_i^\infty, \quad \frac{d\mathbf{x}_i}{dt} = \mathbf{v}_i, \quad (3)$$

where  $\mathbf{U}_i := \mathbf{U}(\mathbf{x}_i)$  is the  $i$ -th particle's ambient wind velocity and  $v_i^\infty$  is the terminal velocity, which is generally a function of attributes  $\mathbf{a}_i$  and the state of the ambient air  $\mathbf{G}_i$ . The next two subsections explain the formulas used to calculate droplet and ice particle terminal velocities.

#### 4.1.2 Droplet terminal velocity

To calculate droplet terminal velocity, we use the formula of Beard (1976):  $v_i^\infty = v_{\text{Beard}}^\infty(\min(r_i, 3.5\text{mm}); \rho_i, P_i, T_i)$ , where  $\rho_i := \rho(\mathbf{x}_i)$  and  $P_i := P(\mathbf{x}_i)$  are the density and pressure of ambient moist air, respectively. This formula is applicable to droplets with radii smaller than 3.5 mm. If we use the formula for droplets larger than this, fall speed becomes unrealistically fast. Therefore, we use the fall speed of a droplet with a 3.5 mm radius for droplets larger than the size limit.

#### 4.1.3 Ice particle terminal velocity

For ice particle terminal velocity, we use the formula of Böhm (1989, 1992c, 1999):  $v_i^\infty = v_{\text{Böhm}}^\infty(m_i, \phi_i, D_i, A_i, A_i^{\text{cc}}; \rho_i, T_i)$ , where  $D_i$  is the maximum dimension,  $A_i$  is projected area perpendicular to the flow direction, and  $A_i^{\text{cc}}$  is the area of the circumcircle of  $A_i$ , i.e., the area of the smallest circle that completely contains  $A_i$ .

The maximum dimension can be calculated as  $D_i = 2 \max(a_i, c_i)$ . We assume that ice particles are falling with their maximum dimension perpendicular to the flow direction, therefore the circumcircle area becomes  $A_i^{\text{cc}} = \pi \max(a_i, c_i)^2$ . Projected area  $A_i$  can be roughly evaluated by the area of circumscribed ellipse  $A_i^{\text{ce}} = \pi a_i \max(a_i, c_i)$ ; however, we must subtract pores and indentations at boundaries from  $A_i^{\text{ce}}$ . We assume that the ratio  $A_i/A_i^{\text{ce}}$  is a power of the volume fraction  $\rho_i^i/\rho_{\text{true}}^i$ , and that the exponent  $\kappa$  is a function of the aspect ratio  $\phi_i$ :

$$A_i = A_i^{\text{ce}} \left( \frac{\rho_i^i}{\rho_{\text{true}}^i} \right)^{\kappa(\phi_i)}. \quad (4)$$

Based on the following arguments, we propose a value  $\kappa$  of the form

$$\kappa(\phi_i) = \exp(-\phi_i). \quad (5)$$



Following Jensen and Harrington (2015), we assume  $\kappa \rightarrow 1$  as  $\phi_i \rightarrow 0$ , and  $\kappa \rightarrow 0$  as  $\phi_i \rightarrow \infty$ .  $\phi_i \ll 1$  means that the ice particle is thin and extends horizontally. Therefore, we can expect that the structure is uniform along the vertical axis and that the ratio  $A_i/A_i^{\text{ce}}$  is equal to the volume fraction  $\rho_i^i/\rho_{\text{true}}^i$ . Thus,  $\kappa(\phi_i = 0) = 1$ . At the other extreme,  $\phi_i \gg 1$  indicates that the ice particle is columnar. Such ice crystals typically hollow inward along their basal face; therefore, the volume fraction  $\rho_i^i/\rho_{\text{true}}^i$  will not affect the ratio  $A_i/A_i^{\text{ce}}$ . Thus,  $\kappa(\phi_i \rightarrow \infty) = 0$ .

For  $\phi_i \approx 1$ , Jensen and Harrington (2015) argued that  $(\rho_i^i/\rho_{\text{true}}^i)^\kappa = 1$ , i.e.,  $\kappa = 0$ . However, this cannot be justified for aggregates with low apparent density. Thus, we estimate  $\kappa$  through a dimensional analysis. We assume that the power laws  $m_i \propto D_i^\beta$  and  $A_i \propto D_i^{\beta/s}$  hold good. Thus, by the definition of apparent density,  $\rho_i^i = m_i/((4/3)\pi a_i^2 c_i) \propto D_i^{\beta-3}$ . From Eq. (4),  $D_i^{\beta/s} = D_i^2 D_i^{(\beta-3)\kappa}$ . Hence,  $\kappa = (2s - \beta)/\{s(3 - \beta)\}$  holds. Schmitt and Heymsfield (2010) estimated that  $(\beta, s) = (2.22, 1.32)$  for aggregates observed during the Cirrus Regional Study of Tropical Anvils and Cirrus Layers–Florida Area Cirrus Experiment (CRYSTAL-FACE) field project. Therefore,  $\kappa = 0.375$  for CRYSTAL-FACE aggregates. They also estimated that  $(\beta, s) = (2.22, 1.32)$  for aggregates observed during an Atmospheric Radiation Measurement (ARM) field project, which results in  $\kappa = 0.300$ .

The  $\kappa$  given by Eq. (5) yields  $\kappa(0) = 1$ ,  $\kappa(1) = 0.368$ , and  $\kappa(\infty) = 0$ , which agree with the aforementioned estimation.

#### 4.1.4 Immersion/condensation and homogeneous freezing

As explained in Sec. 2.4, a supercooled droplet freezes when the ambient temperature drops below its freezing temperature. This section provides a more precise description of when and how freezing occurs in our model.

We consider that the  $i$ -th particle freezes immediately when the following three conditions are all satisfied: (1) The particle is a droplet, i.e.,  $r_i > 0$ ; (2) ambient water vapor is supersaturated over liquid water, i.e.,  $e_i > e_s^w(T_i)$ ; and (3) ambient temperature is colder than the particle's freezing temperature, i.e.,  $T_i < T_i^{\text{fz}}$ . Here,  $e_i := e(\mathbf{x}_i)$  and  $T_i := T(\mathbf{x}_i)$  are the ambient vapor pressure and temperature of the  $i$ -th particle, respectively, and  $e_s^w(T)$  is the saturation vapor pressure over a planar liquid water surface at temperature  $T$ .

We assume that the resulting ice crystal is spherical, with the true ice crystal density  $\rho_{\text{true}}^i$ . Therefore, attributes are updated as follows:  $r_i' = 0$ ,  $a_i' = c_i' = r_i(\rho^w/\rho_{\text{true}}^i)^{1/3}$ ,  $\rho_i^i' = \rho_{\text{true}}^i$ ,  $n_i^{\text{monof}} = 1$ , and  $m_i^{\text{rimedf}} = 0$ . The primed variables here denote values after the update, and  $\rho^w$  is the density of liquid water.  $\{m_{\alpha i}^{\text{sol}}\}$ ,  $\{m_{\beta i}^{\text{insol}}\}$ , and  $T_i^{\text{fz}}$  remain unchanged.

When freezing occurs, each particle releases latent heat of fusion to the moist air as indicated in Eqs. (73), (78), and (79).

#### 4.1.5 Melting

When ambient temperature rises above  $0^\circ\text{C}$ , we consider that melting occurs immediately. Thus, the attributes are updated as follows:  $r_i' = (a_i^2 c_i \rho_i^i/\rho^w)^{1/3}$  and  $a_i' = c_i' = \rho_i^i' = n_i^{\text{monof}} = m_i^{\text{rimedf}} = 0$ .  $\{m_{\alpha i}^{\text{sol}}\}$ ,  $\{m_{\beta i}^{\text{insol}}\}$ , and  $T_i^{\text{fz}}$  remain unchanged. When melting occurs, each particle absorbs latent heat of fusion from the moist air as indicated in Eqs. (73), (78), and (79).



#### 4.1.6 Condensation and evaporation

Following, e.g., Rogers and Yau (1989), the time evolution equation describing droplet growth by condensation/evaporation can be derived as follows.

The growth rate is identical to vapor flux at the droplet surface. If the diffusion of vapor around the droplet is in a quasi-steady state, we obtain

$$\frac{dm_i}{dt} = 4\pi r_i D_v (\rho_{vi} - \rho_{vi}^{\text{sfc}}). \quad (6)$$

Here,  $D_v$  is water vapor's diffusivity in air,  $\rho_{vi} := \rho_v(\mathbf{x}_i)$  is the ambient moist air's water vapor density, and  $\rho_{vi}^{\text{sfc}}$  is water vapor density at the surface of the droplet.

If we further assume that thermal diffusion is also in a quasi-steady state, and that surface temperature  $T_i^{\text{sfc}}$  and ambient temperature  $T_i$  are close to each other, i.e.,  $(T_i^{\text{sfc}} - T_i)/T_i \ll 1$ , Eq. (6) can be reduced to

$$r_i \frac{dr_i}{dt} = \frac{1}{\rho^w (F_k^w + F_d^w)} \left\{ S_i^w - \frac{e_{si}^{\text{w,eff}}}{e_s^w(T_i)} \right\}, \quad (7)$$

where  $S_i^w := e_i/e_s^w(T_i)$  is the ambient saturation ratio over liquid water, and

$$F_k^w = \left( \frac{L_v}{R_v T_i} - 1 \right) \frac{L_v}{k T_i}, \quad F_d^w = \frac{R_v T_i}{D_v e_s^w(T_i)}, \quad (8)$$

Where  $L_v$  is the latent heat of vaporization,  $k$  is the thermal conductivity of moist air, and  $e_{si}^{\text{w,eff}}$  is the effective saturation vapor pressure with respect to the  $i$ -th droplet's surface. Following Köhler's theory (Köhler, 1936),  $e_{si}^{\text{w,eff}}$  can be derived as

$$\frac{e_{si}^{\text{w,eff}}}{e_s^w(T_i)} = 1 + \frac{a(T_i)}{r_i} - \frac{b(\{m_{\alpha i}^{\text{sol}}\})}{r_i^3}, \quad (9)$$

where  $a \approx 3.3 \times 10^{-5} \text{ cm K}/T_i$ ,  $b \approx 4.3 \text{ cm}^3 \sum_{\alpha} I_{\alpha} m_{\alpha i}^{\text{sol}}/M_{\alpha}^{\text{sol}}$ ,  $I_{\alpha}$  is the van't Hoff factor which represents the degree of ionic dissociation, and  $M_{\alpha}^{\text{sol}}$  is the molecular weight of the solute  $\alpha$ . The second and third terms of Eq. (9) account for curvature and solute effects, respectively.

The growth of a droplet by condensation/evaporation is governed by Eqs. (7)-(9). It is worth noting that those equations also describe the respective activation and deactivation of cloud droplets from and to aerosol particles (see, e.g., Arabas and Shima, 2017; Hoffmann, 2017; Abade et al., 2018).

Vapor and latent heat couplings to moist air through condensation and evaporation are calculated by Eqs. (70), (71), (73), (75), (76), and (78).

#### 4.1.7 Deposition and sublimation

The shapes of ice crystals formed by depositional growth exhibit strong dependencies on temperature and, to a lesser extent, supersaturation (e.g., Nakaya, 1954; Hallett and Mason, 1958; Kobayashi, 1961). The former is known as the primary growth habit and the latter as the secondary growth habit. The primary growth habit determines the preferred growth direction, i.e.,



columnar or planar, and the secondary growth habit determines the mode of growth, i.e., whether the columnar crystal becomes solid or hollow, whether the planar crystal becomes plate-like, sectorized, or dendritic, and so on. In this study, we use the model of Chen and Lamb (1994a) with various modifications.

The mass growth rate can be derived like Eqs. (6) and (7):

$$5 \quad \frac{dm_i}{dt} = 4\pi C D_v (\rho_{v_i} - \rho_{v_i}^{\text{sfc}}) \bar{f}_{\text{vnt}} = 4\pi C \frac{S_i^i - 1}{F_k^i + F_d^i} \bar{f}_{\text{vnt}}, \quad (10)$$

where  $S_i^i := e_i / e_s^i(T_i)$  is the ambient saturation ratio over ice and  $e_s^i(T)$  is the saturation vapor pressure over ice at temperature  $T$ ,

$$F_k^i = \left( \frac{L_s}{R_v T_i} - 1 \right) \frac{L_s}{k T_i}, \quad F_d^i = \frac{R_v T_i}{D_v e_s^i(T_i)}, \quad (11)$$

where  $L_s$  is the latent heat of sublimation,  $C = C(a_i, c_i)$  is the electric capacitance of the spheroid, and  $\bar{f}_{\text{vnt}}$  is the ventilation  
 10 coefficient.

The exact form of capacitance  $C(a_i, c_i)$  is given, e.g., by Chen and Lamb (1994a).  $C \approx (2a_i + c_i)/3$  gives a good approximation for  $\phi_i \approx 1$ .

When an ice particle falls through the air, the flow around it enhances diffusional growth, a phenomenon known as the ventilation effect, which is accounted for by the coefficient  $\bar{f}_{\text{vnt}}$ . Hall and Pruppacher (1976) suggested that  $\bar{f}_{\text{vnt}}$  can be  
 15 described by

$$\bar{f}_{\text{vnt}} = b_1 + b_2 X^\gamma, \quad (12)$$

where  $(b_1, b_2, \gamma) = (1.0, 0.14, 2)$  for  $X \leq 1$ ,  $(b_1, b_2, \gamma) = (0.86, 0.28, 1)$  for  $X > 1$ ,  $X = N_{\text{Sc}}^{1/3} (N_{\text{Rei}}^i)^{1/2}$ ,  $N_{\text{Sc}} = \mu / (\rho D_v)$  is the Schmidt number,  $N_{\text{Rei}}^i = \rho v_i^\infty D_i / \mu$  is the Reynolds number of ice particle  $i$ , and  $\mu$  is the dynamic viscosity of moist air.

Note that  $m_i$  in Eq. (10) can become negative through sublimation over a finite time. Therefore, we impose a limiter to  $dm_i$   
 20 as follows:

$$dm_i = \max(dm_i, m_{\text{min}}^i - m_i), \quad (13)$$

where  $m_{\text{min}}^i$  is an arbitrary small mass taken from the mass of a spherical ice particle with radius 1 nm and the true ice density  $\rho_{\text{true}}^i$ .

In Chen and Lamb's (1994a) model, the primary growth habit is expressed by an empirical function known as the inherent  
 25 growth ratio  $\Gamma(T)$ , which modulates the  $c$ -axis to  $a$ -axis growth rate ratio:

$$\frac{dc_i}{da_i} = \Gamma(T_i) f_{\text{vnt}} \frac{c_i}{a_i} =: \Gamma^* \frac{c_i}{a_i}, \quad (14)$$

where  $f_{\text{vnt}}$  is the primary growth habit's ventilation coefficient and  $\Gamma^*$  is the effective inherent growth ratio including the ventilation effect.

For purely diffusional growth,  $dc_i/da_i = c_i/a_i$  holds; therefore, the aspect ratio does not change, i.e.,  $d\phi_i = 0$ .  $\Gamma(T)$  repre-  
 30 sents the lateral redistribution of vapor on ice crystal surface through kinetic processes. We use the  $\Gamma(T)$  proposed by Chen



and Lamb (1994a), but set  $\Gamma(T) = 1$  for  $D < 10\mu\text{m}$  as observations suggest that ice crystals are quasi-spherical if  $D < 60\mu\text{m}$  (Baran, 2012; Korolev and Isaac, 2003; Lawson et al., 2008). Additionally, the  $\Gamma(T)$  provided in Chen and Lamb (1994a) is for temperatures between  $-30^\circ\text{C}$  and  $0^\circ\text{C}$ . For colder temperature, we simply assume

$$\Gamma(T) = \Gamma(-30^\circ\text{C}) \approx 1.28, \quad \text{for } T < -30^\circ\text{C}. \quad (15)$$

- 5 Ventilation coefficient  $f_{\text{vnt}}$  represents the preferential enhancement of vapor flux toward the ice crystal's major axis due to air flow around it. Chen and Lamb (1994a) derived a  $f_{\text{vnt}}$  of the form

$$f_{\text{vnt}} = \frac{b_1 + b_2 X^\gamma (c_i/C)^{1/2}}{b_1 + b_2 X^\gamma (a_i/C)^{1/2}}. \quad (16)$$

The secondary growth habit is expressed by deposition density  $\rho_{\text{dep}}$ , which represents the apparent density of the ice fraction newly created by deposition. Then, the change in ice particle volume  $dV_i$  is given by

$$10 \quad dV_i = \frac{dm_i}{\rho_{\text{dep}}}, \quad \text{for } dm_i \geq 0 \text{ (deposition)}. \quad (17)$$

Deposition density  $\rho_{\text{dep}}$  can be expressed as

$$\rho_{\text{dep}} = \begin{cases} \rho_{\text{true}}^i, & \text{for } \Gamma(T_i) < 1 \wedge a_i < 100\mu\text{m}; \\ \rho_{\text{dep}}^{\text{CL94}}, & \text{otherwise.} \end{cases} \quad (18)$$

Here, following Jensen and Harrington (2015), we assume that planar crystal branching does not occur if the equatorial radius  $a_i$  is smaller than  $100\mu\text{m}$ .  $\rho_{\text{dep}}^{\text{CL94}}$  is an empirical formula of deposition density proposed by Chen and Lamb (1994a),

$$15 \quad \rho_{\text{dep}}^{\text{CL94}} = \rho_{\text{true}}^i \exp \left[ -\frac{3 \max(\Delta\rho_i - 0.05 \text{ g m}^{-3}, 0)}{\Gamma(T_i) \text{ g m}^{-3}} \right], \quad (19)$$

where  $\Delta\rho_i := \rho_{vi} - \rho_{vi}^{\text{sfc}}$ . From Eq. (10),  $\Delta\rho_i$  becomes

$$\Delta\rho_i = \frac{S_i^i - 1}{D_v(F_k^i + F_d^i)}. \quad (20)$$

Here, following Miller and Young (1979), we limit  $\rho_{vi}$  by water saturation and replace the  $\Delta\rho_i$  in (19) with

$$(\Delta\rho_i)^\downarrow = \frac{\min(S_i^i, e_s^w(T_i)/e_s^i(T_i)) - 1}{D_v(F_k^i + F_d^i)}. \quad (21)$$

- 20 For sublimation, particle volume change  $dV_i$  is given by

$$dV_i = \frac{dm_i}{\rho_{\text{sbl}}}, \quad \text{for } dm_i < 0 \text{ (sublimation)}, \quad (22)$$

where sublimation density  $\rho_{\text{sbl}}$  represents the apparent density of the ice fraction removed by sublimation. For simplicity, we assume that the ice particle's apparent density will not be changed through sublimation, i.e.,

$$\rho_{\text{sbl}} = \rho_i^i. \quad (23)$$



We can now calculate attributes at time  $t + dt$ . The apparent density becomes

$$\rho_i^i(t + dt) = \frac{m_i + dm_i}{V_i + dV_i}, \quad (24)$$

where  $dm_i$  is given in Eqs. (10) and (13) and  $dV_i$  is given in Eqs. (17) and (22).

From Eq. (14) and the definition of volume  $V_i = (4\pi/3)a_i^2 c_i$ , after  $dt$ , the two radii become

$$5 \quad a_i(t + dt) = a_i \exp\left(\frac{d \log V_i}{2 + \Gamma^*}\right), \quad (25)$$

$$c_i(t + dt) = c_i \exp\left(\frac{\Gamma^* d \log V_i}{2 + \Gamma^*}\right). \quad (26)$$

Applying those equations to a small ice particle's sublimation results in the creation of a very small planar or columnar ice particle. However, observations suggest that ice crystals are quasi-spherical if  $D < 60 \mu\text{m}$  (Baran, 2012; Korolev and Isaac, 2003; Lawson et al., 2008). Therefore, we regard the ice particle as spherical with the true ice density if the minor axis predicted by Eqs. (25) and (26) is smaller than  $1 \mu\text{m}$ . That is, if  $\min\{a_i(t + dt), c_i(t + dt)\} < 1 \mu\text{m}$ ,

$$\rho_i^{i'}(t + dt) = \rho_{\text{true}}^i, \quad (27)$$

$$a_i'(t + dt) = c_i'(t + dt) = \left(\frac{m_i + dm_i}{(4\pi/3)\rho_i^{i'}(t + dt)}\right)^{\frac{1}{3}}, \quad (28)$$

where primed variables indicate values after correction.

For simplicity we assume that the rime mass fraction does not change through sublimation, following Brdar and Seifert (2018):

$$m_i^{\text{rime}}(t + dt) = \begin{cases} m_i^{\text{rime}}, & \text{for } dm_i \geq 0; \\ m_i^{\text{rime}} \frac{m_i + dm_i}{m_i}, & \text{for } dm_i < 0. \end{cases} \quad (29)$$

Vapor and latent heat couplings to moist air through deposition and sublimation are calculated by Eqs. (70), (71), (73), (75), (77), and (78).

In this section, we detailed the deposition and sublimation model used in SCALE-SDM; however, there is significant room for improvement. For example, as we will discuss in Sec. 9.1.4, the use of  $\Gamma(T)$  for sublimation is questionable. Instead, we propose using  $\Gamma(T) = 1$  for sublimation (Eq.98)). We will validate this correction in Sec. 9.1.5, and several other issues of our deposition/sublimation model, such as the representation of polycrystals, will be discussed in Sec. 9.2.5.

#### 4.1.8 Stochastic description of collision-coalescence, -riming, and -aggregation

Particle collision-coalescence, -riming, -aggregation can be considered a stochastic process. Following Gillespie (1972), consider a region with volume  $\Delta V$ . If  $\Delta V$  is sufficiently small, we can consider that particles within this region are well-mixed, e.g., by atmospheric turbulence. Then, all particle pairs in the volume can collide and coalesce/rime/aggregate during an infinitesimal time interval  $dt$ . The probability that a particle pair  $j$  and  $k$  inside  $\Delta V$  will collide and coalesce/rime/aggregate



within an infinitesimal time interval  $(t, t + dt)$  is given by

$$P_{jk} = K(\mathbf{a}_j, \mathbf{a}_k; \mathbf{G}) \frac{dt}{\Delta V}, \quad (30)$$

where the function  $K(\mathbf{a}_j, \mathbf{a}_k; \mathbf{G})$  is called the collision-coalescence/riming/aggregation kernel and  $\mathbf{G}$  denotes the state of the moist air in  $\Delta V$ .

- 5 In this study, we consider collision-coalescence, -riming, and -aggregation induced by differential gravitational settling of particles as this mechanism is important in mixed-phase clouds.

#### 4.1.9 Coalescence between two droplets

First, we consider droplet collision-coalescence, which accounts for the formation of rain droplets from cloud droplets (auto-conversion) and the collection of cloud droplets by rain droplets (accretion).

- 10 The collision-coalescence kernel is given by

$$K_{\text{coal}} = E_{\text{coal}}(r_j, r_k) \pi(r_j + r_k)^2 |v_j^\infty - v_k^\infty|, \quad (31)$$

- where  $E_{\text{coal}}(r_j, r_k)$  is the collection efficiency of collision-coalescence, which considers the effect that a smaller droplet is swept aside by flow around a larger droplet or bounce on the larger droplet's surface. Following Seeßelberg et al. (1996) and Bott (1998), we adopt the collection efficiency of Davis (1972) and Jonas (1972) for small droplets and that of Hall (1980) for  
 15 larger droplets.

If coalescence takes place, droplets  $j$  and  $k$  then merge into a single droplet. Thus, we keep  $j$  and remove  $k$  from the system. The attributes of the new droplet  $j$  can be calculated as follows:

$$r'_j = (r_j^3 + r_k^3)^{\frac{1}{3}}, \quad (32)$$

$$m_{\alpha j}^{\text{sol}} = m_{\alpha j}^{\text{sol}} + m_{\alpha k}^{\text{sol}}, \quad \alpha = 1, 2, \dots, N^{\text{sol}} \quad (33)$$

20  $m_{\beta j}^{\text{insol}} = m_{\beta j}^{\text{insol}} + m_{\beta k}^{\text{insol}}, \quad \beta = 1, 2, \dots, N^{\text{insol}} \quad (34)$

$$T_j^{\text{fz}'} = \max(T_j^{\text{fz}}, T_k^{\text{fz}}), \quad (35)$$

where primed values indicate the resultant droplet.

#### 4.1.10 Riming between an ice particle and a droplet

- Riming usually refers to the collection of small supercooled droplets by a larger ice particle, but we also include the collection  
 25 of small ice particles by a larger droplet. The latter case can be regarded as a type of contact freezing. However, ice particles grow preferentially when ice particles and supercooled droplets coexist (Wegener-Bergeron-Findeisen mechanism). Therefore, we can expect that the latter case happens less frequently in mixed-phase clouds.



Hereafter we assume, without loss of generality, that particle  $j$  is an ice particle and particle  $k$  is a droplet. The collision-riming kernel is expressed as

$$K_{\text{rime}} = E_{\text{rime}} A_g |v_j^\infty - v_k^\infty|, \quad (36)$$

where  $E_{\text{rime}}$  is the collision-riming collection efficiency and  $A_g$  is the geometric cross-sectional area of  $j$  and  $k$ .

5  $A_g$  for riming is defined in Fig. 1 of Wang and Ji (2000), but calculating it rigorously for porous spheroid models is impossible. Thus, we approximate  $A_g$  by

$$A_g = \pi(a_j + r_k) \{ \max(a_j, c_j) + r_k \} - (A_j^{\text{ce}} - A_j), \quad (37)$$

i.e., the indentation of the ice particle ( $A_j^{\text{ce}} - A_j$ ) is subtracted from the area of an ellipse with semi-axes  $(a_j + r_k)$  and  $\{ \max(a_j, c_j) + r_k \}$ . Therefore, if  $r_k \ll a_j, c_j$ , then  $A_g \approx A_j$ . At the other extreme, if  $r_k \gg a_j, c_j$ , then  $A_g \approx \pi(a_j + r_k) \{ \max(a_j, c_j) + r_k \}$ .

To evaluate collision-riming collection efficiency  $E_{\text{rime}}$ , we combine formulas proposed by Beard and Grover (1974) and Erfani and Mitchell (2017).

If  $v_j^\infty < v_k^\infty$ , we consider droplet  $k$  to be the collector and adopt the formula of Beard and Grover (1974):

$$E_{\text{rime}} = E_{\text{BG74}}(p^{i/w}, N_{\text{Re}k}^w, N_{\text{St}}^{i/w}), \quad (38)$$

15 where  $p^{i/w} := r_j^i / r_k$ ,  $r_j^i := (a_j^2 c_j)^{1/3}$ ,  $N_{\text{Re}k}^w = \rho v_k^\infty 2r_k / \mu$  is the Reynolds number of droplet  $k$ ,  $N_{\text{St}}^{i/w} = (p^{i/w})^2 \rho_j^i N_{\text{Re}k}^w C_{\text{SC}} / (9\rho)$  is the Stokes impaction parameter when droplet  $k$  is collecting an ice particle, and  $C_{\text{SC}}$  is the Cunningham slip correction factor.

If  $v_j^\infty \geq v_k^\infty$ , we consider ice particle  $j$  to be the collector. For spherical ice particle  $\phi_j \approx 1$ , we again use the formula of Beard and Grover (1974), but replace the Stokes impaction parameter  $N_{\text{St}}^{i/w}$  with the mixed Froude number  $N_{\text{mFr}}$  following Hall (1980), Rasmussen and Heymsfield (1985), and Heymsfield and Pflaum (1985). For columnar and planar ice particles,  
 20 we use formulas  $E_{\text{EM17}}^{\text{clm}}$  and  $E_{\text{EM17}}^{\text{pln}}$  from Erfani and Mitchell (2017), which were obtained by fitting the numerical results of Wang and Ji (2000). For the intermediate case, we calculate an average weighted by the aspect ratio  $\phi_j$ . For  $\phi_j \leq 1$  (planar),

$$E_{\text{rime}} = \phi_j E_{\text{BG74}}(p^{w/i}, N_{\text{Re}j}^i, N_{\text{mFr}}) + (1 - \phi_j) E_{\text{EM17}}^{\text{pln}}(N_{\text{Re}j}^i, N_{\text{mFr}}). \quad (39)$$

For  $\phi_j > 1$  (columnar),

$$E_{\text{rime}} = \frac{1}{\phi_j} E_{\text{BG74}}(p^{w/i}, N_{\text{Re}j}^i, N_{\text{mFr}}) + \left( 1 - \frac{1}{\phi_j} \right) E_{\text{EM17}}^{\text{clm}}(N_{\text{Re}j}^i, N_{\text{mFr}}). \quad (40)$$

25 Here,  $p^{w/i} := 1/p^{i/w} = r_k / r_j^i$ ,  $N_{\text{mFr}} = (v_j^\infty - v_k^\infty) v_k^\infty / (gD_j/2)$ , and  $N_{\text{Re}j}^i = \rho v_j^\infty 2a_j / \mu$  is the Reynolds number based on the width of column  $2a_j$ . Note also that there is a typo in Eq. (19) of Erfani and Mitchell (2017), i.e., the two case conditions are opposite.



If riming takes place, the ice particle  $j$  and droplet  $k$  merge and instantaneously freeze into a single ice particle. Thus, we keep  $j$  and remove  $k$  from the system.

If  $\max(a_j, c_j) < r_k$ , we assume that the resultant ice particle is spherical with the true ice density:

$$\rho_j^{i'} = \rho_{\text{true}}^i, \quad (41)$$

$$5 \quad a_j' = c_j' = \left( \frac{m_j + m_k}{(4\pi/3)\rho_{\text{true}}^i} \right)^{\frac{1}{3}}, \quad (42)$$

$$m_j^{\text{rime}'} = m_j^{\text{rime}} + m_k, \quad (43)$$

$$n_j^{\text{mono}'} = n_j^{\text{mono}}, \quad (44)$$

$$m_{\alpha j}^{\text{sol}'} = m_{\alpha j}^{\text{sol}} + m_{\alpha k}^{\text{sol}}, \quad \alpha = 1, 2, \dots, N^{\text{sol}}, \quad (45)$$

$$m_{\beta j}^{\text{insol}'} = m_{\beta j}^{\text{insol}} + m_{\beta k}^{\text{insol}}, \quad \beta = 1, 2, \dots, N^{\text{insol}}, \quad (46)$$

$$10 \quad T_j^{\text{fz}'} = \max(T_j^{\text{fz}}, T_k^{\text{fz}}), \quad (47)$$

where primed values indicate the resultant ice particle.

If  $\max(a_j, c_j) \geq r_k$ , we preserve the ice particle's maximum dimension, i.e.,  $D_j' = D_j$ , until the ice particle becomes quasi-spherical. This accounts for the gradual growth of an unrimed ice crystal to a graupel particle with a quasi-spherical shape. This “filling-in” simplification was introduced by Heymsfield (1982), and is used in various models (e.g., Chen and Lamb, 1994b; Morrison and Grabowski, 2008, 2010; Jensen and Harrington, 2015; Morrison and Milbrandt, 2015). As graupels have an aspect ratio of approximately 0.8 (Heymsfield, 1978), we preserve the minor dimension if  $0.8 < \phi_j \leq 1/0.8 = 1.25$ , which mimics graupel's tumbling. When an accreted droplet freezes, air will be trapped inside. Let rime density  $\rho_{\text{rime}}$  be the frozen droplet's apparent density. Then, for  $\phi_j \leq 0.8$  (planar) and  $1.0 < \phi_j \leq 1.25$  (columnar but quasi-spherical),

$$\rho_j^{i'} = \frac{m_j + m_k}{V_j + m_k/\rho_{\text{rime}}}, \quad (48)$$

$$20 \quad a_j' = a_j, \quad (49)$$

$$c_j' = \frac{V_j + m_k/\rho_{\text{rime}}}{(4\pi/3)a_j^2}. \quad (50)$$

Other attributes are updated by Eqs. (43)–(47). For  $\phi_j > 1.25$  (columnar) and  $0.8 < \phi_j \leq 1.0$  (planar but quasi-spherical),

$$\rho_j^{i'} = \frac{m_j + m_k}{V_j + m_k/\rho_{\text{rime}}}, \quad (51)$$

$$a_j' = \left\{ \frac{V_j + m_k/\rho_{\text{rime}}}{(4\pi/3)c_j} \right\}^{\frac{1}{2}}, \quad (52)$$

$$25 \quad c_j' = c_j. \quad (53)$$

Other attributes are updated by Eqs. (43)–(47). Following Chen and Lamb (1994b), we use the formula of Heymsfield and Pflaum (1985) here to calculate rime density  $\rho_{\text{rime}}$ :

$$\rho_{\text{rime}} = \max\{\min\{\rho_{\text{rime}}^{\text{HP85}}(Y), 0.91 \text{ g cm}^{-3}\}, 0.1 \text{ g cm}^{-3}\}, \quad (54)$$



where  $Y := (-r_k v_{\text{imp}} / T_j^{\text{sfc}}) / (\mu\text{m ms}^{-1} / ^\circ\text{C})$ ,  $v_{\text{imp}}$  is impact velocity,  $T_j^{\text{sfc}}$  is the surface temperature of ice particle  $j$ ,

$$\rho_{\text{rime}}^{\text{HP85}}(Y) = \begin{cases} (\text{g cm}^{-3}) \exp(B_2 + B_3 Y + B_4 Y^2 + B_5 Y^3), & \text{for } T_s > -5^\circ\text{C} \wedge Y > 1.6; \\ AY^{B_1}, & \text{otherwise,} \end{cases} \quad (55)$$

$A = 0.30 \text{ g cm}^{-3}$ ,  $B_1 = 0.44$ ,  $B_2 = -0.03115$ ,  $B_3 = -1.7030$ ,  $B_4 = 0.9116$ , and  $B_5 = -0.1224$ .

Impact velocity can be calculated using the formula of Rasmussen and Heymsfield (1985):  $v_{\text{imp}} = |v_j^\infty - v_k^\infty| \max\{f_{\text{RH85}}(N_{\text{Re}j}^i, N_{\text{St}}^{w/i}), 0\}$ , where  $N_{\text{St}}^{w/i} = (p^{w/i})^2 \rho^w N_{\text{Re}j}^i / (9\rho)$  is the Stokes impaction parameter when an ice particle collects a droplet. Because the formula of Rasmussen and Heymsfield (1985),  $f_{\text{RH85}}$ , becomes slightly negative around  $0.1 < N_{\text{St}}^{w/i} < 1.0$ , we impose a limiter to ensure it is positive. Surface temperature  $T_j^{\text{sfc}}$  can be evaluated as

$$T_j^{\text{sfc}} = T_j + \frac{L_s D_v}{k} \Delta\rho_j, \quad (57)$$

where  $\Delta\rho_j$  is given in Eq. (20). This equation is derived under an assumption of quasi-steady vapor and thermal diffusion.

When riming occurs, the frozen droplet releases latent heat of fusion to the moist air as described in Eqs. (73), (78) and (79).

As we will discuss in Sec. 9.1.1, the rime density formula of Heymsfield and Pflaum (1985) must be revised slightly. We propose to replace the  $Y$  in Eq. (55) (not in Eq. (56)) with  $Y^\downarrow = \min(Y, 3.5)$  (Eq. (95)), because the rime density derived from Eq. (55) becomes too small for larger values of  $Y$ , which affects the shape of hailstones near the freezing level.

Another issue discussed in Sec. 9.1.2 is related to the filling-in model. Assuming that the diameter of the frozen droplet is preserved if the diameter is larger than the ice particle's maximum dimension, we propose replacing Eq. (49) by Eq. (96) and Eq. (53) by Eq. (97).

We validate these two corrections in Sec. 9.1.5. More discussions to refine our collision-riming model will be presented in Sec. 9.2.6.

#### 4.1.11 Aggregation between two ice particles

Finally, we consider the collision-aggregation of ice particles. Following Connolly et al. (2012), we use the projected area of particles to evaluate the geometric cross-sectional area. The collision-aggregation kernel is then given by

$$K_{\text{agg}} = E_{\text{agg}} \left( A_j^{\frac{1}{2}} + A_k^{\frac{1}{2}} \right)^2 |v_j^\infty - v_k^\infty|, \quad (58)$$

where  $E_{\text{agg}}$  is the collision-aggregation collection efficiency. Following Morrison and Grabowski (2010), we assume that the efficiency is given by a constant,  $E_{\text{agg}} = 0.1$ , in this study. Field et al. (2006) confirmed that  $E_{\text{agg}} = 0.09$  produces a good agreement with aircraft observations.

If aggregation takes place, ice particles  $j$  and  $k$  merge into a single ice particle. Thus, we keep  $j$  and remove  $k$  from the system. However, no reliable model exists for calculating the next porous spheroid. Chen and Lamb (1994b) proposed a model, but it tends to create snow aggregates with impossibly low apparent density (lighter than vapor). In this study, we propose another intuitive model incorporating the compaction of fluffy snowflakes to cope with the problem.



Snow aggregates have complicated fractal structures. However, if we circumscribe them using a spheroid, the growth by aggregation is in three dimensions, rather than one (columnar) or two (planar). Therefore, as in the case of riming, we assume that only the minor dimension grows by aggregation.

If the volume weighted average density  $\bar{\rho}_{jk}^i = (m_j + m_k)/(V_j + V_k)$  is closer to the true density of ice  $\rho_{\text{true}}^i$ , the two particles  
 5 aggregate without changing their shapes. Hence, when we approximate the resultant aggregate with a spheroid, there are more empty spaces inside, thus reducing apparent density. Let us denote the minimum possible apparent density as  $\rho_{jk}^{i,\text{min}}$ , which can be evaluated using Eq. (60), which we will derive shortly.

In contrast, if  $\bar{\rho}_{jk}^i$  is small, compaction of the fluffy snowflakes occurs, and the empty space of the larger ice particle may be filled with the smaller ice particle or the particles may deform due to the collision-aggregation impact. Because of this  
 10 compaction mechanism, we assume there is a limiting value of the apparent density, and let it be  $\rho_{\text{crt}}^i = 10 \text{ kg m}^{-3}$ . This choice of value is roughly consistent with observations by Magono and Nakamura (1965). If  $\bar{\rho}_{jk}^i$  is closer to  $\rho_{\text{crt}}^i$ , we consider that the apparent density of the resultant aggregate is closer to the maximum possible density  $\rho_{jk}^{i,\text{max}}$ . Let us assume  $\rho_{jk}^{i,\text{max}} = \bar{\rho}_{jk}^i$ .

In the following, we derive equations describing how to update the attributes.

Without loss of generality, assume that  $D_j \geq D_k$ . For  $\phi_j \leq 1$  (planar),

$$15 \quad a'_j = a_j, \quad (59)$$

because we assumed the maximum dimension is preserved. The longest possible minor axis length is  $c_j + \min(a_k, c_k)$ , hence the largest possible volume becomes  $V_{\text{max}} = (4\pi/3)a_j^2\{c_j + \min(a_k, c_k)\}$ . The minimum possible apparent density  $\rho_{jk}^{i,\text{min}}$  then becomes

$$\rho_{jk}^{i,\text{min}} = \frac{m_j + m_k}{V_{\text{max}}}. \quad (60)$$

20 The resultant particle's apparent density is given by a weighted average of  $\rho_{jk}^{i,\text{max}} = \bar{\rho}_{jk}^i$  and  $\rho_{jk}^{i,\text{min}}$ :

$$\rho_j^{i'} = \frac{(\rho_{\text{true}}^i - \bar{\rho}_{jk}^i)\rho_{jk}^{i,\text{max}} + (\bar{\rho}_{jk}^i - \rho_{\text{crt}}^i)\rho_{jk}^{i,\text{min}}}{\rho_{\text{true}}^i - \rho_{\text{crt}}^i}, \quad (61)$$

where primed values indicate the resultant ice particle. All other attributes are updated as follows:

$$c'_j = \frac{m_j + m_k}{\rho_j^{i'}(4\pi/3)a_j'^2}, \quad (62)$$

$$m_j^{\text{rime}'} = m_j^{\text{rime}} + m_k^{\text{rime}}, \quad (63)$$

$$25 \quad n_j^{\text{mono}'} = n_j^{\text{mono}} + n_k^{\text{mono}}, \quad (64)$$

$$m_{\alpha j}^{\text{sol}'} = m_{\alpha j}^{\text{sol}} + m_{\alpha k}^{\text{sol}}, \quad \alpha = 1, 2, \dots, N^{\text{sol}}, \quad (65)$$

$$m_{\beta j}^{\text{insol}'} = m_{\beta j}^{\text{insol}} + m_{\beta k}^{\text{insol}}, \quad \beta = 1, 2, \dots, N^{\text{insol}}, \quad (66)$$

$$T_j^{\text{fz}'} = \max(T_j^{\text{fz}}, T_k^{\text{fz}}). \quad (67)$$

For  $\phi_j \leq 1$  (planar), the polar axis length is preserved

$$30 \quad c'_j = c_j. \quad (68)$$



If approximating the largest possible particle using an ellipsoid, the largest possible volume becomes  $V_{\max} = (4\pi/3)c_j\{a_j + \min(a_k, c_k)\} \max(a_j, a_k, c_k)$ . Then, the resultant ice particle's apparent density  $\rho_j^i$  can be calculated using Eqs. (60) and (61). Then, the minor axis is updated by

$$a'_j = \left\{ \frac{m_j + m_k}{\rho_j^i (4\pi/3)c'_j} \right\}^{\frac{1}{2}}, \quad (69)$$

5 and other attributes are updated by Eqs. (63)-(67).

Note that our aggregation outcome model does not produce particles lighter than  $\rho_{\text{crit}}^i = 10 \text{ kg m}^{-3}$ .

#### 4.1.12 Limitations of our cloud microphysics model

Eqs. (2)–(69) provide time evolution equations for mixed-phase cloud microphysics. Our model is based on a detailed kinetic description, and all aerosol, cloud, and precipitation particles in the system are followed. The respective activation and deactivation of cloud droplets from and to CCNs, and their growth by diffusion and collision are also explicitly predicted. Additionally, formation of ice particles by condensation/immersion and homogeneous freezing, and gradual morphology changes in ice particles during their growth by diffusion and collision are also predicted explicitly without relying on artificial ice categories or predefined mass-dimension relationships. However, because our basic understanding of mixed-phase cloud microphysics is still not sufficient, the introduced models have room for improvement. Further, several processes important for mixed-phase clouds are ignored for simplicity. For example, collisional breakup of ice particles and rime-splintering are not considered, though they are thought to be responsible for secondary ice production (e.g., Field et al., 2017). In Sec. 9.2, we will discuss more on the limitations and possible future refinements of our model.

#### 4.2 Fluid dynamics of moist air

Moist air fluid dynamics can be described by the compressible Navier-Stokes equation for moist air:

$$20 \quad \frac{\partial \rho}{\partial t} + \nabla \cdot (\rho \mathbf{U}) = \left. \frac{\partial \rho}{\partial t} \right|_{\text{cm}}, \quad (70)$$

$$\frac{\partial \rho q_v}{\partial t} + \nabla \cdot (\rho q_v \mathbf{U}) = \left. \frac{\partial \rho q_v}{\partial t} \right|_{\text{cm}} + D_v \nabla^2 (\rho q_v), \quad (71)$$

$$\frac{\partial \rho \mathbf{U}}{\partial t} + \nabla \cdot (\rho \mathbf{U} \otimes \mathbf{U}) = -\nabla P - \rho g \hat{z} + \left. \frac{\partial \rho \mathbf{U}}{\partial t} \right|_{\text{cm}} + \mu \nabla^2 \mathbf{U}, \quad (72)$$

$$\frac{\partial \rho \theta}{\partial t} + \nabla \cdot (\rho \theta \mathbf{U}) = \left. \frac{\partial \rho \theta}{\partial t} \right|_{\text{cm}} + \frac{k}{c_p} \nabla^2 \theta, \quad (73)$$

$$P = \rho R T = P_0 \left( \frac{\rho \theta R}{P_0} \right)^{c_p / (c_p - R)}, \quad (74)$$

25 where the four terms with the form  $\partial \cdot / \partial t|_{\text{cm}}$  represent cloud microphysics coupling terms.

$\partial \rho / \partial t|_{\text{cm}} = \partial \rho q_v / \partial t|_{\text{cm}}$  is the source of vapor:

$$\left. \frac{\partial \rho}{\partial t} \right|_{\text{cm}} = \left. \frac{\partial \rho q_v}{\partial t} \right|_{\text{cm}} = s_v + s_s. \quad (75)$$



Here,  $s_v$  and  $s_s$  are sources of vapor through condensation/evaporation and deposition/sublimation, respectively:

$$s_v(\mathbf{x}, t) = - \sum_{i \in I_r(t)} \delta^3(\mathbf{x} - \mathbf{x}_i(t)) \left. \frac{dm_i}{dt} \right|_{\text{cnd/evp}}, \quad (76)$$

$$s_s(\mathbf{x}, t) = - \sum_{i \in I_r(t)} \delta^3(\mathbf{x} - \mathbf{x}_i(t)) \left. \frac{dm_i}{dt} \right|_{\text{dep/sbl}}, \quad (77)$$

where  $\delta^3(\mathbf{x})$  is the three-dimensional Dirac's delta function, and the time derivatives for condensation/evaporation and deposition/sublimation are given by Eqs. (6) and (10), respectively.

$\partial\rho\theta/\partial t|_{\text{cm}}$  represents heating due to the phase transition of water:

$$\left. \frac{\partial\rho\theta}{\partial t} \right|_{\text{cm}} = - \frac{L_v s_v + L_s s_s + L_f s_f}{c_p \Pi}, \quad (78)$$

where  $L_f$  is the latent heat of fusion and  $s_f$  is the production rate of liquid water through freezing, melting, or riming. Let  $t_n^{\text{fz}}$  be the time of the  $n$ -th freezing event and  $i_n^{\text{fz}}$  be the index of the frozen droplet. Similarly, let  $t_n^{\text{mlt}}$  and  $i_n^{\text{mlt}}$  be the time and melted ice particle of the  $n$ -th melting event, respectively. Let  $t_n^{\text{rime}}$  and  $i_n^{\text{rime}}$  be the time and rimed droplet of the  $n$ -th riming event, respectively. Then,  $s_f$  is given by

$$\begin{aligned} s_f(\mathbf{x}, t) = & - \sum_{\text{freezing event } n} \delta^3(\mathbf{x} - \mathbf{x}_{i_n^{\text{fz}}}(t)) \delta(t - t_n^{\text{fz}}) m_{i_n^{\text{fz}}}(t) \\ & + \sum_{\text{melting event } n} \delta^3(\mathbf{x} - \mathbf{x}_{i_n^{\text{mlt}}}(t)) \delta(t - t_n^{\text{mlt}}) m_{i_n^{\text{mlt}}}(t) \\ & - \sum_{\text{riming event } n} \delta^3(\mathbf{x} - \mathbf{x}_{i_n^{\text{rime}}}(t)) \delta(t - t_n^{\text{rime}}) m_{i_n^{\text{rime}}}(t). \end{aligned} \quad (79)$$

$\partial\rho\mathbf{U}/\partial t|_{\text{cm}}$  is the drag force from the particles. From Eq. (2), we can derive  $\mathbf{F}_i^{\text{drg}} = m_i g \hat{\mathbf{z}} + d(m_i \mathbf{v}_i)/dt$ . The terminal velocity assumption does not mean that the second term vanishes as  $m_i$  and  $\mathbf{v}_i$  are still time dependent. However, even if a droplet accelerated from  $0 \text{ m s}^{-1}$  to  $10 \text{ m s}^{-1}$  in 100 s through rapid precipitation development, the contribution of the second term is much smaller than that of the first term:  $10 \text{ m s}^{-1}/100 \text{ s} \ll g$ . Thus, we finally obtain

$$\begin{aligned} \left. \frac{\partial\rho\mathbf{U}}{\partial t} \right|_{\text{cm}} = & - \sum_{i \in I_r(t)} \delta^3(\mathbf{x} - \mathbf{x}_i(t)) \mathbf{F}_i^{\text{drg}} \\ \approx & - \left[ \sum_{i \in I_r(t)} \delta^3(\mathbf{x} - \mathbf{x}_i(t)) m_i(t) \right] g \hat{\mathbf{z}}. \end{aligned} \quad (80)$$

### 4.3 Summary of the section

Now, we have the complete set of the system's time evolution equations: Eqs. (2)–(69) for cloud microphysics (i.e., aerosol, cloud, and precipitation particles) and Eqs. (70)–(80) for cloud dynamics (i.e., moist air). With suitable initial and boundary conditions, our mathematical model can predict mixed-phase cloud behavior. In the next section, we explain how the SCALE-SDM numerical model solves those time evolution equations.



## 5 Numerical schemes and implementation

We develop a numerical model known as SCALE-SDM to solve the mathematical model of mixed-phase clouds presented in the preceding sections.

SCALE is a library of weather and climate models of Earth and other planets (Nishizawa et al., 2015; Sato et al., 2015, <http://r-ccs-climate.riken.jp/scale/>). We implemented SDM into SCALE version 0.2.5, thus constructing a mixed-phase cloud model called SCALE-SDM 0.2.5-2.2.0.

In our model, we use SDM to solve cloud microphysics as defined by Eqs. (2)–(69). SDM is a particle-based scheme using an efficient Monte Carlo algorithm for collision-coalescence, -riming, and -aggregation, which enables accurate simulation of aerosol, cloud, and precipitation particles with lower computational demand (Shima et al., 2009).

Moist air fluid dynamics are solved using SCALE’s dynamical core. The compressible Navier-Stokes equation for moist air (70)–(80) is solved fully explicitly using a finite volume method with an Arakawa-C staggered grid. In this study, we resolve only large eddies and do not use a sub-grid scale (SGS) turbulence model. To stabilize the calculation, we add an artificial fourth order hyperdiffusion term. Numerical schemes and implementation are described in further detail.

### 5.1 Spatial discretization of moist air

We consider the density of moist air  $\rho$ , density of water vapor  $\rho q_v$ , momentum of moist air  $\rho \mathbf{U}$ , and mass-weighted potential temperature  $\rho \theta$  as prognostic variables for moist air. We employ the Arakawa-C staggered grid for discretization:  $\rho$ ,  $\rho q_v$ , and  $\rho \theta$  are defined at the center of each grid cell, and the three components of  $\rho \mathbf{U}$  are defined on the faces of each grid cell. To simplify notation we use  $G_{lmn}$  to denote the status of moist air at each grid point. Let  $\Delta x$ ,  $\Delta y$ , and  $\Delta z$  represent grid sizes.

### 5.2 Super-particles and real particles

There are many particles in the atmosphere, thus it is practically impossible to follow all of them in a numerical model. Therefore, we reduce unnecessary degrees of freedom by approximating the population of real particles  $\{\{\mathbf{x}_i(t), \mathbf{a}_i(t)\}, i = 1, 2, \dots, N_r^{\text{WP}}\}$  using a population of super-particles:  $\{\{\xi_i(t), \mathbf{x}_i(t), \mathbf{a}_i(t)\}, i = 1, 2, \dots, N_s^{\text{WP}}\}$  (see, e.g., Fig. 4 of Grabowski et al., 2019). A super-particle is characterized by multiplicity  $\xi_i$ , position  $\mathbf{x}_i$ , and attributes  $\mathbf{a}_i$ . We consider that the  $i$ -th super-particle represents  $\xi_i$  real particles  $\{\mathbf{x}_i, \mathbf{a}_i\}$ . Note that multiplicity  $\xi_i$  is an integer and is time dependent.  $N_s^{\text{WP}}$  is the total number of super-particles accumulated over the whole period.

The relationship between super-particles and real particles can be expressed more precisely as follows. Let  $n(\mathbf{a}, \mathbf{x}, t)$  be the particle distribution function, i.e., the mean number density of particles with attributes  $\mathbf{a}$  at position  $\mathbf{x}$  and time  $t$ . The following relation then holds:

$$n(\mathbf{a}, \mathbf{x}, t) = \left\langle \sum_{i \in I_r(t)} \delta^d(\mathbf{a} - \mathbf{a}_i(t)) \delta^3(\mathbf{x} - \mathbf{x}_i(t)) \right\rangle, \quad (81)$$



where  $\langle \dots \rangle$  denotes mean and  $\delta^d(\mathbf{a})$  is the  $d$ -dimensional Dirac's delta function. Super-particles reproduce the behavior of particles in expectation:

$$\begin{aligned} n(\mathbf{a}, \mathbf{x}, t) &= \left\langle \sum_{i \in I_s(t)} \xi_i(t) \delta^d(\mathbf{a} - \mathbf{a}_i(t)) \delta^3(\mathbf{x} - \mathbf{x}_i(t)) \right\rangle \\ &= N_s(t) \sum_{\xi=1}^{\infty} \xi p(\xi, \mathbf{a}, \mathbf{x}, t), \end{aligned} \quad (82)$$

where  $p(\xi, \mathbf{a}, \mathbf{x}, t)$  is the probability density that a super-particle has multiplicity  $\xi$ , attributes  $\mathbf{a}$ , and position  $\mathbf{x}$  at time  $t$ ;  $I_s(t)$  is the set of super-particle indices existing in the domain at time  $t$ ; and  $N_s(t) := \#I_s(t)$  is the number of super-particles existing at time  $t$ .

### 5.3 Initialization of super-particles

There is an arbitrariness in how to initialize super-particles. In this study, we use the uniform sampling method.

Basically, any probability density function  $p(\xi, \mathbf{a}, \mathbf{x}, t = 0)$  that satisfies Eq. (82) can be used to initialize super-particles; however, Unterstrasser et al. (2017) showed that SDM's performance is sensitive to probability density function.

Let us consider a specific type of procedure in which we assign  $\mathbf{a}$  and  $\mathbf{x}$  based on probability density function  $p(\mathbf{a}, \mathbf{x})$ , and determine the super-particle's multiplicity  $\xi$  using a deterministic function of  $\mathbf{a}$  and  $\mathbf{x}$ , i.e.,  $\xi = \xi(\mathbf{a}, \mathbf{x})$ . Then, Eq. (82) at  $t = 0$  reduces to

$$n(\mathbf{a}, \mathbf{x}, 0) = N_s(0) \xi(\mathbf{a}, \mathbf{x}) p(\mathbf{a}, \mathbf{x}). \quad (83)$$

If we set  $\xi(\mathbf{a}, \mathbf{x})$  as a constant, the probability density function must be proportional to the initial distribution function of real particles:  $p(\mathbf{a}, \mathbf{x}) \propto n(\mathbf{a}, \mathbf{x}, 0)$ . This so-called constant multiplicity method was adopted in Shima et al. (2009). However, Unterstrasser et al. (2017) found that the numerical convergence of this method with respect to super-particle number is slow. (Note that constant multiplicity method is referred to as  $\nu_{\text{const}}$ -init in Unterstrasser et al. (2017).)

Instead, we can set  $p(\mathbf{a}, \mathbf{x})$  as a constant (i.e., uniform sampling). Multiplicity then becomes proportional to the initial distribution function of real particles:

$$\xi(\mathbf{a}, \mathbf{x}) = \frac{n(\mathbf{a}, \mathbf{x}, 0)}{N_s(0)p}, \quad p(\mathbf{a}, \mathbf{x}) = p = \text{const}. \quad (84)$$

Using the uniform sampling method, we can more frequently sample rare but important particles in the tail of the distribution, thus improving the numerical convergence. This uniform sampling method has been used in various studies (e.g., Arabas and Shima, 2013; Shima et al., 2014; Sato et al., 2017, 2018).

Unterstrasser et al. (2017) proposed several other procedures using a grid, known as SingleSIP-init, multiSIP-init, and  $\nu_{\text{random}}$ -init, to more uniformly distribute super-particles along the particle size axis. They confirmed that their methods had much better performance than the constant multiplicity method, but did not try the uniform sampling method. Dziekan and Pawlowska (2017) also proposed a similar procedure. However, both works focused on collision-coalescence and their initialization procedures are tested only in a zero-dimensional simulation (box model) with one particle attribute (size). It is



questionable whether their procedures would work efficiently for three-dimensional (3D) simulations with several particle attributes. It is known that the “discrepancy” of axis-aligned grid decreases very slowly in higher dimensions (e.g., Niederreiter, 1978). Therefore, an axis-aligned grid is generally not suitable for sampling high dimensional space. A uniform sampling method should be more efficient for such a purpose, and using quasi-random numbers would further improve performance. Meanwhile, as indicated in Grabowski et al. (2018), we should also note that the unbalanced weight of super-particles could cause larger statistical fluctuations when super-particles are advected from one grid cell of moist air to another.

All in all, further study is required to determine an optimal method for initializing super-particles. In this study we use the uniform sampling method given by Eq. (84). More details of our procedure will be specified in Sec. 6.1.7. As shown in Fig. 10, our model’s numerical convergence with respect to super-particle number is good for at least the 2D cumulonimbus simulation that we will conduct to evaluate our model.

#### 5.4 Operator splitting of the time integration

We evaluate each process separately using the first order operator splitting scheme. Let  $\Delta t$  be the common time step. Here we explain how  $\{\{\xi_i, \mathbf{x}_i, \mathbf{a}_i\}\}$  and  $\mathbf{G}_{lmn}$  are updated from time  $t$  to  $t + \Delta t$ .

Let  $\Delta t_{adv}$ ,  $\Delta t_{fz/mlt}$ ,  $\Delta t_{cnd/evp}$ ,  $\Delta t_{dep/sbl}$ , and  $\Delta t_{coal}$  be the time steps for the advection and sedimentation of particles, freezing and melting, condensation and evaporation, deposition and sublimation, and collision-coalescence, -riming, and -aggregation, respectively.

Let  $\Delta t_{dyn}$  be the time step for moist air fluid dynamics, which must fulfill the Courant-Friedrichs-Lewy (CFL) condition of acoustic waves.

These process time steps are all divisors of common time step  $\Delta t$ .

We first calculate fluid dynamics without coupling terms from particles to moist air (75)–(80), and update moist air from  $\mathbf{G}_{lmn}(t)$  to  $\mathbf{G}'_{lmn}(t)$ . Then, we update super-particles  $\{\{\xi_i, \mathbf{x}_i, \mathbf{a}_i\}\}$  from  $t$  to  $t + \Delta t$ . We select one elementary cloud microphysics process, integrate it forward by one time step, and then move on to the next process. Here, processes lagging behind in time are calculated preferentially. Simultaneously, we evaluate feedback from particles to moist air through the coupling terms (75)–(80), and update the moist air from  $\mathbf{G}'_{lmn}(t)$  to  $\mathbf{G}_{lmn}(t + \Delta t)$ . Figure. 1 shows an example of calculation order.

#### 5.5 Time integration of cloud microphysics

We use SDM to solve cloud microphysics. Details of the numerical schemes used to calculate cloud microphysics are provided in this section. The state of ambient air  $\mathbf{G}_i := \mathbf{G}(\mathbf{x}_i)$  around a super-particle  $i$  is often needed. For scalar variables, we use the value at the center point of the grid cell in which the super-particle is located, whereas we interpolate wind velocities from face grids, as detailed in the next section.



	$t \xrightarrow{\hspace{1.5cm}} t+\Delta t$					
fluid dynamics	1	2	3	4	5	6
advection	7					
freezing/melting	8					
condensation/evaporation	9	12	13	15	17	19
deposition/sublimation	10		14		18	
collision-coalescence/ riming/aggregation	11			16		

**Figure 1.** An example of calculation order when updating system state from  $t$  to  $t + \Delta t$ . We first calculate the fluid dynamics and then calculate cloud microphysics. Each process is integrated one time step forward at a time. Processes lagging behind in time are calculated preferentially.

### 5.5.1 Advection and sedimentation

For each super-particle, the motion equation (3) is solved using time step  $\Delta t_{adv}$ . We normally select a short enough  $\Delta t_{adv}$  to satisfy the CFL condition for wind velocity. For consistency of wind velocity field divergence, we use a predictor-collector scheme with the “simple linear interpolation” of wind velocities from the face grid following Grabowski et al. (2018). The momentum  $\rho U$  is defined on the face grid and density  $\rho$  is defined on the center grid. Therefore, we average the  $\rho_{lmn}$  on both sides of the face grid to calculate wind velocity  $U_{lmn}$  on the face grid. We then interpolate  $U_{lmn}$  to the super-particle position using the simple linear scheme of Grabowski et al. (2018).

The reaction force acting on moist air is calculated using Eq. (80). Feedback from each super-particle is imposed only on the  $(\rho W)_{lmn}$  nearest the super-particle.

### 10 5.5.2 Freezing and melting

Every  $\Delta t_{fz/mlt}$  interval, for each super-particle, freezing and melting is examined following the model detailed in Secs. 4.1.4 and 4.1.5. The exchange of latent heat of fusion is calculated using Eqs. (73), (78), and (79). Feedback from each super-particle is imposed only on the grid cell where the super-particle is located.

### 5.5.3 Condensation and evaporation

15 For each super-droplet, we solve the condensation and evaporation equation (7) with a time step of  $\Delta t_{cnd/evp}$ . The activation/deactivation time scale is very short. To eliminate stiffness, we convert the equation to the time evolution equation of  $r^2$  following Shima et al. (2009) and adopt the backward Euler scheme.

The exchange of vapor and latent heat with moist air is calculated using Eqs. (70), (71), (73), (75), (76), and (78). Feedback from each super-droplet is imposed only on the grid cell where the super-droplet is located.



The growth of droplets is calculated implicitly, but the evolution of supersaturation through feedback is calculated explicitly. Therefore, the length of  $\Delta t_{\text{cnd/evp}}$  is restricted mostly by supersaturation's phase relaxation time due to condensation and evaporation, which is the timescale in which a supersaturation fluctuation decays through condensation or evaporation.

#### 5.5.4 Deposition and sublimation

5 For each ice super-particle, we solve the deposition and sublimation time evolution equations detailed in Sec. 4.1.7 using the time step  $\Delta t_{\text{dep/sbl}}$ . Contrary to the condensation and evaporation equation (7), the time evolution equation of mass (10) is not stiff as the curvature term is ignored and the solute effect does not exist. Let us convert the equation to the time evolution equation of  $m^{2/3}$ . Then, if the ice particle is spherical and we ignore the ventilation effect, the r.h.s. of the resultant equation does not depend on  $m$ . Therefore, we adopt the forward Euler scheme to solve the time evolution equation of  $m^{2/3}$ .

10 The exchange of vapor and latent heat with moist air is calculated using Eqs. (70), (71), (73), (75), (77), and (78). Feedback from each ice super-particle is imposed only on the grid cell where the ice super-particle is located.

$\Delta t_{\text{dep/sbl}}$  is restricted by the timescale of individual ice particle growth through deposition and sublimation and the phase relaxation time of supersaturation due to deposition and sublimation.

#### 5.5.5 Collision-coalescence, -riming, and -aggregation

15 The stochastic process of collision-coalescence, -riming, and -aggregation detailed in Secs. 4.1.8–4.1.11 is solved using the Monte Carlo scheme of Shima et al. (2009). The time step  $\Delta t_{\text{coal}}$  is restricted by the mean free time of a particle, i.e., the average waiting time for a particle between two successive collision-coalescence/riming/aggregation events.

The exchange of latent heat of fusion due to riming is calculated using Eqs. (73), (78), and (79). Feedback from each super-particle is imposed only on the grid cell where the super-particle is located.

#### 20 5.6 Time integration of moist air fluid dynamics

Moist air fluid dynamics is governed by the compressible Navier-Stokes equation (70)–(80). In this study, as explained in the previous section, the four coupling terms from cloud microphysics with the form  $\partial \cdot / \partial t|_{\text{cm}}$  are evaluated when calculating cloud microphysics.

We solve the compressible Navier-Stokes equation without coupling terms fully explicitly using a finite volume method with an Arakawa-C staggered grid. For spatial discretization, the fourth order central difference scheme is used for advection terms and the second order central difference scheme is used for other spatial derivatives. To preserve monotonicity, the flux-corrected transport scheme of Zalesak (1979) is applied to water vapor advection. For time integration, the three-step Runge-Kutta scheme of Wicker and Skamarock (2002) is used. An artificial, fourth order hyperdiffusion term is added to stabilize the calculation. For this study, the non-dimensional diffusion coefficient defined in Eq. (A132) of Nishizawa et al. (2015) is set as  $\gamma = 10^{-3}$ .

30 For more details of the numerical schemes used for fluid dynamics, see Nishizawa et al. (2015) and Sato et al. (2015).

The time step  $\Delta t_{\text{dyn}}$  must satisfy the CFL condition of acoustic waves.



## 6 Design of numerical experiments for model evaluation: 2D simulation of an isolated cumulonimbus

The basic equations and numerical implementation of SCALE-SDM were described in the preceding sections. To evaluate our numerical model's performance, we conduct a 2D simulation of an isolated cumulonimbus following the setup of Khain et al. (2004). In this section, we first describe the atmospheric conditions and numerical parameters used for the control case, denoted by CTRL. To evaluate fluctuation, we conduct a 10-member ensemble of simulations by changing the pseudo-random number sequence. To investigate the simulation's numerical convergence, we will change super-particle number concentration, grid sizes, and time steps of CTRL. Those ensembles are denoted by NSP, DX, and DT, respectively. Our choice of parameters is specified in the subsequent sections. Table 1 summarizes the model setup for all cases.

### 6.1 Control ensemble (CTRL)

In this section, the atmospheric conditions and numerical parameters used for the CTRL ensemble are specified.

#### 6.1.1 Initial moist air conditions

The domain is 2D ( $x$ - $z$ ), 60 km in the horizontal direction and 16 km in the vertical direction.

The initial atmospheric profile is horizontally uniform, and the vertical moist air profile is given by sounding data from Midland, Texas, on 13 August 1999, as shown in Fig. 4 of Khain et al. (2004). The cloud base and freezing level are at about 2.2 km (14 °C) and 4.1 km, respectively. We consider that the wind is initially horizontal and wind velocity increases from 4 ms<sup>-1</sup> near the surface to 7 ms<sup>-1</sup> at 400 hPa, and remains unchanged at higher levels.

#### 6.1.2 Moist air boundary conditions

For the lateral boundaries, we impose periodic boundary conditions. For the upper and lower boundaries, we set the vertical wind velocity  $W$  to zero, i.e., a zero-fixed boundary condition for vertical momentum  $\rho W$  and no flux boundary conditions for other prognostic variables.

#### 6.1.3 Initial conditions of particles

Initially, the particles are distributed uniformly in space at random, and consist of pure ammonium bisulfate aerosol particles and mineral dusts internally mixed with ammonium bisulfate.

The initial number-size distribution of the population of pure ammonium bisulfate particles is given by a bimodal log-normal distribution,

$$\frac{dN^{\text{sulf}}}{d\log r_{\text{dry}}^{\text{sulf}}} = \sum_{a=1}^2 \frac{1}{\sqrt{2\pi}} \frac{c_a^{\text{sulf}}}{\log \sigma_a} \exp \left[ -\frac{(\log r_{\text{dry}}^{\text{sulf}} - \log r_a)^2}{2 \log^2 \sigma_a} \right], \quad (85)$$

where  $r_{\text{dry}}^{\text{sulf}}$  is the dry radius of the ammonium bisulfate component and  $N^{\text{sulf}}$  is the accumulated number of particles smaller than  $r_{\text{dry}}^{\text{sulf}}$  per unit volume of air. The particle number concentrations are  $c_1^{\text{sulf}} = 270 \text{ cm}^{-3}$  and  $c_2^{\text{sulf}} = 45 \text{ cm}^{-3}$ , thus, the total



**Table 1.** Summary of numerical experiments for model evaluation. The domain is two-dimensional ( $x$ - $z$ ), 60 km in the horizontal direction and 16 km in the vertical direction. The initial profile of moist air is given by sounding data from Midland, Texas, on 13 August 1999, as shown in Fig. 4 of Khain et al. (2004). The particles are initially distributed uniformly in space at random and consist of pure ammonium bisulfate aerosol particles and mineral dusts internally mixed with ammonium bisulfate. The numerical parameters used in each case are listed in the table and values changed from the CTRL case are in bold. We conducted a 10-member ensemble of simulations for each case by changing the pseudo random number sequence to evaluate fluctuation.

Case	Super-particle		Time steps						
	number	Grid size							
	concentration	$\Delta x = \Delta y = \Delta z$	$\Delta t$	$\Delta t_{adv}$	$\Delta t_{fz/mlt}$	$\Delta t_{coal}$	$\Delta t_{cnd/evp}$	$\Delta t_{dep/sbl}$	$\Delta t_{dyn}$
	$c^{SP}$	[m]	[s]	[s]	[s]	[s]	[s]	[s]	[s]
	[/cell]								
CTRL	128	62.5	0.4	0.4	0.4	0.2	0.1	0.1	0.05
NSP002	<b>2</b>	62.5	0.4	0.4	0.4	0.2	0.1	0.1	0.05
NSP004	<b>4</b>	62.5	0.4	0.4	0.4	0.2	0.1	0.1	0.05
⋮	⋮	⋮	⋮	⋮	⋮	⋮	⋮	⋮	⋮
NSP128 (CTRL)	128	62.5	0.4	0.4	0.4	0.2	0.1	0.1	0.05
NSP256	<b>256</b>	62.5	0.4	0.4	0.4	0.2	0.1	0.1	0.05
NSP512	<b>512</b>	62.5	0.4	0.4	0.4	0.2	0.1	0.1	0.05
DXx4	128	<b>250.0</b>	<b>1.6</b>	<b>1.6</b>	<b>1.6</b>	0.2	0.1	0.1	<b>0.2</b>
DXx2	128	<b>125.0</b>	<b>0.8</b>	<b>0.8</b>	<b>0.8</b>	0.2	0.1	0.1	<b>0.1</b>
DXx1 (CTRL)	128	62.5	0.4	0.4	0.4	0.2	0.1	0.1	0.05
DX/2	128	<b>31.25</b>	<b>0.2</b>	<b>0.2</b>	<b>0.2</b>	0.2	0.1	0.1	<b>0.025</b>
DTx2	128	62.5	<b>0.8</b>	<b>0.8</b>	<b>0.8</b>	<b>0.4</b>	<b>0.2</b>	<b>0.2</b>	0.05
DTx1 (CTRL)	128	62.5	0.4	0.4	0.4	0.2	0.1	0.1	0.05
DT/2	128	62.5	<b>0.2</b>	<b>0.2</b>	<b>0.2</b>	<b>0.1</b>	<b>0.05</b>	<b>0.05</b>	0.05
DT/4	128	62.5	<b>0.1</b>	<b>0.1</b>	<b>0.1</b>	<b>0.05</b>	<b>0.025</b>	<b>0.025</b>	0.05

particle number concentration is  $c^{\text{sulf}} = c_1^{\text{sulf}} + c_2^{\text{sulf}} = 315 \text{ cm}^{-3}$ . The geometric mean radii are  $r_1 = 0.03 \mu\text{m}$  and  $r_2 = 0.14 \mu\text{m}$ , with geometric standard deviations of  $\sigma_1 = 1.28$  and  $\sigma_2 = 1.75$ , respectively. This distribution is based on *in situ* maritime aerosol data as detailed in Sec. 2.2.3 of VanZanten et al. (2011), but the number concentration is multiplied by three. As discussed in Sec. 2.4, we consider that a droplet containing only soluble substances freezes only through a homogeneous freezing mechanism; therefore, the freezing temperature of these particles is  $T^{\text{fz}} = -38^\circ\text{C}$ . Therefore, pure ammonium bisulfate's initial distribution function can be calculated as

$$n^{\text{sulf}}(\log r_{\text{dry}}^{\text{sulf}}, T^{\text{fz}}) = \frac{dN^{\text{sulf}}}{d \log r_{\text{dry}}^{\text{sulf}}} \delta(T^{\text{fz}} - (-38^\circ\text{C})). \quad (86)$$



The other aerosol population consists of mineral dust internally mixed with ammonium bisulfate. We set the number concentration to  $c^{\text{dust}} = 1 \text{ cm}^{-3}$ , and for simplicity set the mineral dust particle diameter to  $d^{\text{dust}} = 1 \mu\text{m}$  initially. We assume the same size distribution of internally mixed ammonium bisulfate as that of the pure ammonium bisulfate (85). The probability density function of freezing temperature  $p(T^{\text{fz}})$  is given by eq. (1). Here, we use the INAS density formula from Niemand et al. (2012), but based on the discussion in Niedermeier et al. (2015), we do not extrapolate the formula to lower or higher temperatures:

$$n_{\text{S}}(T) = \begin{cases} 0, & \text{for } T > T_{\text{max}}^{\text{fz}}; \\ n_{\text{S}}^{\text{Niemand}}(T), & \text{for } T_{\text{max}}^{\text{fz}} \geq T > T_{\text{min}}^{\text{fz}}; \\ n_{\text{S}}^{\text{Niemand}}(T_{\text{min}}^{\text{fz}}), & \text{for } T_{\text{min}}^{\text{fz}} \geq T; \end{cases} \quad (87)$$

where  $T_{\text{max}}^{\text{fz}} = -12^\circ\text{C}$  and  $T_{\text{min}}^{\text{fz}} = -36^\circ\text{C}$ . Mineral dust surface area is given by  $A^{\text{insol}} = \pi(d^{\text{dust}})^2$ . As discussed in Sec. 2.4, we set  $T^{\text{fz}} = -38^\circ\text{C}$  if the mineral dust is IN inactive and no INAS appears until  $T^{\text{fz}} = -38^\circ\text{C}$ . Altogether, the mineral dust distribution function is given by

$$\begin{aligned} n^{\text{dust}}(d^{\text{dust}}, \log r_{\text{dry}}^{\text{sulf}}, T^{\text{fz}}) \\ = \delta(d^{\text{dust}} - 1 \mu\text{m}) \frac{c^{\text{dust}}}{c^{\text{sulf}}} \frac{dN^{\text{sulf}}}{d \log r_{\text{dry}}^{\text{sulf}}} \\ [p(T^{\text{fz}})H(T^{\text{fz}} + 38^\circ\text{C}) + P_{\text{INia}}\delta(T^{\text{fz}} + 38^\circ\text{C})], \end{aligned} \quad (88)$$

where  $H(T)$  is the Heaviside step function and  $P_{\text{INia}} := P(T^{\text{fz}} \leq -38^\circ\text{C})$  is the probability that a single INAS does not appear until  $T^{\text{fz}} = -38^\circ\text{C}$ . For  $d^{\text{dust}} = 1 \mu\text{m}$ ,  $P_{\text{INia}} \approx 0.056$ .

#### 6.1.4 Boundary conditions for particles

We also impose periodic boundary conditions on particles for the lateral boundaries. If a particle crosses the upper or lower boundary, we remove that particle from the system.

#### 6.1.5 Surface heating

Convective cloud development is triggered by a 20min heating within a 10km wide region centered at  $x = 5 \text{ km}$ , and is expressed as

$$\left. \frac{\partial \rho \theta}{\partial t} \right|_{\text{sfc}} = \rho H \max(W, 0), \quad (89)$$

$$W = \left( -\frac{4}{w^2} \right) \left[ (x - x_0)^2 - \left( \frac{w}{2} \right)^2 \right] \exp \left[ -\frac{z - z_0}{z_0} \right], \quad (90)$$

where  $H = 10 \text{ K/h}$ ,  $x_0 = 5 \text{ km}$ ,  $w = 10 \text{ km}$ , and  $z_0 = 0.5 \text{ km}$ . The heating has a parabolic shape in the horizontal direction and decays exponentially in the vertical direction.



### 6.1.6 Grid size and time steps

We use a uniform grid throughout this study, with a grid size of  $\Delta x = \Delta y = \Delta z = 62.5$  m in the CTRL case. The time steps in the CTRL case are  $\Delta t = 0.4$  s,  $\Delta t_{\text{adv}} = \Delta t_{\text{fz/mlt}} = 0.4$  s,  $\Delta t_{\text{coal}} = 0.2$  s,  $\Delta t_{\text{cnd/evp}} = \Delta t_{\text{dep/sbl}} = 0.1$  s, and  $\Delta t_{\text{dyn}} = 0.05$  s.

### 6.1.7 Initialization of super-particles

- 5 Initially, the super-particles are distributed uniformly throughout the domain at random with a number concentration of  $c^{\text{SP}} = 128/\text{cell}$ . We consider half of them to be pure ammonium bisulfate aerosol particles, a few of them to IN inactive mineral dust particles internally mixed with ammonium bisulfate, and the remainder to be IN active mineral dust particles internally mixed with ammonium bisulfate.

The multiplicity, ammonium bisulfate mass, and freezing temperature of each pure ammonium bisulfate super-particle is assigned as follows. For each pure ammonium bisulfate super-particle we draw a random number uniformly in log-space from the interval  $[r_{\text{dry,min}}^{\text{sulf}}, r_{\text{dry,max}}^{\text{sulf}}]$  and calculate the dry radius  $r_{\text{dry},i}^{\text{sulf}}$ . To accurately represent the size distribution given in eq. (85), we set  $r_{\text{dry,min}}^{\text{sulf}} = 10.0$  nm and  $r_{\text{dry,max}}^{\text{sulf}} = 5.0$   $\mu\text{m}$ . From Eqs. (84) and (86), the super-particle's multiplicity is then given by

$$\xi_i = \frac{dN^{\text{sulf}}}{d \log r_{\text{dry}}^{\text{sulf}}} (\log r_{\text{dry},i}^{\text{sulf}}) \frac{\log(r_{\text{dry,max}}^{\text{sulf}}/r_{\text{dry,min}}^{\text{sulf}})}{c^{\text{SP}}/2}. \quad (91)$$

The ammonium bisulfate mass is calculated from the dry radius  $r_{\text{dry},i}^{\text{sulf}}$  as  $m_{1i}^{\text{sulf}} = (4\pi/3)\rho_{(\text{NH})_4\text{HSO}_4}(r_{\text{dry},i}^{\text{sulf}})^3$ , where  $\rho_{(\text{NH})_4\text{HSO}_4} = 1.78$  g  $\text{cm}^{-3}$ . Soluble aerosol particle freezing temperature is  $T_i^{\text{fz}} = -38^\circ\text{C}$ .

For IN inactive mineral dust super-particles, we use  $P_{\text{INia}}^{\text{SP}} = 0.05$ . The mineral dusts initially have the same size  $d^{\text{dust}} = 1$   $\mu\text{m}$ . The dry radius  $r_{\text{dry},i}^{\text{sulf}}$  is calculated using the same procedure as the pure ammonium bisulfate aerosol particles, i.e., for each super-particle we draw a random number uniformly in log-space from the interval  $[r_{\text{dry,min}}^{\text{sulf}}, r_{\text{dry,max}}^{\text{sulf}}]$ . IN inactive mineral dust freezing temperature is  $T_i^{\text{fz}} = -38^\circ\text{C}$ . From Eqs. (84) and (88), an IN inactive mineral dust super-particle's multiplicity is then given by

$$\xi_i = \frac{c^{\text{dust}}}{c^{\text{sulf}}} \frac{dN^{\text{sulf}}}{d \log r_{\text{dry}}^{\text{sulf}}} (\log r_{\text{dry},i}^{\text{sulf}}) \frac{\log(r_{\text{dry,max}}^{\text{sulf}}/r_{\text{dry,min}}^{\text{sulf}})}{c^{\text{SP}}/2} \frac{P_{\text{INia}}}{P_{\text{INia}}^{\text{SP}}}. \quad (92)$$

Finally, we consider IN active mineral dusts internally mixed with ammonium bisulfate. The remaining super-particles, i.e.,  $(1 - P_{\text{INia}}^{\text{SP}})/2$ , are used for this population. Mineral dust initial diameter is  $d^{\text{dust}} = 1$   $\mu\text{m}$  and the dry radius  $r_{\text{dry},i}^{\text{sulf}}$  is determined as in the other populations. We draw another random number uniformly from the interval  $[T_{\text{min}}^{\text{fz}}, T_{\text{max}}^{\text{fz}}]$  and determine the freezing temperature  $T_i^{\text{fz}}$ . From Eqs. (84) and (88), an IN active mineral dust super-particle's multiplicity is then given by

$$\xi_i = \frac{c^{\text{dust}}}{c^{\text{sulf}}} \frac{dN^{\text{sulf}}}{d \log r_{\text{dry}}^{\text{sulf}}} (\log r_{\text{dry},i}^{\text{sulf}}) p(T_i^{\text{fz}}) \frac{\log(r_{\text{dry,max}}^{\text{sulf}}/r_{\text{dry,min}}^{\text{sulf}})(T_{\text{max}}^{\text{fz}} - T_{\text{min}}^{\text{fz}})}{(c^{\text{SP}}/2)(1 - P_{\text{INia}}^{\text{SP}})}. \quad (93)$$



Note that multiplicity  $\xi_i$  is an integer variable. We round the r.h.s. of Eqs. (91)–(93) to the nearest integer, and if the r.h.s. is  $< 1$  we draw a random number to decide whether to choose  $\xi_i = 1$  or  $\xi_i = 0$  to avoid sampling error. If  $\xi_i = 0$ , the super-particle will be removed from the system.

Assuming that all the particles are deliquescent, we consider that the initial droplet radius  $r_i$  is equal to the equilibrium radius of condensation/evaporation growth equation (7). Because the vapor profile is initially subsaturated relative to liquid water and all particles contain soluble substances, the growth equation (7) has a unique, stable equilibrium solution.

### 6.1.8 Pseudo-random numbers

To evaluate the fluctuation, we conduct a 10-member ensemble of simulations by changing the pseudo-random number sequence.

Now the atmospheric conditions and numerical parameters used for the CTRL ensemble have all been specified.

## 6.2 Other ensembles for investigating numerical convergence

We also try various other test cases by changing the CTRL ensemble's numerical parameters, and assess the sensitivity of results to numerical parameters. Our parameter selections are specified in the following sections and a summary is provided in Table 1.

### 6.2.1 NSP ensembles for super-particle number convergence

To investigate numerical convergence with respect to initial super-particle number concentration  $c^{\text{SP}}$ , we vary  $c^{\text{SP}}$  as follows: 2, 4, ..., 512/cell. Grid size and time steps are not changed. These cases are respectively denoted by NSP002, NSP008, ..., NSP512. We conduct a 10-member ensemble of simulations, changing the pseudo-random number sequence for each case. Note that NSP128 and CTRL are the same.

### 6.2.2 DX ensembles for grid convergence

To investigate numerical convergence with respect to grid size we run ensembles using different grid sizes.

The grid size of the DXx4 ensemble is four times that of CTRL:  $\Delta x = \Delta y = \Delta z = 250$  m,  $\Delta t_{\text{dyn}} = 0.2$  s, and  $\Delta t = \Delta t_{\text{adv}} = \Delta t_{\text{fz/mlt}} = 1.6$  s, but other time steps, i.e.,  $\{\Delta t_{\text{coal}}, \Delta t_{\text{cnd/evp}}, \Delta t_{\text{dep/sbl}}\}$ , are not changed.

The DXx2 ensemble's grid size is twice that of CTRL:  $\Delta x = \Delta y = \Delta z = 125$  m,  $\Delta t_{\text{dyn}} = 0.1$  s, and  $\Delta t = \Delta t_{\text{adv}} = \Delta t_{\text{fz/mlt}} = 0.8$  s.

Note that DXx1 and CTRL are the same.

The DX/2 ensemble has a grid size that is half that of CTRL:  $\Delta x = \Delta y = \Delta z = 31.25$  m.  $\Delta t_{\text{dyn}} = 0.025$  s, and  $\Delta t = \Delta t_{\text{adv}} = \Delta t_{\text{fz/mlt}} = 0.2$  s.

Each DX ensemble consists of 10 simulations using different pseudo-random number sequences.



### 6.2.3 DT ensembles for time step convergence

To investigate numerical convergence with respect to cloud microphysics time steps, we change cloud microphysics time steps for CTRL without changing the time step for fluid dynamics.

The time steps for the DTx2 ensemble's cloud microphysics are twice that of CTRL:  $\Delta t = \Delta t_{\text{adv}} = \Delta t_{\text{fz/mlt}} = 0.8 \text{ s}$ ,  
5  $\Delta t_{\text{coal}} = 0.4 \text{ s}$ , and  $\Delta t_{\text{cnd/evp}} = \Delta t_{\text{dep/sbl}} = 0.2 \text{ s}$ .  $\Delta t_{\text{dyn}}$  is not changed.

Note that DTx1 and CTRL are the same.

The time steps of the DT/2 ensemble are half that of CTRL:  $\Delta t = \Delta t_{\text{adv}} = \Delta t_{\text{fz/mlt}} = 0.2 \text{ s}$ ,  $\Delta t_{\text{coal}} = 0.1 \text{ s}$ , and  $\Delta t_{\text{cnd/evp}} =$   
 $\Delta t_{\text{dep/sbl}} = 0.05 \text{ s}$ .

The time steps of the DT/4 ensemble are one quarter that of CTRL:  $\Delta t = \Delta t_{\text{adv}} = \Delta t_{\text{fz/mlt}} = 0.1 \text{ s}$ ,  $\Delta t_{\text{coal}} = 0.05 \text{ s}$ , and  
10  $\Delta t_{\text{cnd/evp}} = \Delta t_{\text{dep/sbl}} = 0.025 \text{ s}$ .

Each DT ensemble consists of 10 simulations using different pseudo-random number sequences.

## 7 Typical behavior of CTRL ensemble

We conducted 10 CTRL case simulations using different pseudo-random number sequences. As shown in the next section, there  
are a fluctuations due to atmospheric turbulence. From the 10 CTRL ensemble members we selected the one that produced  
15 accumulated precipitation amounts closest to the mean value as the representative, hereafter referred to as the typical realization  
of CTRL. In this section, we analyze these results in detail.

### 7.1 Hydrometeor categorization

We do not categorize hydrometeors during the simulation, which is one of the salient features of our model as artificial parti-  
tioning of hydrometeors can cause various artifacts. In contrast, when analyzing results, dividing hydrometeors into categorizes  
20 is useful for precisely understanding the results.

In this study we assume that hydrometeors completely freeze or melt instantaneously (see Secs. 4.1.4 and 4.1.5). Further, we  
assume that all particles contain soluble components and are hygroscopic. If not frozen, we assume the particles are deliques-  
cent even when humidity is low (see Sec. 4.1.6). We also introduced a limiter (13) to prevent complete sublimation. Hence, all  
particles can be categorized as either droplets or ice particles with no ambiguity.

25 If a particle is a droplet and its radius  $r$  is  $< 40 \mu\text{m}$ , we consider it a cloud droplet. Otherwise, the particle is considered a  
rain droplet.

If a particle is an ice particle with a rimed mass fraction satisfying  $m^{\text{rime}}/m > 0.3$ , we consider it a graupel particle. This  
criterion is based on riming categories in Fig. 5 of Mosimann et al. (1994), in which 0.3 corresponds to a densely rimed  
ice crystal. If the maximum dimension of a graupel particle is  $> 5 \text{ mm}$ , we consider it a hailstone; however, for the sake of  
30 simplicity we consider hailstones to be a subset of graupel and they will not be distinguished in the figures. If the ice particle



is not a graupel particle, but rather is composed of  $> 10$  monomers, i.e.,  $n^{\text{mono}} > 10$ , we consider the ice particle a snow aggregate. Otherwise, we categorize the ice particle as a cloud ice particle.

## 7.2 Spatial structure of the cloud, water path, and precipitation amount

We first analyze the cloud's overall properties, and then, in the next section, we analyze the properties of individual ice particles.

5 Figure 2 shows how the cloud's spatial structure in the typical realization of CTRL evolved over time. The mixing ratio of cloud water, rainwater, cloud ice, graupel, and snow aggregates are plotted in fading white, yellow, blue, red, and green, respectively. See also Movie 1 in the Supplement.

Figure 3 shows how the amounts of hydrometeors in the atmosphere evolved over time. The domain-averaged cloud water, rainwater, cloud ice water, graupel water, and snow aggregate water paths are plotted in gray, yellow, blue, red, and green, 10 respectively. Figure 4 shows the time evolution of domain-averaged accumulated precipitation amounts. Solid lines represent the typical realization of CTRL in both figures. Dark shades indicate the mean  $\pm$  standard deviation, which were calculated using the 10 CTRL ensemble members. The unbiased estimator was used to calculate the standard deviation. Pale shades indicate the maximum and minimum values of the 10 ensemble members.

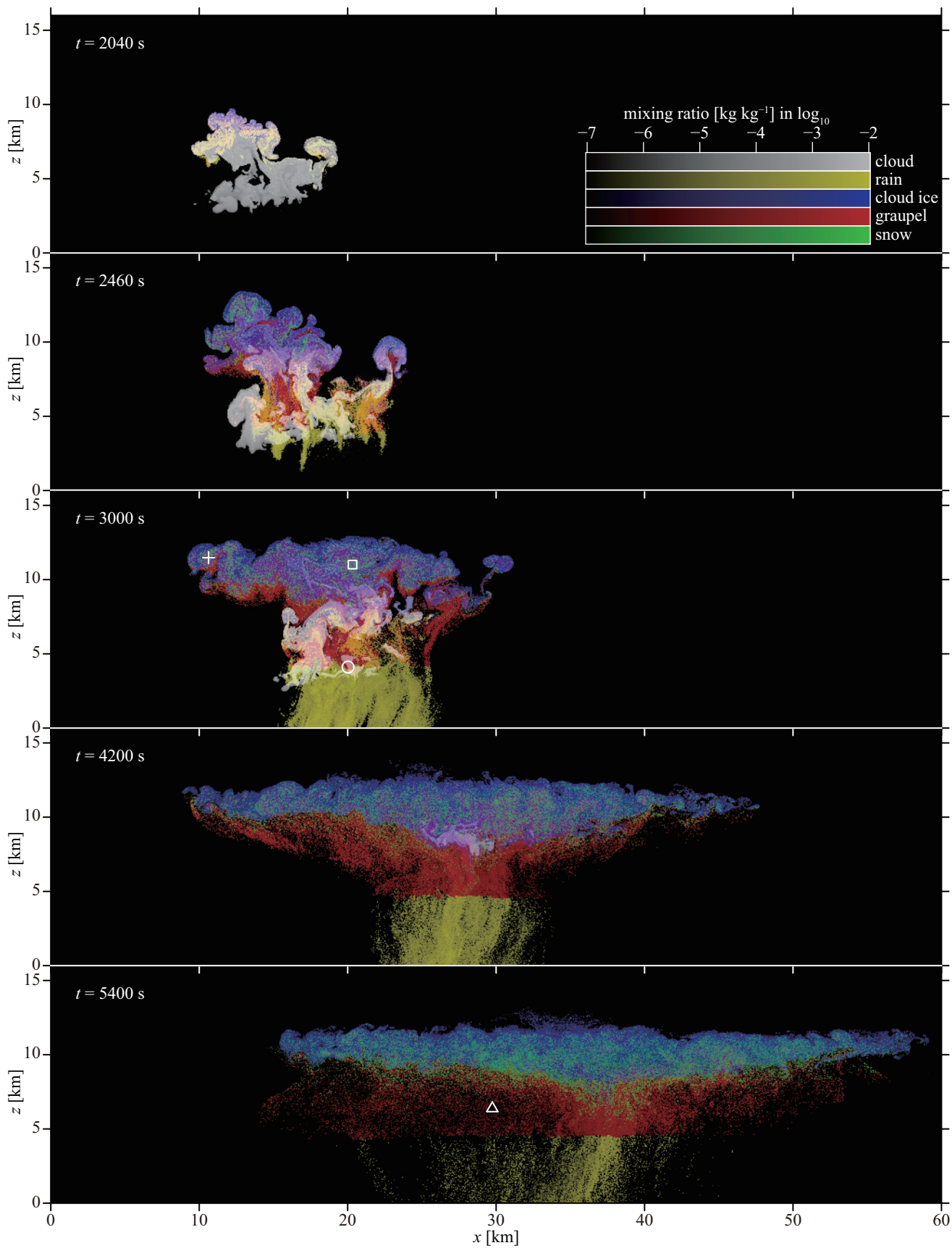
The cloud started to form at approximately  $t = 1200$ s, and at approximately  $t = 1900$ s, rain droplets started to be created 15 through warm rain microphysics processes. Soon after that, supercooled droplets near the cloud top started to freeze and the amount of supercooled cloud droplets quickly decreased due to the Wegener-Bergeron-Findeisen process and collision-riming, but did not disappear until around  $t = 5000$ s. The ice particles quickly evolved into graupel particles through collision-riming, then fell toward the surface. When crossing the freezing level at approximately  $z = 4.1$  km, graupel instantaneously melted into rain droplets, based on our model. The peak of the rainwater path at  $t = 2800$ s was created by graupel melting. The 20 first rain droplet reached the surface at about  $t = 2800$ s, and heavy precipitation was sustained for 1200s, followed by weak precipitation. At the end of the simulation ( $t = 5400$ s), the domain-averaged accumulated precipitation amount was 1.2 mm. An anvil cloud was created between  $z = 10$  km and  $z = 12$  km. The anvil cloud was mostly composed of cloud ice particles, with a small amount of snow aggregates that increased slowly over time through collision-aggregation of cloud ice particles.

## 7.3 Ice particle morphology and fall speeds

25 Now we analyze properties of individual ice particles in the typical realization of CTRL.

Figure 5 shows the mass-dimension relationship of ice particles at  $t = 2040$ s (towering stage), 3000s (mature stage), and 5400s (dissipating stage). The 2D mass densities of cloud ice particles, graupel particles, and snow aggregates are plotted in fading blue, red, and green, respectively. The horizontal axis represents the maximum ice particle dimension  $D$ . The vertical axis represents the normalized ice particle mass  $m^*$ , which is defined by the ratio of ice particle mass  $m$  to the mass of a 30 spherical ice particle with the same maximum dimension  $D$  and the true density of ice  $\rho_{\text{true}}^{\text{i}}$ :

$$m^* := \frac{\rho^{\text{i}} a^2 c}{\rho_{\text{true}}^{\text{i}} (D/2)^3}, \quad D = 2 \max(a, c). \quad (94)$$



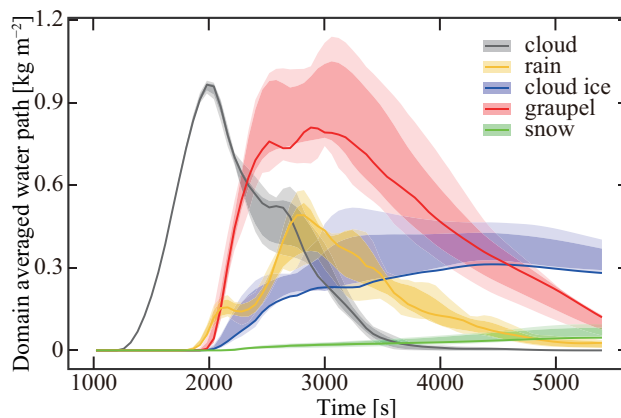


**Figure 3.** Time evolution of the domain-averaged water path in the CTRL ensemble. The cloud water, rainwater, cloud ice water, graupel water, and snow aggregate water paths are plotted in gray, yellow, blue, red, and green, respectively. The solid line represents the typical realization of CTRL. Dark shades indicate the mean  $\pm$  standard deviation and pale shades indicate the maximum and minimum values of the 10 ensemble members.

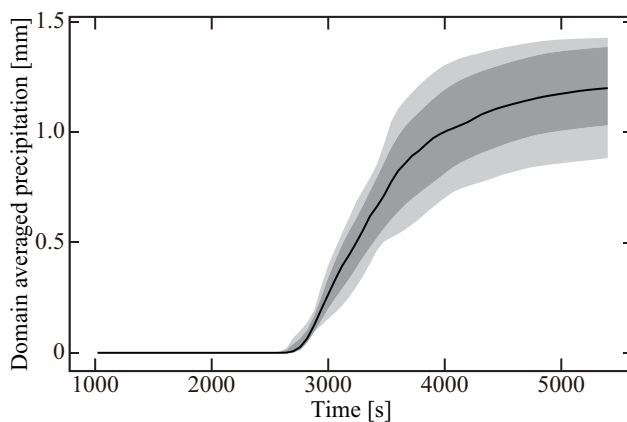


**Figure 4.** Time evolution of domain-averaged accumulated precipitation amounts in the CTRL ensemble. The solid line represents the typical realization of CTRL. The dark shade indicates the mean  $\pm$  standard deviation and the pale shade indicates the maximum and minimum values of the 10 ensemble members.



Note that  $m^* \leq 1$  always holds true. To calculate 2D mass densities, we divided the 2D  $D$ - $m^*$  space into  $100 \times 100$  bins, accumulated the masses of ice particles in each bin, and divided total masses by the area of each bin measured in  $\log_{10}(D)$  and  $\log_{10}(m^*)$ . The colored segments in Fig. 5 represent mass-dimension relationship formulas from various studies, and M96, HK87, K89, M90, and LH74 indicate Mitchell (1996), Heymsfield and Kajikawa (1987), Kajikawa (1989), Mitchell et al. (1990), and Locatelli and Hobbs (1974), respectively. Note that “crystals with sector like branches (M96)” and “stellar crystals with broad arms (M96)” consists of two segments, respectively, but both are not continuous. See also Movie 2 in the Supplement.

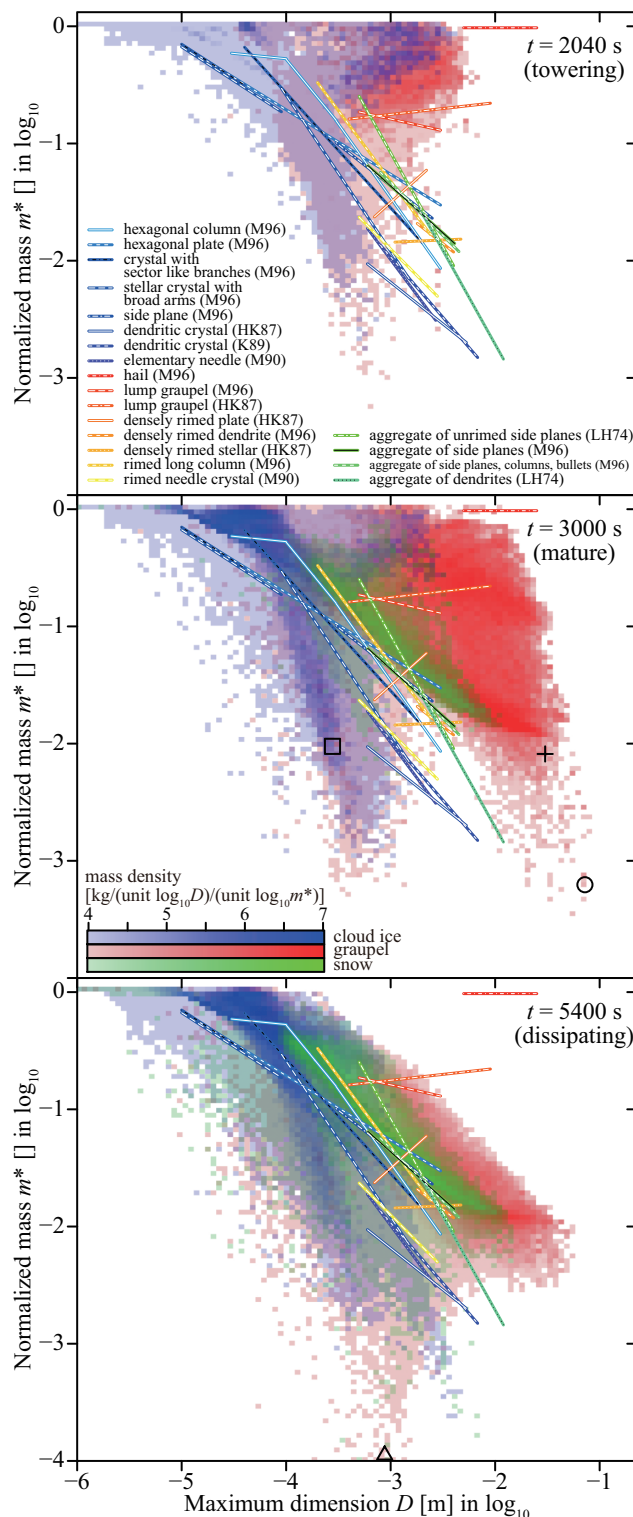
Figure 6 shows the relationship between ice particle aspect ratios and dimensions at  $t = 2040$ s,  $3000$ s, and  $5400$ s. The horizontal axis represents the maximum ice particle dimension  $D$  and the vertical axis represents the ice particle aspect ratio  $\phi$ . The 2D mass densities of cloud ice particles, graupel particles, and snow aggregates are plotted in the same way as Fig. 5, except for differences in the vertical axis. Note that if  $\phi > 1$  ( $\phi < 1$ ), ice particles are columnar (planar). See also Movie 3 in the Supplement.

Figure 7 shows the relationship between ice particle apparent densities and dimensions at  $t = 2040$ s,  $3000$ s, and  $5400$ s. The horizontal axis represents the maximum ice particle dimension  $D$  and the vertical axis represents ice particle apparent density  $\rho^i$ . The 2D mass densities of cloud ice particles, graupel particles, and snow aggregates are plotted in the same way as Fig. 5, except for differences in the vertical axis. See also Movie 4 in the Supplement.

Figure 8 shows the relationship between ice particle velocities and dimensions at  $t = 2040$ s,  $3000$ s, and  $5400$ s. The horizontal axis represents the maximum ice particle dimension  $D$  and the vertical axis represents ice particle terminal velocity  $v^\infty$ . The 2D mass densities of cloud ice particles, graupel particles, and snow aggregates are plotted in the same way as Fig. 5, except for differences in the vertical axis. The colored segments in Fig. 8 represent velocity-dimension relationship formulas from various studies, and SC85, W08, H72, KH83, A72, and H02 indicate Starr and Cox (1985), Westbrook et al. (2008), Heymsfield (1972), Knight and Heymsfield (1983), Auer (1972), and Heymsfield et al. (2002), respectively; “Stokes’ law for ice spheres” is based on the Stokes’ terminal velocity for spherical ice particles with the true ice density. Dynamic viscosity at a temperature of  $-20^\circ\text{C}$  is used, i.e.,  $\mu = 1.630 \times 10^{-5} \text{ kg m}^{-1} \text{ s}^{-1}$ ; The two segments of W08 are based on the analytical formula of Westbrook et al. (2008) for  $< 100 \mu\text{m}$  ice particles. For “hexagonal plates”,  $L/2a = 0.05$  is assumed, with  $L$  being the height of the hexagonal prism and  $a = D/2$  being the hexagon’s maximal radius. Effective radius is calculated using the horizontal orientation model from Roscoe (1949). For “hexagonal columns”,  $L/2a = 20$  is assumed, and the effective radius is calculated using the random orientation model of Hubbard and Douglas (1993). In both cases, dynamic viscosity at a temperature of  $-20^\circ\text{C}$  is used. See also Movie 5 in the Supplement.

At  $t = 2040$ s (towering stage), cloud glaciation had just started, and a small amount of planar and columnar cloud ice particles and graupel particles can be observed. The two horizontal red bands at  $\phi = 0.8$  and  $\phi = 1/0.8$  in Fig. 6 were created because of our assumption that riming growth eventually makes ice particles quasi-spherical.

At  $t = 3000$ s (mature stage), many hailstones (graupel particles  $> 5$  mm) can be observed in the cloud’s middle layer. We also have many columnar cloud ice particles and a small amount of snow aggregates in the upper part of the cloud. Those cloud



**Figure 5.** Mass-dimension relationship of ice particles in the typical realization of CTRL at  $t = 2040\text{s}$ ,  $3000\text{s}$ , and  $5400\text{s}$ . The 2D mass densities of cloud ice particles, graupel particles, and snow aggregates are plotted in fading blue, red, and green, respectively. The horizontal and vertical axes represent maximum ice particle dimension  $D$ , and normalized ice particle mass  $m^*$ , respectively. Colored segments represent various mass-dimension relationship formulas. Symbols indicate examples of unrealistic predicted ice particles (Sec. 7.3 and Sec. 9.1).

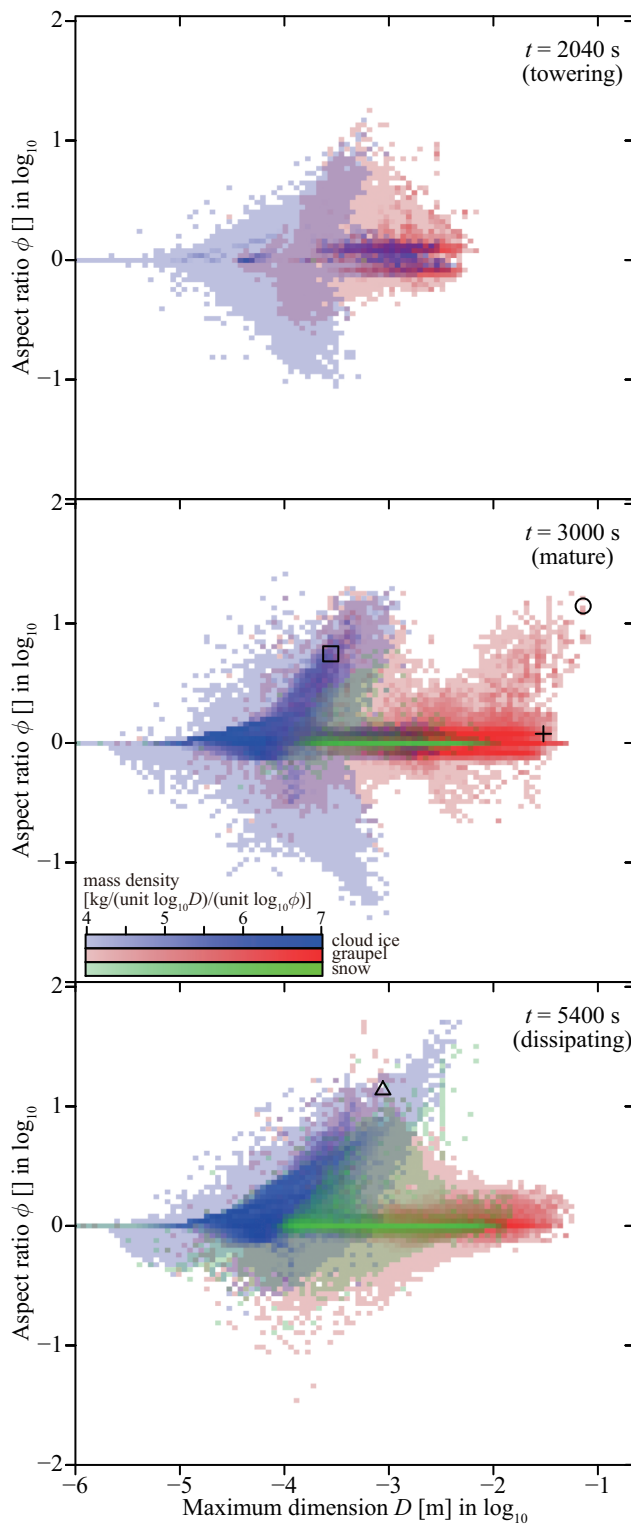


**Figure 6.** Aspect ratio-dimension relationship of ice particles in the typical realization of CTRL at  $t = 2040$  s,  $3000$  s, and  $5400$  s. The vertical axis represents ice particle aspect ratio  $\phi$ . This figure is the same as Fig. 5, except for the vertical axis difference. Symbols indicate examples of unrealistic predicted ice particles (Sec. 7.3 and Sec. 9.1). See also Movie 3 in the Supplement.

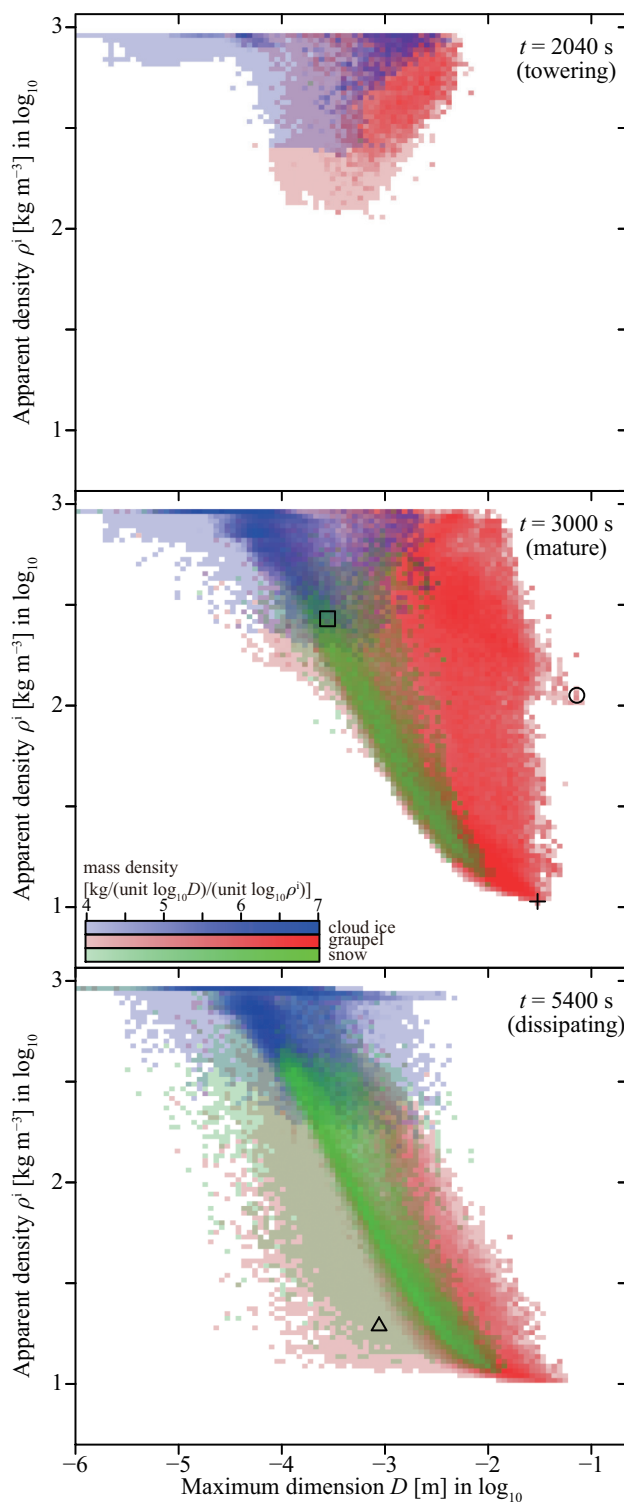


**Figure 7.** Apparent density-dimension relationship of ice particles in the typical realization of CTRL at  $t = 2040$  s,  $3000$  s, and  $5400$  s. The vertical axis represents ice particle apparent density  $\rho^i$ . This figure is the same as Fig. 5, except for the vertical axis difference. Symbols indicate examples of unrealistic predicted ice particles (Sec. 7.3 and Sec. 9.1). See also Movie 4 in the Supplement.

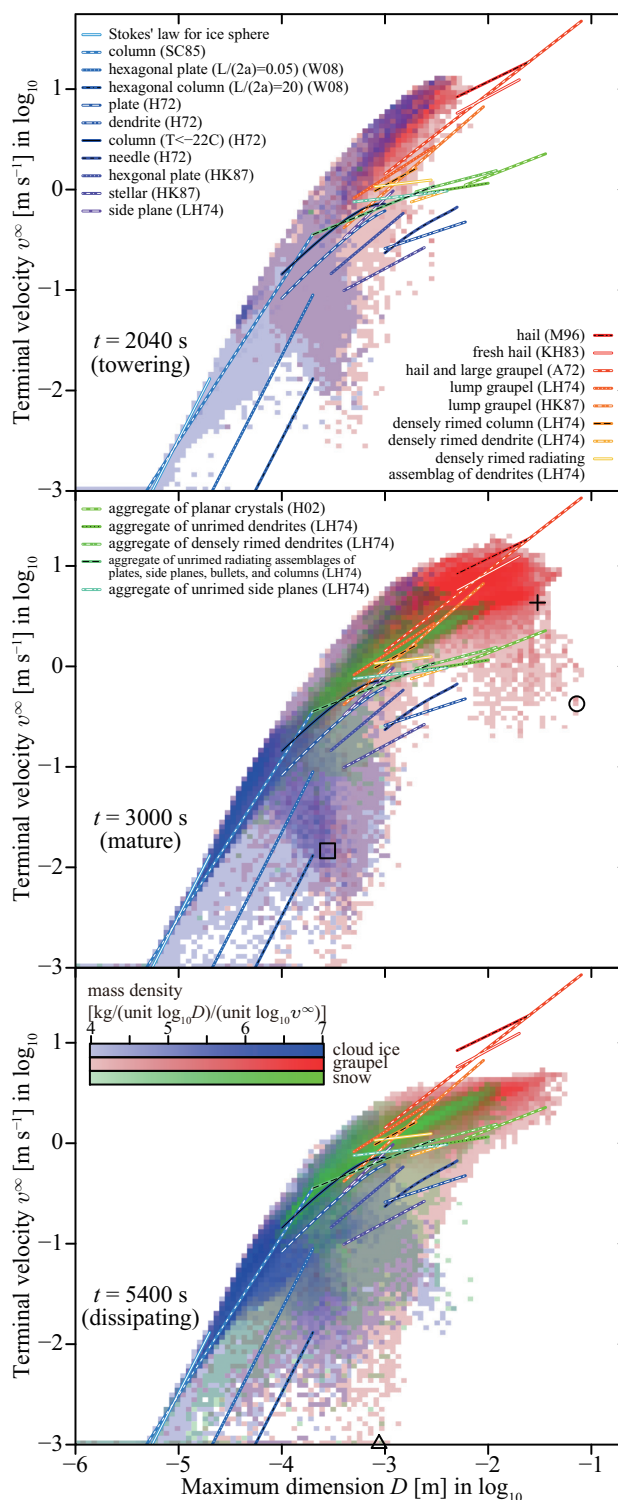


**Figure 8.** Velocity-dimension relationship of ice particles in the typical realization of CTRL at  $t = 2040$  s,  $3000$  s, and  $5400$  s. The vertical axis represents ice particle terminal velocity  $v^\infty$ . This figure is the same as Fig. 5, except for the vertical axis difference. Colored segments represent various velocity-dimension relationship formulas. Symbols indicate examples of unrealistic predicted ice particles (Sec. 7.3 and Sec. 9.1). See also Movie 5 in the Supplement.



ice particles were columnar because our model's inherent growth ratio  $\Gamma(T)$  is  $> 1$  at this height. Many of the snow aggregates were spherical because our model assumed that aspect ratio  $\phi$  approaches to 1 as aggregation occurs.

At  $t = 5400$ s (dissipating stage), most of the graupel particles had fallen away and only a small amount remained. More columnar cloud ice particles and snow aggregates can be observed in the anvil.

5 The mass-dimension relationship shown in Fig. 5 and the velocity-dimension relationship shown in Fig. 8 show a reasonable agreement between our model's predicted results and existing formulas based on laboratory measurements and observations. In both figures, cloud ice particles, graupel particles, and snow aggregates are distributed near the blue, red, and green segments, respectively. However, at the same time, we also see several types of seemingly unrealistic ice particles, representative examples of which are indicated by symbols in Figs. 2, 5–8: The ice particle denoted by the circle at  $t = 3000$ s is a long, slowly  
10 falling hailstone. The square at  $t = 3000$ s is a columnar cloud ice particle that is not consistent with known mass-dimension relationships. The cross at  $t = 3000$ s is a hailstone with a very low apparent density. The triangle at  $t = 5400$ s is a long graupel particle with a very low apparent density. In Sec. 9.1, we will investigate the causes of these odd behaviors in more detail, but those issues can basically be attributed to uncertainties in ice microphysics process formulations.

## 8 Results of the numerical convergence tests

15 Our numerical model uses three types of numerical parameters, super-particle number concentration, grid size, and time steps, which correspond to the resolution of aerosol/cloud/precipitation particle distribution in real space and attribute space, the spatial resolution of moist air, and temporal resolution. The numerical solution from our model approaches the true solution of time evolution equations (2)–(80) as the super-particle number approaches the number of real particles and the grid size and time steps approach zero.

20 To confirm the numerical convergence of the cumulonimbus case, we conducted a series of simulations changing the numerical parameters of CTRL. These ensembles are referred to as NSP, DX, and DT (see Table 1). Our results suggest that the numerical parameters used for the CTRL case can produce accurate numerical result. The detail of this analysis is presented in this section.

### 8.1 NSP ensembles and super-particle number convergence

25 Numerical convergence with respect to the initial super-particle number concentration  $c^{\text{SP}}$  was investigated by varying the  $c^{\text{SP}}$  value of CTRL as follows: 2, 4, ..., 512/cell (see Table 1). These cases are referred to as NSP002, NSP004, ..., and NSP512, respectively. For each case, we conducted a 10-member ensemble of simulations with different pseudo-random number sequences. Note that NSP128 and CTRL are the same.

30 Figure 9 shows accumulated precipitation amount statistics at the end of the simulation ( $t = 5400$ s) versus the initial super-particle number concentration  $c^{\text{SP}}$ . The error bars indicate the mean and standard deviation calculated from the 10 members of each NSP ensemble. The unbiased estimator was used to calculate standard deviations. Crosses denote maximum and minimum values of the 10 ensemble members.

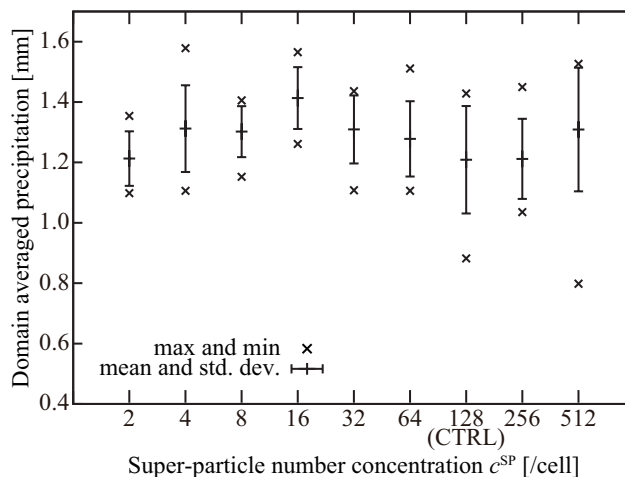


Figure 10 shows statistics of the maximum water path of each hydrometeor type during the simulation (i.e., the maximum of each line in Fig. 3) versus the initial super-particle number concentration  $c^{SP}$ . Error bars indicate the mean and standard deviation from the 10 members of each NSP ensemble. The unbiased estimator was used for calculating standard deviations. Symbols indicate the maximum and minimum values of each hydrometeor type in the 10 ensemble members.

5 Our model has two sources of fluctuation, atmospheric turbulence and SDM randomness. Pseudo-random numbers are used for the Monte Carlo calculation of collision-coalescence, -riming, and -aggregation, and to initialize super-particles. The standard deviation of the fluctuation caused by SDM randomness decreases proportionally to the inverse of the square root of super-particle number. However, Figs. 9 and 10 show that the fluctuation is not sensitive to the initial super-particle number concentration  $c^{SP}$ . This indicates that fluctuations in all simulations are dominated by atmospheric turbulence.

10 Figure 9 shows that the accumulated precipitation amount is less sensitive to super-particle number. However, the maximum water path statistics in Fig. 10 clearly indicate that the initial super-particle number concentration  $c^{SP}$  must be larger than 128/cell. When the number of super-particles was too low, more rain droplets were produced because of an erroneous enhancement of collision-coalescence that suppressed the amount of cloud droplets, cloud ice particles, and graupel particles.

To summarize, NSP ensemble results suggest that numerical convergence with respect to super-particle number is achieved  
 15 at NSP128 (CTRL), i.e.,  $c^{SP} = 128/\text{cell}$ .



**Figure 9.** Statistics of NSP ensemble accumulated precipitation amounts. The vertical axis represents accumulated precipitation at the end of the simulation ( $t = 5400\text{s}$ ), and the horizontal axis represents the initial super-particle number concentration  $c^{SP}$ . Error bars indicate the mean and standard deviation calculated from the 10 members of each NSP ensemble. Crosses denote maximum and minimum values of the 10 ensemble members.

## 8.2 DX ensembles and grid convergence

Numerical convergence with respect to grid size was investigated by varying  $\Delta x = \Delta y = \Delta z$  of CTRL as follows: 31.25, 62.5, 125, and 250 m (see Table 1). These cases are referred to as DX/2, DXx1, DXx2, and DXx4, respectively. We conducted

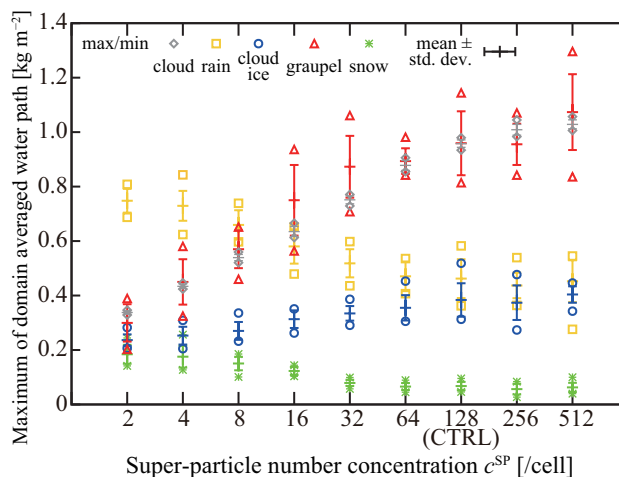


**Figure 10.** Statistics of NSP ensemble maximum water paths for each hydrometeor type. The vertical axis represents the maximum water path of each hydrometeor type during the simulation (i.e., the maximum of each line in Fig. 3), and the horizontal axis represents the initial super-particle number concentration  $c^{SP}$ . Error bars indicate the mean and standard deviation calculated from the 10 members of each NSP ensemble. Symbols denote maximum and minimum values of the 10 ensemble members.

a 10-member ensemble of simulations for each case using different pseudo-random number sequences. Note that DXx1 and CTRL are the same.

Figure 11 shows the accumulated precipitation amount statistics at the end of the simulation versus grid size, plotted in the same way as Fig. 9 except for the difference in the horizontal axis.

5 Figure 12 shows the maximum water path statistics for each hydrometeor type during the simulation versus grid size, plotted in the same way as Fig. 10 except for the difference in the horizontal axis.

The DX/2 ensemble is the highest grid resolution tested in this study, and a snapshot of the cloud from the DX/2 ensemble is shown in Fig. 13. Mixing ratios are plotted in the same way as Fig. 2. See also Movie 6 in the Supplement.

10 Figure 11 shows that accumulated precipitation amount increased from a grid size of 125 m to a grid size of 62.5 m, but no significant difference exists between the 62.5 m and 31.25 m grids. Similar behavior can be observed in the maximum rainwater path in Fig. 12; however, no significant difference exists for other hydrometeor types. Comparing Fig. 13 (31.25 m) and Fig. 2 (62.5 m), the spatial structures of the clouds also look similar.

Therefore, we conclude that numerical convergence with respect to grid size is achieved at DXx1 (CTRL), i.e.,  $\Delta x = \Delta y = \Delta z = 62.5$  m.

### 15 8.3 DT ensembles and time step convergence

Numerical convergence with respect to cloud microphysics time steps was investigated by varying CTRL's cloud microphysics time steps by factors of 1/4, 1/2, 1, and 2 (see Table 1). These cases are referred to as DT/4, DT/2, DTx1, and DTx2, respec-

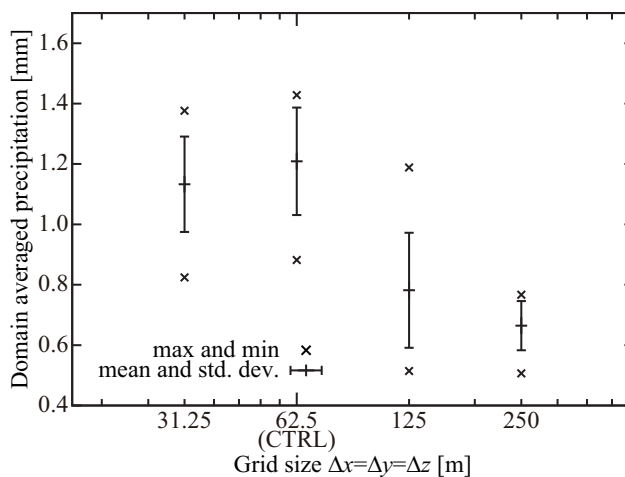


**Figure 11.** Statistics of DX ensemble accumulated precipitation amounts. The horizontal axis represents grid size  $\Delta x = \Delta y = \Delta z$ . This figure has the same form as Fig. 9, except for a difference in the horizontal axis.

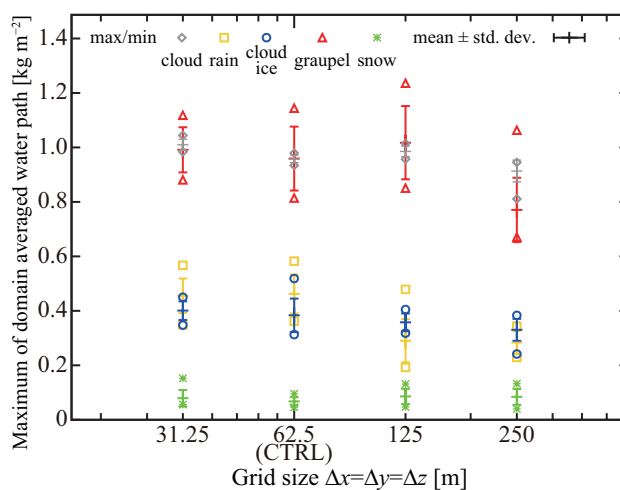


**Figure 12.** Statistics of the DX ensemble maximum water paths for each hydrometeor type. The horizontal axis represents the grid size  $\Delta x = \Delta y = \Delta z$ . This figure has the same form as Fig. 10, except for a difference in the horizontal axis.

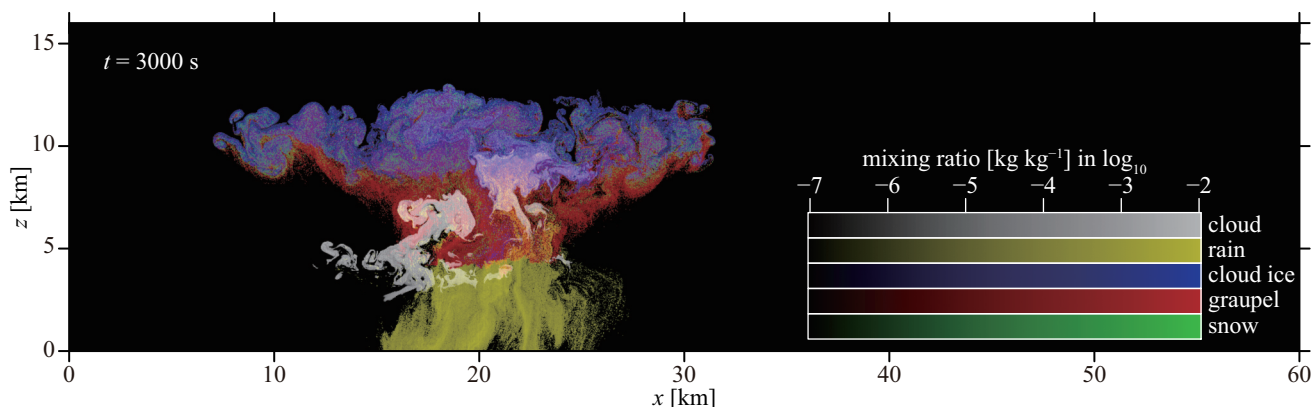


**Figure 13.** Spatial structure of the cloud at  $t = 3000$  s from a DX/2 ensemble member. This figure is formatted the same as Fig. 2, except for the grid resolution. See also Movie 6 in the Supplement.

tively. We conducted a 10-member ensemble of simulations for each case using different pseudo-random number sequences. Note that DTx1 and CTRL are the same.

Figure 14 shows the statistics of accumulated precipitation amounts at the end of the simulation versus the ratio of cloud microphysics time steps to CTRL, plotted in the same manner as Fig. 9 except for the difference in the horizontal axis.

5 Figure 15 shows statistics of the maximum water path of each hydrometeor type during the simulation versus the ratio of cloud microphysics time steps to CTRL, plotted in the same manner as Fig. 10 except for the difference in the horizontal axis.

Both figures show no significant difference among the four ensembles; therefore, we conclude that the numerical convergence with respect to time steps is already attained at DTx1 (CTRL), i.e.,  $(\Delta t, \Delta t_{\text{adv}}, \Delta t_{\text{fz/mlt}}, \Delta t_{\text{coal}}, \Delta t_{\text{cnd/evp}}, \Delta t_{\text{dep/sbl}}) = (0.4\text{s}, 0.4\text{s}, 0.4\text{s}, 0.2\text{s}, 0.1\text{s}, 0.1\text{s})$ . Because DTx2 does not show any difference, time steps twice as large or even larger  
10 could suffice.

Further discussion of numerical convergence characteristics is provided in Sec. 9.3

## 9 Discussions

Results of the typical realization of CTRL presented in Sec. 7 show that our model well captures characteristics of a real cumulonimbus. At the same time, as indicated by the symbols in Figs. 2 and 5–8, our model produces several types of seemingly  
15 unrealistic ice particles. Further, not all of the elementary cloud microphysics processes important for mixed-phase clouds are incorporated in our model yet. In this section, we explore possible improvements and further sophistication of the model and then conduct a general discussion of our model's numerical convergence characteristics and computational cost based on results presented in Sec. 8.

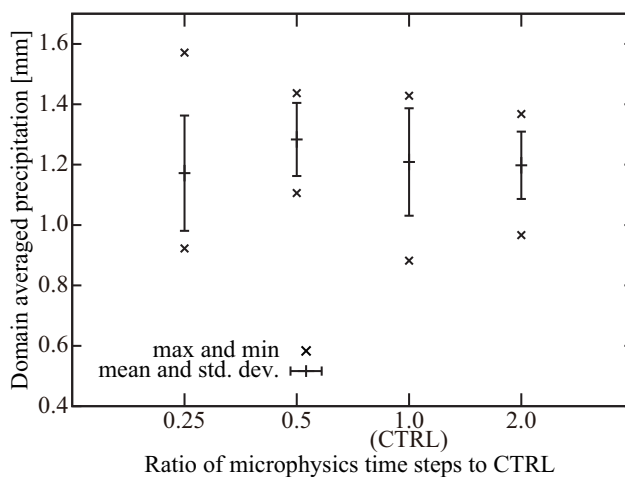


**Figure 14.** Statistics of DT ensemble accumulated precipitation amounts. The horizontal axis represents the ratio of cloud microphysics time steps to CTRL. This figure has the same form as Fig. 9, except for the difference in the horizontal axis.

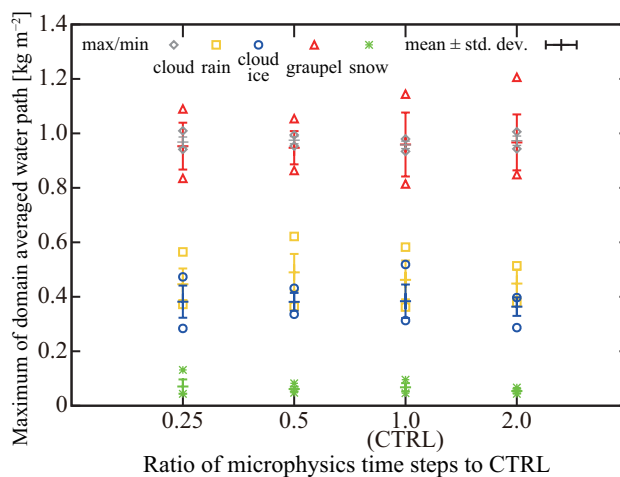


**Figure 15.** Statistics of the DT ensemble maximum water path for each hydrometeor type. The horizontal axis represents the ratio of cloud microphysics time steps to CTRL. This figure has the same form as Fig. 10, except for the difference in the horizontal axis.



## 9.1 Origins of odd particles

Let us determine the origins of the four types of odd particles denoted by symbols in Figs. 2 and 5–8. Once determined, we then modify the time evolution equations to resolve three of the four issues in effect.

### 9.1.1 Long, slowly falling hailstones

- 5 The ice particle denoted by the circle at  $t = 3000$  s is an example of hailstones that are too long and slowly falling. The attributes related to this ice particle’s morphology are  $\{a, c, \rho^i, m^{\text{rime}}/m, n^{\text{mono}}\} = \{2.58 \text{ mm}, 36.1 \text{ mm}, 1.12 \times 10^2 \text{ kg m}^{-3}, 0.98, 213\}$ . Therefore, this ice particle is categorized as a hailstone. However, the aspect ratio is  $> 10$ , which is unrealistically long for a hailstone. Because of the odd shape, its terminal velocity  $v^\infty = 4.25 \times 10^{-1} \text{ m s}^{-1}$  is also much smaller than that of typical hailstones (Fig. 8). It is located at  $(x, z) = (20.0 \text{ km}, 4.11 \text{ km})$ , which is near the freezing level (see Fig. 2).
- 10 This odd particle was caused by a problem with the riming density formula (54)–(56). By analyzing this particle’s history, we found that it was created by only a single collision-riming event between a graupel particle and a similarly sized rain droplet. The mechanism can be explained as follows: Consider the collision-riming of a quasi-spherical columnar graupel particle with a radius of 1 mm and a rain droplet with a radius slightly smaller than 1 mm. Assume also that the ambient temperature is slightly lower than  $0^\circ\text{C}$ . Then, from Eqs. (54)–(56),  $\rho_{\text{rime}} = 0.1 \text{ g cm}^{-3}$ . That is, the apparent volume of the rimed rain droplet
- 15 expands 10-fold. Because of the “filling in” model we employed for riming outcome (see Sec. 4.1.10), the resultant ice particle became a long columnar hailstone:  $(a, c) = (1 \text{ mm}, 11 \text{ mm})$ .

However,  $\rho_{\text{rime}} = 0.1 \text{ g cm}^{-3}$  must be reconsidered. Equation (55) has a global maximum of approximately  $0.95 \text{ g cm}^{-3}$  at around  $Y = 3.7$  and then quickly decreases, becoming  $< 0.1 \text{ g cm}^{-3}$  at around  $Y = 5.5$ . Then, from Eq. (54),  $\rho_{\text{rime}} = 0.1 \text{ g cm}^{-3}$  for  $Y > 5.5$ . As a result, considering the definition  $Y := (-r_k v_{\text{imp}}/T_j^{\text{sfc}})/(\mu \text{ m ms}^{-1}/^\circ\text{C})$ ,  $\rho_{\text{rime}} = 0.1 \text{ g cm}^{-3}$

20 frequently happens near the freezing level. For example,  $Y = 1000$  for  $r_k = 1 \text{ mm}$ ,  $v_{\text{imp}} = 1 \text{ ms}^{-1}$ , and  $T_j^{\text{sfc}} = -1^\circ\text{C}$ . However,  $\rho_{\text{rime}}$  would be much larger and even closer to  $\rho_{\text{true}}^i$  in such a situation in reality as the rimed droplet freezes very slowly. Therefore, we argue that Eq. (55) is valid only up to  $Y = 3.5$  and levels off after that. This correction can be made by simply replacing the  $Y$  value in Eq. (55) (but not in Eq. (56)) with

$$Y^\downarrow = \min(Y, 3.5). \quad (95)$$

- 25 In Sec. 9.1.5, we will confirm that this correction eliminates those long hailstones (Figs. 16–19).

Additionally, the same problem happens if a quasi-spherical planar graupel particle and a slightly smaller rain droplet collide and rime near the freezing level. However, it is less evident than with the previous case as the equatorial radius grows as the square root of the volume (Eq. (52)). Regardless, this problem can also be addressed using the above correction.

### 9.1.2 Columns with steep mass-dimension relationship

- 30 The square at  $t = 3000$  s indicates another odd particle. If we look around the square in Figs. 5 and 6, we see that this particle belongs to a population of columnar cloud ice particles that have a steeper mass-dimension relationship than observed. The



attributes related to this cloud ice particle's morphology are  $\{a, c, \rho^i, m^{\text{rime}}/m, n^{\text{mono}}\} = \{24.9\mu\text{m}, 138.8\mu\text{m}, 269.7\text{kg m}^{-3}, 0.29, 1\}$ . Its terminal velocity is  $v^\infty = 1.46 \times 10^{-2} \text{m s}^{-1}$  and it is located at  $(x, z) = (20.3\text{km}, 11.0\text{km})$  (see Fig. 2).

Like the previous case, we found that a single collision-riming event between a cloud ice particle and a cloud droplet followed by depositional growth created this columnar ice particle type. The mechanism can be explained as follows: Consider a quasi-spherical columnar ice particle with a radius of  $10\mu\text{m}$  and a supercooled droplet of radius slightly smaller than  $10\mu\text{m}$ . Assuming an impact velocity of  $10^{-2} \text{m s}^{-1}$  and ambient temperature of  $-10^\circ\text{C}$ , then, from Eqs. (54)–(56),  $Y = 10^{-2}$  and  $\rho_{\text{rime}} = 0.1 \text{g cm}^{-3}$ . That is, the apparent volume of the rimed droplet expands 10-fold, and create a columnar graupel particle:  $(a, c) = (10\mu\text{m}, 110\mu\text{m})$ , due to our riming outcome model's "filling in" assumption. Then, through subsequent depositional growth, this columnar graupel particle turns back into a columnar cloud ice particle.

Contrary to the previous case, the low riming density is reasonable. Instead, the "filling in" model must be reconsidered. We assumed that the ice particle's maximum dimension is preserved, but this is not realistic for riming between an ice particle and a similarly sized droplet, as our thought experiment revealed. Generalizing the idea, we consider that the frozen droplet's diameter is preserved if the diameter is larger than the ice particle's maximum dimension. That is, we propose to replace Eq. (49) with

$$a'_j = \max(a_j, r_k(\rho^w/\rho_{\text{rime}})^{1/3}), \quad (96)$$

and Eq. (53) with

$$c'_j = \max(c_j, r_k(\rho^w/\rho_{\text{rime}})^{1/3}). \quad (97)$$

In Sec. 9.1.5, we will confirm that those columns that follow a too steep mass-dimension relationship can be eliminated using this correction (Figs. 16–19).

### 9.1.3 Low-density hailstones

The cross at  $t = 3000\text{s}$  represents a hailstone with very low apparent density. The attributes related to this hailstone's morphology are  $\{a, c, \rho^i, m^{\text{rime}}/m, n^{\text{mono}}\} = \{12.6\text{mm}, 15.0\text{mm}, 10.7\text{kg m}^{-3}, 0.85, 1585116\}$ . Its terminal velocity is  $v^\infty = 4.31 \text{m s}^{-1}$  and it is located at  $(x, z) = (10.6\text{km}, 11.5\text{km})$  (see Fig. 2). What is unusual here is the very low apparent density  $\rho^i = 10.7 \text{kg m}^{-3}$ . This particle is composed of many monomers  $n^{\text{mono}} = 1585116$ , and we set the limiting value of aggregate density in Eq. (61) to  $\rho_{\text{crt}}^i = 10 \text{kg m}^{-3}$ . Thus, we can conclude that this hailstone is created by repeated collision-aggregation between graupel particles.

Lump graupel particles with apparent densities as low as  $50 \text{kg m}^{-3}$  were reported in Locatelli and Hobbs (1974). Therefore, a hailstone with an apparent density of  $10 \text{kg m}^{-3}$  is not extremely unrealistic. However, our aggregation model is crude. Following Morrison and Grabowski (2010), we assumed that collision-aggregation collection efficiency is a fixed constant of  $E_{\text{agg}} = 0.1$  regardless of morphology or temperature. It is thus plausible that this is causing the accumulation of graupel particles near the limiting value  $\rho_{\text{crt}}^i$  in Fig. 7. Future further detailed study to assess our aggregation model's applicability to graupel particles is required. See also Sec. 9.2.7, which provides a discussion to refine our aggregation model.



### 9.1.4 Long graupel particles

The triangle at  $t = 5400\text{s}$  is a very long graupel particle with a very low apparent density. The attributes related to this cloud ice particle's morphology are  $\{a, c, \rho^i, m^{\text{rime}}/m, n^{\text{mono}}\} = \{31.9\mu\text{m}, 438.2\mu\text{m}, 19.4\text{kg m}^{-3}, 0.53, 26679\}$ . Its terminal velocity is  $v^\infty = 1.02 \times 10^{-3}\text{ m s}^{-1}$ , it is located at  $(x, z) = (29.7\text{ km}, 6.4\text{ km})$  (see Fig. 2), and the ambient temperature is  
5  $T = -14.4^\circ\text{C}$ .

This particle is created by the sublimation of a graupel particle. The inherent growth ratio  $\Gamma(T)$  proposed by Chen and Lamb (1994a) was used to calculate the deposition and sublimation process as described in Sec. 4.1.7.  $\Gamma(T) < 1$  if  $T$  is in the range of approximately  $[-20^\circ\text{C}, -10^\circ\text{C}]$  and  $[-5^\circ\text{C}, 0^\circ\text{C}]$ ; therefore, in this temperature range, ice particles grow to become planar through deposition and shrink to become columnar by sublimation.

10 However,  $\Gamma(T)$  was derived from measurements of depositional growth, hence it is questionable whether it is applicable for sublimation. As Harrington et al. (2019) and references therein indicated,  $\Gamma(T)$  should be considered as unity for sublimation,

$$\Gamma(T_i) = 1, \quad \text{for } dm_i < 0 \text{ (sublimation),} \quad (98)$$

thus, the aspect ratios of ice particles are preserved during sublimation.

In Sec. 9.1.5, we will confirm that those long graupel particles can be eliminated using this correction (Figs. 16–19).

### 15 9.1.5 Results after corrections

We proposed three corrections to the time evolution equations (Eq. (95)–(98)) in the preceding sections to avoid the creation of ice particles with unrealistic morphologies.

We incorporated the proposed corrections into our model to create a new revision, SCALE-SDM 0.2.5-2.2.1. To assess the validity of these corrections, we conducted the same simulations as the typical realization of CTRL using the new model. By  
20 comparing the results (Figs. 16–19) with the original results (Figs. 5–8), we confirm that the three types of odd ice particles no longer exist, as we intended. See also Movies 7–11 in the Supplement. Note that we left the issue of low density hailstones for future study. These corrections have little effect upon the overall cloud properties, i.e., spatial structure (Movie 7 in the Supplement), time evolution of water path (Fig. 20), and accumulated precipitation amount (Fig. 21).

## 9.2 Further sophistication of the model

25 Our model is based on kinetic description, i.e., individual dynamics of particles and their stochastic collisions. However, quantitative understanding of mixed-phase cloud microphysics is a long-standing meteorological issue and kinetic description of mixed-phase cloud microphysics has not been established. Further, our model does not incorporate several elementary processes that are important for mixed-phase clouds. In this section, we explore the possibilities of further refining and sophisticating our model. Readers may also refer to Chen and Lamb (1994a, b), Misumi et al. (2010), Hashino and Tripoli (2007,  
30 2008, 2011a, b), Jensen and Harrington (2015), Sölch and Kärcher (2010), Brdar and Seifert (2018), and Seifert et al. (2019), as these are modeling studies closely relevant to our study.

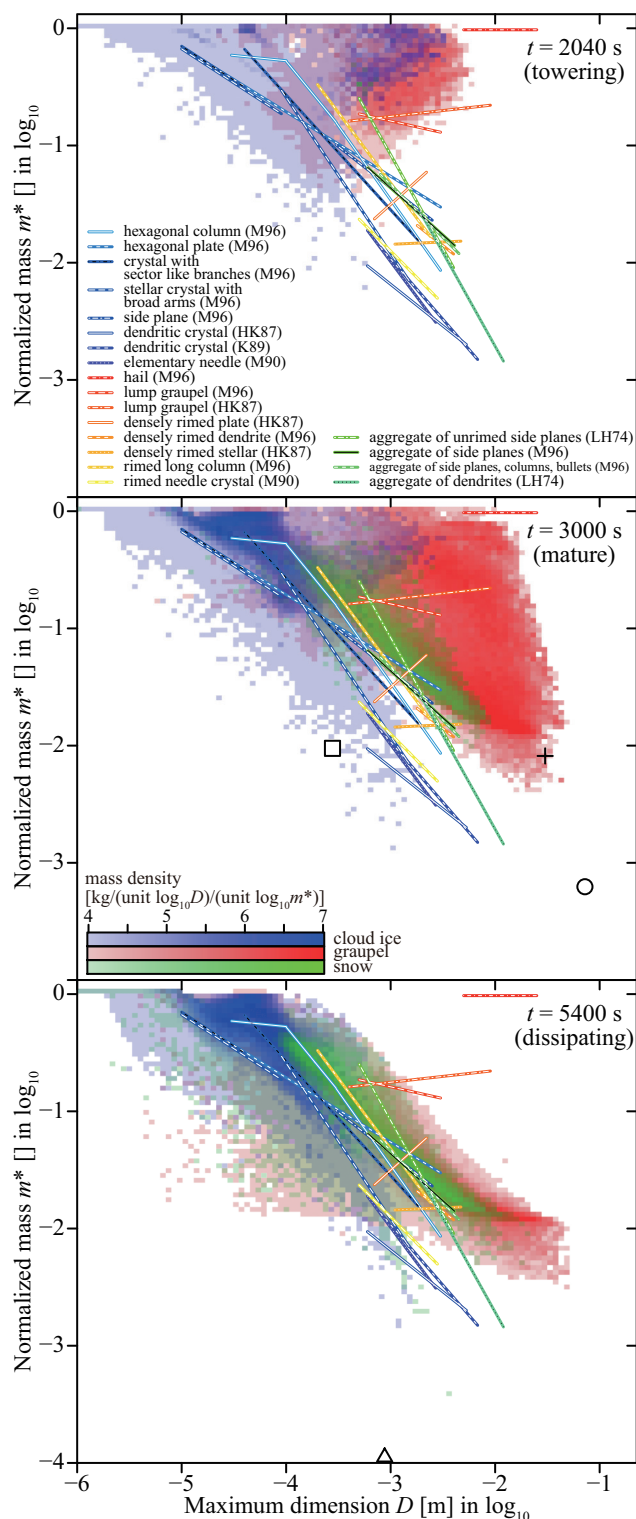


**Figure 16.** This figure is the same as Fig. 5 but shows results from the corrected model. See also Movie 8 in the Supplement.

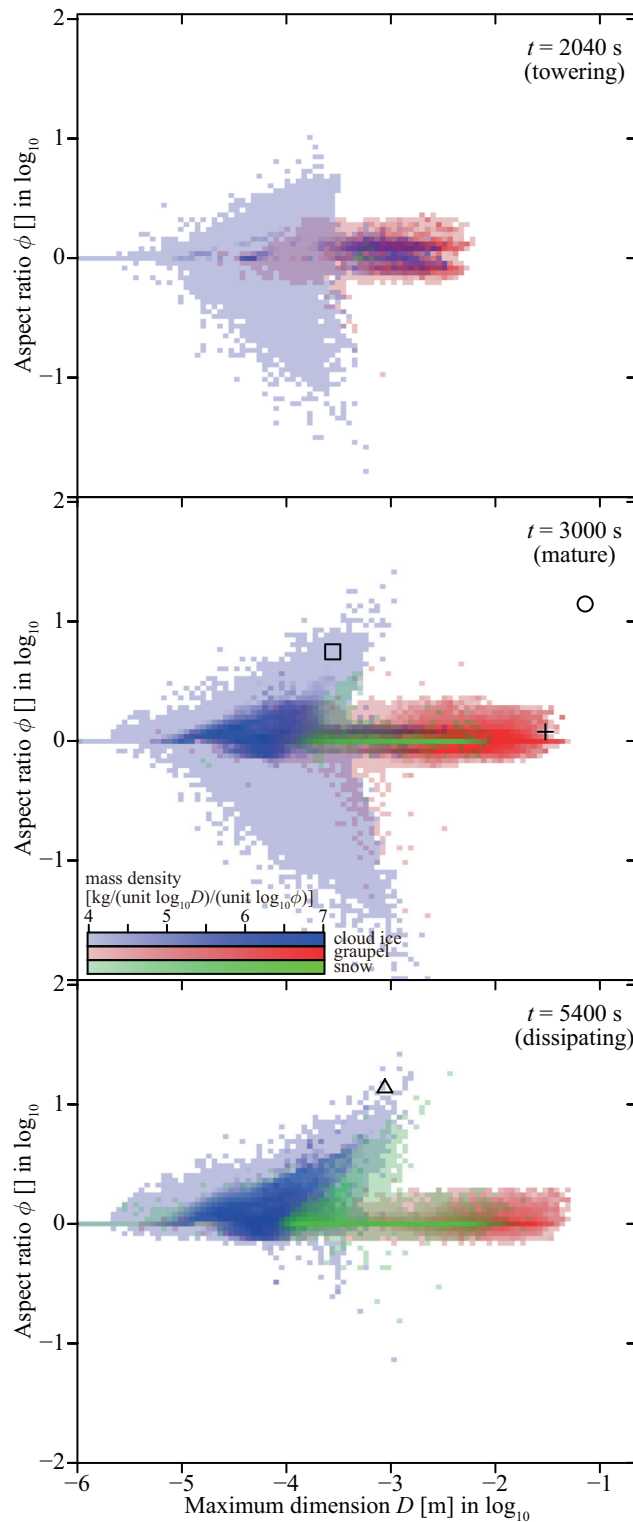


**Figure 17.** This figure is the same as Fig. 6 but shows results from the corrected model. See also Movie 9 in the Supplement.

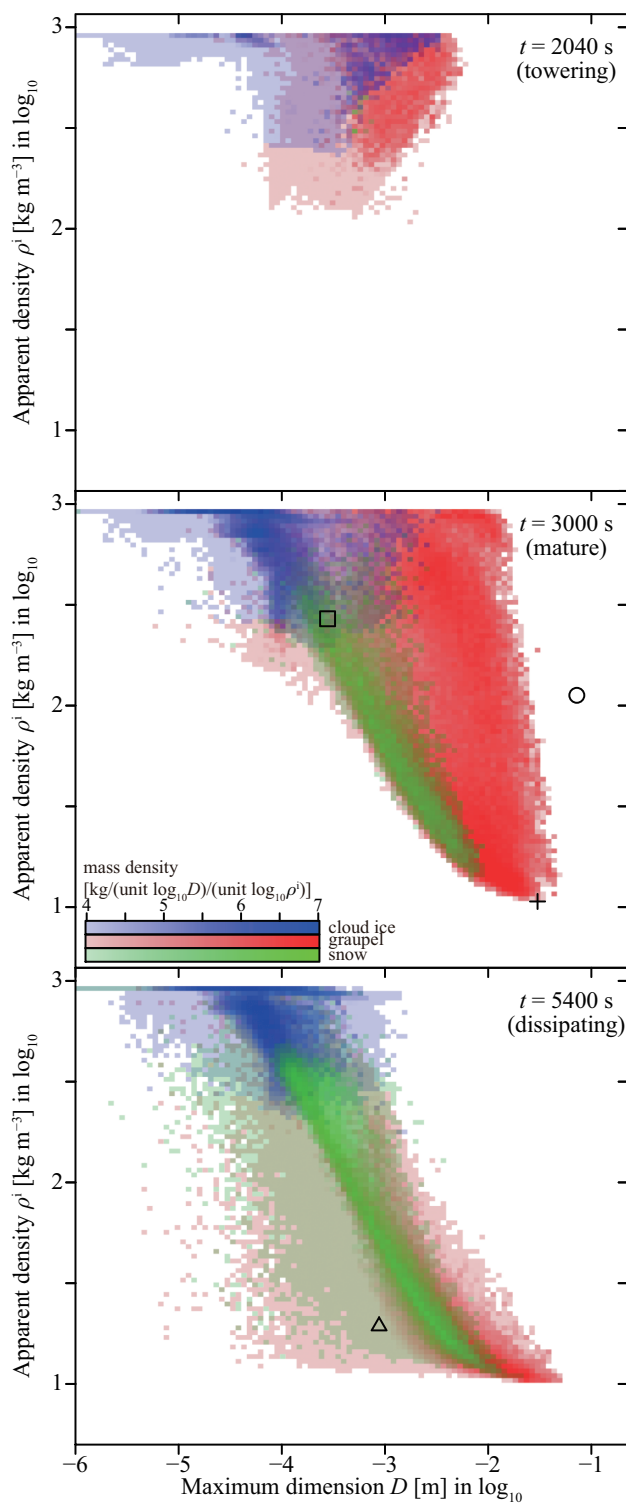


**Figure 18.** This figure is the same as Fig. 7 but shows results from the corrected model. See also Movie 10 in the Supplement.

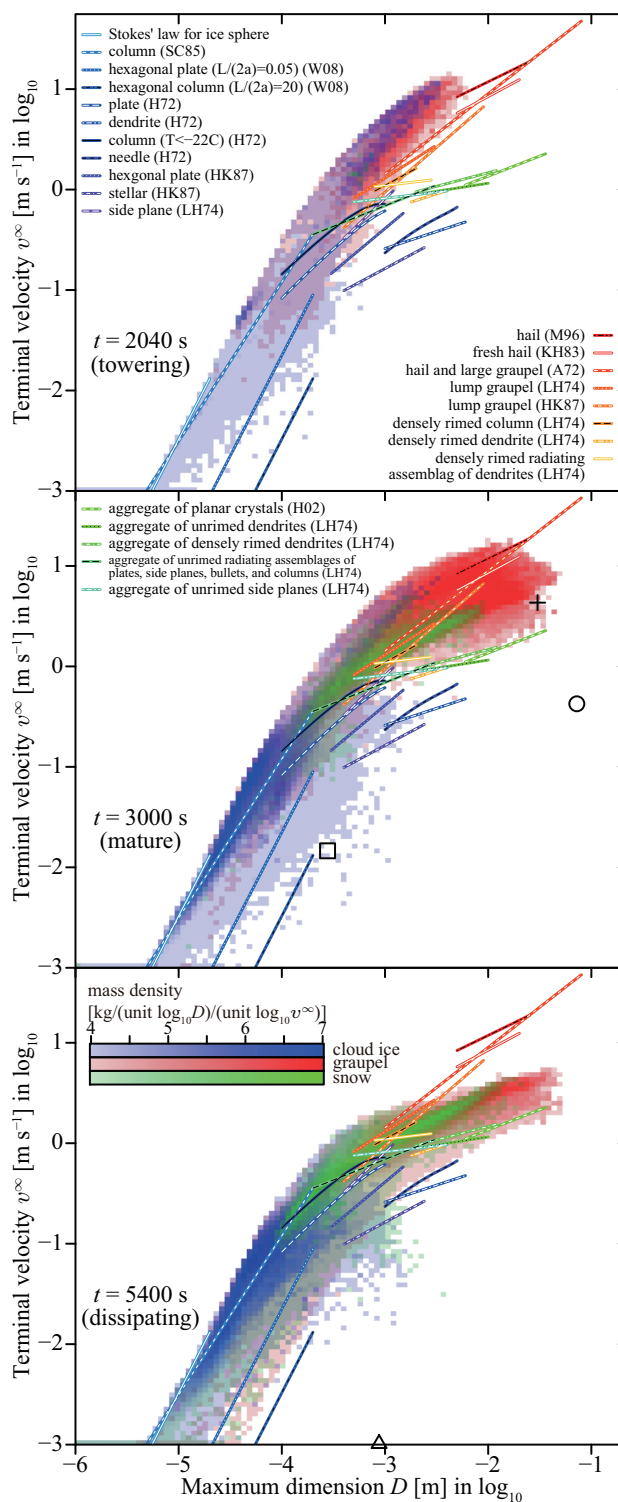


**Figure 19.** This figure is the same as Fig. 8 but shows results from the corrected model. See also Movie 11 in the Supplement.

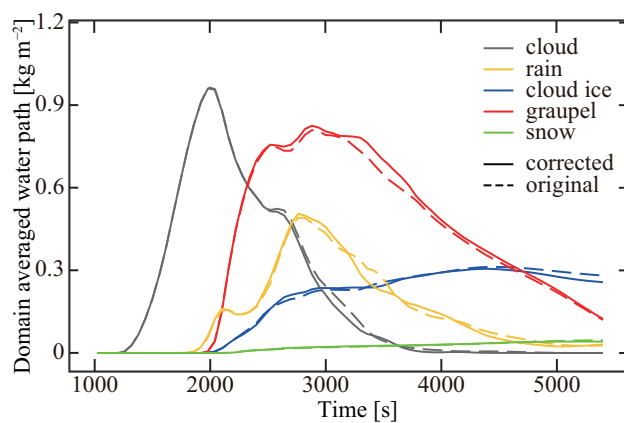


**Figure 20.** Changes in the domain-averaged water path before and after corrections. The solid and dashed lines represent the corrected and original models, respectively.

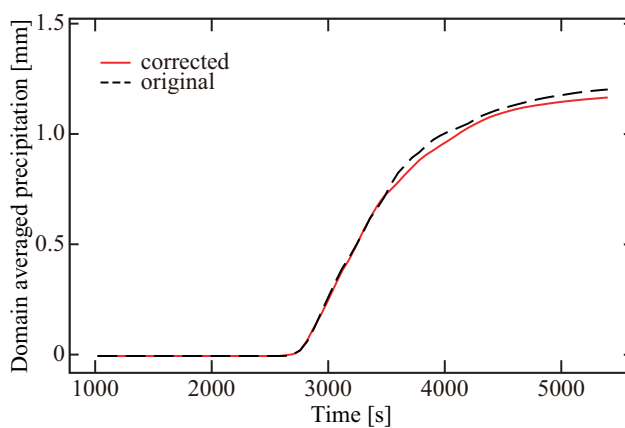


**Figure 21.** Changes in accumulated precipitation amounts before and after corrections. The solid and dashed lines represent the corrected and original models, respectively.



### 9.2.1 Ice nucleation pathways

There are various ice nucleation pathways (e.g., Kanji et al., 2017); however, in this study, we only considered condensation/immersion freezing and homogeneous freezing, as these are the dominant mechanisms in mixed-phase clouds.

Based on the “singular hypothesis” (Levine, 1950), we considered that each insoluble particle has its own freezing temperature  $T^{\text{fz}}$  that can be determined by INAS formulas. In the model evaluation experiments, we assumed that ice nuclei consist of mineral dust and used the INAS formula of Niemand et al. (2012). Formulas from Wex et al. (2015) and Ullrich et al. (2017) can be used for biogenic substances and soot, respectively.

Time dependence of ice nucleation is ignored in the “singular hypothesis”, thus it is assumed that particles initiate freezing immediately after the temperature drops below  $T^{\text{fz}}$  and the ambient air becomes saturated over liquid water. However, time dependence of ice nucleation could be important for clouds with long lifetimes, something known as the “stochastic hypothesis”. The Soccer Ball Model of Niedermeier et al. (2011, 2014, 2015), which is based on classical nucleation theory, could be used to incorporate time dependence. Then, instead of freezing temperature  $T^{\text{fz}}$ , the contact angle of surface site  $\theta$  must be treated as an attribute.

To express homogeneous freezing, we assigned a fixed freezing temperature of  $T^{\text{fz}} = -38^\circ\text{C}$  to all IN inactive particles and ignored the time dependence of ice nucleation. However, this is not appropriate for the homogeneous freezing of deliquescent aerosol particles as homogeneous ice nucleation is suppressed when solute concentration increases. Additionally, time dependence of ice nucleation could be also important as the probability that a droplet freezes homogeneously is proportional to liquid water volume. These effects can all be incorporated using the model of Koop et al. (2000).

Condensation/immersion freezing of deliquescent IN particles can also be incorporated by considering the depression of the freezing temperature  $T^{\text{fz}}$  by solute (see Wex et al., 2014, and references therein). Alternatively, a model based on classical nucleation theory proposed by Khvorostyanov and Curry (2004, 2005) can be used to incorporate time dependence.

The formation of ice directly from the vapor phase onto an IN particle is known as deposition freezing. This can be observed at  $< -25^\circ\text{C}$  and in air that is below water saturation. Marcolli (2014) suggested that the phenomena conventionally known as deposition freezing can be reinterpreted as pore condensation and freezing. We can use the temperature-dependent and saturation-ratio-dependent INAS formula proposed by Steinke et al. (2015) to incorporate this process. Here, INAS density  $n_S$  is a function of  $x_{\text{therm}}$  and  $x_{\text{therm}}$  is a function of temperature  $T$  and saturation ratio over ice  $S^i$ . We can assign  $x_{\text{therm},i}$  to each particle as an attribute. We consider that freezing occurs if  $x_{\text{therm}}(T, S^i) > x_{\text{therm},i}$ .

Contact freezing is another ice nucleation mechanism in which solid particle can initiate freezing upon contacting the surface of a supercooled droplet. Contact freezing occurs at temperatures greater than that of the same particle immersed in a droplet (e.g., Shaw et al., 2005); therefore, it might also be relevant to mixed-phase clouds. To explain the scavenging of aerosol particles by droplets, Brownian diffusion and phoretic forces must be considered. This process can be incorporated into our model by introducing the collision-coalescence kernels detailed in Sec. 17.4.2 of Pruppacher and Klett (1997). Then, based on the results of Shaw et al. (2005), as suggested by Will H. Cantrell (2017, private comm.), contact freezing may well be expressed by increasing the particle’s  $T^{\text{fz}}$  by  $4.5^\circ\text{C}$  in each single particle-droplet collision event. Another possibility is using



laboratory data from Niehaus et al. (2014), who measured the freezing efficiency of various insoluble particles, which can be interpreted as the probability that each single particle-droplet collision results in a freezing event.

It is also known that the evaporation of a droplet could lead to inside-out contact freezing (e.g., Durant and Shaw, 2005); however, there are still substantial uncertainties.

## 5 9.2.2 Onset of melting

We assumed that ice particles start melting immediately after the ambient temperature reaches  $> 0^\circ\text{C}$ . However, evaporative cooling delays melting onset. For example, at a relative humidity of 50%, melting begins at  $+4^\circ\text{C}$ . We can incorporate this effect by considering ice particle surface temperatures as discussed in Rasmussen and Pruppacher (1982).

## 9.2.3 Partially frozen/melted particles

10 After the onset of freezing or melting, we assumed that complete freezing/melting occurs instantaneously.

However, as shown in Murray and List (1972), the freezing time of millimeter-size droplets can be of the order of 100s. We can explicitly incorporate this process using the time evolution equation summarized in Sec. 16.1.4 of Pruppacher and Klett (1997), which is derived from a quasi-steady assumption of vapor and thermal diffusion around a partially frozen droplet.

15 We also assumed that rimed supercooled droplets freeze instantaneously; however, wet growth of graupel particles is important for accurately predicting hailstone formation. We can use the model from Rasmussen and Heymsfield (1987) to incorporate the wet growth process.

20 Depending on relative humidity and warming rate, the melting time of spherical ice particles with radii of approximately  $300\text{--}400\mu\text{m}$  ranges between 20–70s (Rasmussen and Pruppacher, 1982). It is well known that a large hailstone can escape complete melting and reach the ground. Shedding of droplets can also occur if a partially melted hailstone contains excess melt water, which can affect the raindrop size distribution below the cloud. Partially melted snow aggregates can create a layer of stronger radar reflectivity below the melting level, known as a “bright band”. We can explicitly incorporate these processes explicitly using the model summarized in Phillips et al. (2007).

Additionally, to make the model complete, all other time evolution equations must be extended to make them compatible with partially frozen/melted particles, which would require some effort.

## 25 9.2.4 Condensation and evaporation

In SCALE-SDM, we assumed that water vapor’s diffusivity in air and moist air’s thermal conductivity in Eq. (8) are fixed constants,  $D_v = 2.52 \times 10^{-5} \text{m}^2\text{s}^{-1}$  and  $k = 2.55 \times 10^{-2} \text{Jm}^{-1}\text{s}^{-1}\text{K}^{-1}$ , which are the values for  $T = 20^\circ\text{C}$  and  $p = 1000 \text{hPa}$ . However, this approximation is erroneous, in particular because diffusivity  $D_v$  is inversely proportional to pressure. In the case of the initial profile we used for model evaluation,  $T = -44^\circ\text{C}$  and  $p = 250 \text{hPa}$  at  $z = 10 \text{km}$ . Thus,  $D_v = 6.08 \times 10^{-5} \text{m}^2\text{s}^{-1}$ ,  
30 which is about 2.4 times larger than we assumed. The temperature and pressure dependence of water vapor’s diffusivity in air



$D_v$ , and the temperature dependence moist air's thermal conductivity  $k$  must be considered. The formulas summarized in Sec. 13.1 of Pruppacher and Klett (1997) can be used.

We considered the ventilation effect for deposition and sublimation but not for condensation and evaporation, even though it also enhances the growth and evaporation of larger droplets. We can include this effect by using the model described in 5 Sec. 13.2.3 of Pruppacher and Klett (1997).

For cloud droplets, kinetic correction to  $D_v$  and  $k$  must also be considered. See, e.g., Sec. 13.1 of Pruppacher and Klett (1997) and Kogan (1991).

In our model, aerosol particle hygroscopicity is expressed by Raoult's law with the van't Hoff factor  $i$  (Low, 1969); however, using the kappa parameterization of Petters and Kreidenweis (2007) would be more convenient.

## 10 9.2.5 Deposition and sublimation

There are many issues around  $\Gamma(T)$ , which represents the primary growth habit of ice crystals. Considering the amount of data used for the fitting, the proposed shape of  $\Gamma(T)$  is subject to large uncertainties (see Fig. 3 of Chen and Lamb, 1994a). The applicable range is also not clear. We set  $\Gamma(T) = 1$  for small ice crystals  $D < 10\mu\text{m}$ . As discussed in Sec. 9.1.4,  $\Gamma(T) = 1$  should be used for sublimation (Harrington et al., 2019, and references therein). We may need to use some other form of  $\Gamma(T)$  15 for graupel particles and snow aggregates. Connolly et al. (2012) had to adjust  $\Gamma(T)$  somewhat arbitrarily to obtain a better agreement.

Further, as shown by Kumai (1982) and Bailey and Hallett (2004), at  $T < -20^\circ\text{C}$  both plates and columns can be created at the same temperature depending on saturation ratio over ice  $S^i$ , and polycrystals can also be created. Therefore, for  $T < -20^\circ\text{C}$ ,  $\Gamma$  may better be considered a function of both  $T$  and  $S^i$ , and formation of polycrystals must be somehow incorporated 20 into our model. We can employ the mathematical model from Hashino and Tripoli (2008), which extends Chen and Lamb (1994a)'s model to describe these behaviors.

Harrington et al. (2019) reformulated the model from Chen and Lamb (1994a), and their model does not rely on  $\Gamma(T)$ , predicting the aspect-ratio evolution using the "facet-based hypothesis". The model is as good as Chen and Lamb's original model at liquid saturation, and further, it can be applied to wider range of environmental conditions, such as low supersaturation 25 and low pressure. However, it is still unclear how well the model would work for polycrystals or irregular ice particles.

We used Chen and Lamb (1994a)'s deposition density formula; however, as discussed in Jensen and Harrington (2015), their formula does not capture the wind tunnel data of Takahashi et al. (1991) very well. Instead, Jensen and Harrington (2015) proposed a simple formula:  $\rho_{\text{dep}} = \rho_{\text{true}}^i \Gamma(T)$  for  $\Gamma < 1$ ;  $\rho_{\text{dep}} = \rho_{\text{true}}^i / \Gamma(T)$  for  $\Gamma > 1$ . Their idea to relate deposition density  $\rho_{\text{dep}}$  to axis growth ratio is plausible, but its dependence on  $S^i$  is lost. Because  $\rho_{\text{dep}}$  accounts for the secondary growth habit, 30 dependence on  $S^i$  must be reconsidered.

In our model, each ice particle is approximated by a porous spheroid  $(a, c, \rho^i)$ . We used spheroid capacitance  $C(a, c)$  to evaluate  $C$  in Eq. (10). However, the spheroid  $(a, c)$  represents the ice particle's spatial extent, and it may have a more detailed internal structure, which is represented by the apparent density  $\rho^i$ . Actual ice particle capacitance also depends on internal structure. Westbrook et al. (2008) accurately calculated the capacitance of realistic ice particles by directly simulating the



trajectories of diffusing water molecules. Thus, we can use their formulas to refine our model's accuracy. For example, they showed that the capacitance of snow aggregates can be approximated by  $C = D/4$ , which is half that of a sphere.

As with condensation and evaporation, we assumed that water vapor's diffusivity in air  $D_v$  and moist air's thermal conductivity  $k$  in Eq. (11) are fixed constants, but this must be revised.

5 Demange et al. (2017) constructed a sophisticated phase field model for ice crystal growth that successfully reproduced the formation of diverse ice crystal shapes. This model could help us construct a more accurate kinetic description of deposition and sublimation processes.

### 9.2.6 Riming

For the collection efficiency of collision-riming  $E_{\text{rime}}$  when a large spherical ice particle collects a supercooled droplet, we used the formula from Beard and Grover (1974) with a mixed Froude number (Eqs.(39) and (40)). von Blohn et al. (2009) demonstrated that the formula underestimates the efficiency if the spherical ice particle is large, but Eq. (11) in their paper seems to be incorrect and thus we did not take this into account.

When a large droplet collects ice particles, we used the original formula from Beard and Grover (1974) approximating the ice particle is spherical. To consider ice particle shape, formulas from Lew and Pruppacher (1983) can be used for a large droplet collecting small columns, and Lew et al. (1985) for a large droplet collecting small planar crystals.

Beard and Grover (1974)'s formula is valid only for  $p < 0.1$ , where  $p$  is the size ratio of the collector ice/droplet and collected droplet/ice. We forcibly applied the formula beyond this range, which increases the collection efficiency of riming between small similar size droplets and ice particles, as  $E_{\text{BG74}}(p, N_{\text{Re}}, N_{\text{St}}) \approx p^2/(1 + p^2)$  for  $N_{\text{St}} \ll 1$ . This must be corrected.

When an ice particle collects a droplet, we employed the filling in model and preserved the ice particle's maximum dimension. However, if the collector is a snow aggregate, we should use the similarity model proposed by Seifert et al. (2019). Unrimed/rimed snow aggregates have fractal structures, and Seifert et al. (2019) found a universal self-similar relation in snow aggregate growth through riming. The similarity model properly considers the maximum dimension's increase during the early stages of riming, which can lead to more rapid ice particle growth due to riming.

### 9.2.7 Aggregation

25 We assumed that collision-riming's collection efficiency is given by a constant  $E_{\text{agg}} = 0.1$  following Morrison and Grabowski (2010), but this is a simplification.  $E_{\text{agg}}$  should be larger for large particles (due to the interlocking mechanism) and near water-saturated conditions.  $E_{\text{agg}}$  can be decomposed into  $E_{\text{agg}} = E_{\text{coll}}E_{\text{stick}}$ , where  $E_{\text{coll}}$  is collision efficiency and  $E_{\text{stick}}$  is sticking efficiency. For  $E_{\text{coll}}$ , the formula of Böhm (1989, 1992a, b, c, 1994, 1999) can be used. For  $E_{\text{stick}}$ , Pruppacher and Klett (1997, Sec. 16.2) provides a simple formula that depends solely on temperature. The  $E_{\text{stick}}$  formula provided by Phillips et al. (2015) is physically based and should thus be more reliable.

Calculating resultant ice particles is also not easy. Let  $(a', c', \rho^i, m^{\text{rime}'}, n^{\text{mono}'})$  be the ice particle created by the collision-aggregation of  $(a_1, c_1, \rho_1^i, m_1^{\text{rime}}, n_1^{\text{mono}})$  and  $(a_2, c_2, \rho_2^i, m_2^{\text{rime}}, n_2^{\text{mono}})$ . For rime mass and number of monomers,  $m^{\text{rime}'} = m_1^{\text{rime}} + m_2^{\text{rime}}$  and  $n^{\text{mono}'} = n_1^{\text{mono}} + n_2^{\text{mono}}$  hold. To determine the remainder,  $(a', c', \rho^i)$ , specifying two out of the three



attributes is sufficient because of the conservation of total mass. In this study, as in the case of riming, we assumed that the filling in model can be applied to aggregation, i.e., the maximum dimension is conserved and only the minor axis grows. Therefore,  $D' = \max(D_1, D_2) = \max(a_1, c_1) + \max(a_2, c_2)$ . However, one more attribute must be specified. In this study, instead of predicting minor axis growth, we predict the apparent density  $\rho^{i'}$  by introducing an intuitive model that considers the compaction of fluffy snowflakes. As a result, the fractal dimension of the mass-dimension relationship of snow aggregates predicted by our model is close to 2 (see the green shade in Figs. 5 and 16), which agrees well with various previous studies (e.g., Brown and Francis, 1995; Heymsfield et al., 2010; Mitchell, 1996; Schmitt and Heymsfield, 2010).

However, the filling in assumption is not valid for collision-aggregation. Higuchi (1960) introduced a parameter called the separation ratio:  $s := 2l/(D_1 + D_2)$ ,  $s \in [0, 1]$ , where  $l$  is the horizontal distance between the centers of the two particles. For an aggregation between two planar ice particles, the resultant ice particle's maximum dimension can be evaluated by  $D' = \max\{D_1, D_2, (1 + s)(D_1 + D_2)/2\}$ . Our model corresponds to the special case  $s = 0$ , but it has been reported that  $s \approx 0.5$ – $0.6$  for two planar crystals and dendrites (Higuchi, 1960; Kajikawa and Heymsfield, 1989; Kajikawa et al., 2002), and  $s \approx 0.9$  for spatial dendrites (Kajikawa et al., 2002). In contrast,  $s = 0$  for columnar ice crystals can be justified from Kajikawa (1995)'s observation that two needles of similar sizes tend to attach with their centers close ( $s \approx 0$ ) and a right angle between their polar axes (crossed adhesion). It is also interesting to note that cross adhesion displacement gives the largest possible volume  $V_{\max}$ , which we used to calculate the apparent density  $\rho^{i'}$  of the resultant ice particle by interpolation.

Another issue of the filling in assumption is that it gradually makes snow aggregates quasi-spherical (see the green shades in Figs. 6 and 17). Measurements indicate that snow aggregates have an average aspect ratio of 0.6 (e.g., Korolev and Isaac, 2003) or smaller (Jiang et al., 2017).

Introducing the separation ratio  $s$  in our model is straightforward, and could improve our model's accuracy. In general, this tends to reduce the mass-dimension relationship's fractal dimension, and their aspect ratio. Locatelli and Hobbs (1974) reported that aggregates of dendrites and aggregates of unrimed side planes had fractal dimensions of 1.4 (plotted in Figs. 5 and 16), which is smaller than 2.

In our model, apparent density  $\rho^{i'}$  after aggregation is predicted by the formula given in Eq. (61). It is natural to assume that there is a lower limit of apparent density; however, this is a crude expression of the idea and requires further validation and improvement. Also note that a contact angle model was used in Chen and Lamb (1994b) and Hashino and Tripoli (2011a) to determine the resultant ice particle.

Several numerical models can create detailed 3D structures of snow aggregates consisting of primary ice crystals (e.g., Westbrook et al., 2004a, b; Maruyama and Fujiyoshi, 2005; Schmitt and Heymsfield, 2010). Our collision-aggregation outcome model can be refined by using the results of those more microscopic models that resolve snow aggregate structures. For example, Przybylo et al. (2019) intensively studied the characteristics of aggregates composed of two monomers.

### 9.2.8 Spontaneous/collisional breakup

Several mechanisms can induce spontaneous/collisional breakup of hydrometeors; however, none of them are considered in the present study. In particular though, rime splintering (Findeisen and Findeisen, 1943; Hallett and Mossop, 1974), and the



collisional breakup of ice particles (Vardiman, 1978) are important in mixed-phase clouds, as these processes are thought to be responsible for the large excess in the observed number concentration of ice particles to the number concentration of IN aerosol particles (e.g., Field et al., 2017).

5 First, a particle-based numerical algorithm for calculating spontaneous/collisional breakup processes has not yet been established. A simple strategy is to add more super-particles to the system when a breakup event occurs, but this could be computationally inefficient.

Mathematical models of spontaneous/collisional breakup processes are available from various studies. For the spontaneous breakup of rain droplets  $> 6.5$  mm, the mathematical model from Kamra et al. (1991) can be used. For the collisional breakup of droplets, Seifert et al. (2005)'s model can be used. For the shedding of excess melt water, Phillips et al. (2007)'s model  
10 can be used. For rime splintering, the model summarized in Sec. 16.1.6 of Pruppacher and Klett (1997) can be used. Readers may also refer to Field et al. (2017) and the references cited therein. For the collisional breakup of ice particles, Phillips et al. (2017)'s model can be used.

On average, spontaneous/collisional breakup increases the number concentration of ice particles and rain droplets, and their sizes then become smaller, which results in a reduction of accumulated surface precipitation. This effect can be mimicked to  
15 some extent if we increase the number concentration of mineral dusts in our model.

### 9.2.9 Sub-grid scale turbulence

The grid size we tested for evaluating the model ranged from 31.25 m to 250 m, and only flows larger than the chosen grid size can be resolved. A substantial portion of turbulence kinetic energy is accumulated in large scales and small scale turbulence is mostly driven by large scale motions; therefore, SGS turbulence is of secondary importance to the phenomena. Nevertheless,  
20 SGS turbulence does affect moist air flow and atmospheric particle behavior. Appropriately incorporating SGS turbulence is desired to improve the model's grid convergence.

The Smagorinsky-Lilly model (Smagorinsky, 1963; Lilly, 1962; Brown et al., 1994; Scotti et al., 1993), which is already available in SCALE-SDM, can be used for the diffusion of moist air by SGS turbulence. However, we did not use it in this study because the model is designed for 3D turbulence.

25 SGS turbulence can enhance particle collision, which can be incorporated by using the collision kernels proposed in Wang et al. (2008), Onishi and Seifert (2016), and Chen et al. (2018). Particle velocity fluctuations due to SGS turbulence can be modeled as an Ornstein-Uhlenbeck process (e.g., Pope, 1994; Schilling et al., 1996; Grabowski and Abade, 2017). Fluctuation of supersaturation through eddy-hopping and entrainment can be considered by introducing a new stochastic attribute (Grabowski and Abade, 2017; Abade et al., 2018) or by applying the Linear Eddy model to particles (Hoffmann et al., 2019).

### 30 9.3 Numerical convergence and computational cost

As confirmed in Sec. 8, the numerical parameters used for the CTRL ensemble (see Table 1) can produce an accurate numerical solution of the cumulonimbus case.



The CTRL ensemble's super-particle number concentration is  $c^{\text{SP}} = 128/\text{cell}$ , which is comparable to various previous studies (e.g., Andrejczuk et al., 2010; Sölch and Kärcher, 2010; Riechelmann et al., 2012; Arabas and Shima, 2013; Unterstrasser and Sölch, 2014; Unterstrasser et al., 2017; Grabowski et al., 2018; Jaruga and Pawlowska, 2018; Dziekan et al., 2019; Hoffmann et al., 2019). In those studies, it was reported that approximately 50–200/cell of super-particles are needed to accurately simulate clouds in two or three dimensions. If the number of attributes is increased, we generally need more super-particles to cover the higher dimensional attribute space. In this study, we used 5 attributes to represent ice particles, which is relatively large compared to previous studies. Therefore, the fact that numerical convergence is achieved with a super-particle number concentration as low as 128/cell is a remarkable result that reveals the efficacy of a particle-based cloud modeling approach. Another example of studies using many attributes is Jaruga and Pawlowska (2018), which included 8 attributes to study aqueous-phase oxidation of sulfur to sulfate and confirmed that results do not change significantly if the number concentration of super-droplets is larger than 64/cell. Additionally, performance is sensitive to how super-particles are initialized (Unterstrasser et al., 2017), which we discussed in Sec. 5.3.

The CTRL ensemble's grid size is  $\Delta x = \Delta y = \Delta z = 62.5\text{ m}$ , which is highly dependent on the simulated cloud's energy injection scale. As discussed in Sec. 9.2.9, introducing SGS turbulence models should improve grid convergence characteristics.

The time steps for cloud microphysical processes used in the CTRL ensemble are  $(\Delta t_{\text{adv}}, \Delta t_{\text{tz/mlt}}, \Delta t_{\text{coal}}, \Delta t_{\text{cnd/evp}}, \Delta t_{\text{dep/sbl}}) = (0.4\text{ s}, 0.4\text{ s}, 0.2\text{ s}, 0.1\text{ s}, 0.1\text{ s})$ . As shown in Sec. 8.3, the DTx2 ensemble does not show any significant difference. Therefore, time steps twice as large or even larger could suffice. In the following, we discuss how those time steps are determined and whether the constraints can be relaxed.

To accurately trace the flow of moist air,  $\Delta t_{\text{adv}}$  should be limited by the CFL condition of wind velocity.

To avoid a sudden release of latent heat,  $\Delta t_{\text{tz/mlt}}$  must also be restricted by the CFL condition.

$\Delta t_{\text{coal}}$  is the time step of collision-coalescence, -riming, and -aggregation. From a simple argument, Shima et al. (2009) showed that  $\Delta t_{\text{coal}}$  can be estimated from the number concentration and size of real particles, and that  $\Delta t_{\text{coal}}$  does not depend on numerical parameters such as super-particle number concentration or grid size. To make the calculation robust to larger time steps, a technique to allow multiple coalescence, riming, and aggregation occurrences is implemented in the SDM; however, this does not work properly if the collected super-particle's multiplicity is not large enough. This issue could be improved by introducing a recursive algorithm (Okawa, 2015), which may allow us to use larger  $\Delta t_{\text{coal}}$  values.

$\Delta t_{\text{cnd/evp}}$  and  $\Delta t_{\text{dep/sbl}}$  are determined by the phase relaxation time of supersaturation,  $\tau_{\text{phase}} \propto 1/\sum \xi_i r_i$  (e.g., Cooper, 1989). The time scale of CCN activation/deactivation is normally much smaller than the phase relaxation time; however, our model is not constrained by the activation/deactivation time scale as the condensation and evaporation equation (7) is solved implicitly (see Sec. 5.5.3). However, we explicitly calculate the exchange of vapor and latent heat with moist air (see Sec. 5.5.3), thus,  $\Delta t_{\text{cnd/evp}}$  and  $\Delta t_{\text{dep/sbl}}$  must be smaller than the phase relaxation time. This restriction could be relaxed if we fully implicitly solve this coupled process of droplets and moist air. Perhaps the approach described in Sec. 2.6 of Grabowski et al. (2018) for mitigating spurious cloud-edge supersaturations can be used also for this purpose.

We used the first order operator splitting scheme to separate the calculation (Fig. 1). Employing higher order operator splitting and/or tendencies would also improve numerical convergence characteristics.



Lastly, we discuss SCALE-SDM's actual computational cost. Calculating one realization of the CTRL case required approximately 10 hours using 160 Intel Xeon E5-2650v3 CPU cores. To compare computational cost, we also tried the two-moment bulk scheme of Seiki and Nakajima (2014) implemented on SCALE. This took approximately 20 minutes, which is about 30 times faster than SDM. Because SDM's computational cost scales linearly with the number of super-particles and the number concentration of super-particles for the CTRL case was 128/cell, this is a plausible result. We can solve the same mathematical model using a multi-dimensional bin scheme. Let us also estimate the bin model's computational cost. The effective number of attributes we used for ice particles is 5, meaning that the bin space is 5-dimensional. If we assume that 10–100 bins are needed for each axis, the total number of bins becomes  $10^5$ – $100^5$ . Due to the binary collision calculation, the bin model's computational cost scales with the square of the number of bins, i.e.,  $10^{10}$ – $100^{10}$ . This is much larger than 100, i.e., the computational cost of SDM.

In SCALE-SDM, super-particles are distributed all over the simulated domain. If we use super-particles only inside the clouds by employing, e.g., the Twomey super-droplet methodology (Grabowski et al., 2018), computational costs can be considerably reduced.

## 10 Conclusions

Using SDM, we constructed a detailed numerical model of mixed-phase clouds based on kinetic description and subsequently demonstrated that a large-eddy simulation of a cumulonimbus which predicts ice particle morphology without assuming ice categories or mass-dimension relationships is possible. Our results strongly support the particle-based modeling methodology's efficacy for simulating mixed-phase clouds.

In our model, ice particles are approximated by porous spheroids. The elementary cloud microphysics processes the model considers include advection and sedimentation; immersion/condensation, and homogeneous freezing; melting; condensation and evaporation including the activation and deactivation of CCNs; deposition and sublimation; and collision-coalescence, -riming, and -aggregation. Moist air fluid dynamics is described using the compressible Navier–Stokes equation.

Our model captured cumulonimbus characteristics well, and the predicted mass-dimension and velocity-dimension relationships were comparable with existing formulas. Numerical convergence was achieved at a super-particle number concentration as low as 128/cell, which consumed 30 times more computational time than a typical two-moment bulk model.

More careful evaluation and further sophistication of the model will be necessary in the future. As discussed in Sec. 9, various elementary processes must be incorporated or refined in the model. In particular, rime splintering and collisional breakup of ice particles are important because these processes are thought to be responsible for secondary ice production. Therefore, establishing an accurate and efficient particle-based algorithm for spontaneous/collisional breakup is also crucial.

Particle-based model accuracy is more subject to cloud microphysics uncertainties than numerical errors. Therefore, quantitative understanding of elementary cloud microphysics processes is becoming increasingly important. More laboratory, observational, and theoretical studies to advance our knowledge of cloud microphysics are desired in the future. Additionally, we can go into a more microscopic description of cloud microphysics than kinetic description, i.e., to explicitly resolve droplet and ice



particle shapes and deterministically consider their collisions (e.g., Demange et al., 2017; Wang and Ji, 2000; Westbrook et al., 2004a, b; Maruyama and Fujiyoshi, 2005; Schmitt and Heymsfield, 2010; Mazloomi Moqaddam et al., 2015). Such model studies would also be useful for refining kinetic descriptions.

Our model's computational cost is at least one or two orders of magnitude larger than that of bulk models. To further  
5 accelerate calculation, the use of SGS models discussed in Sec. 9.2.9 is important. Further reduction of the computational cost can also be achieved by using the Twomey super-droplet methodology described in Grabowski et al. (2018); however, it is vital to introduce dynamic load balancing. Acceleration achieved by those improvements may not be enough to allow the use of particle-based cloud microphysics models in weather or climate models. Studies to construct a high-fidelity bulk model or other form of macroscopic cloud microphysics model must also be pursued (e.g., Noh et al., 2018).

## 10 Appendix A: List of symbols

Table A1 summarizes important variables used in this study.



**Table A1.** List of symbols

Symbol	Description
$\mathbf{a}, \mathbf{a}_i$	attributes of a particle
$a, a_i$	equatorial radius of an ice particle
$a$	coefficient of curvature term of Köhler curve
$A_i$	projected area of a particle perpendicular to flow direction
$A_i^{\text{cc}}$	area of circumcircle of $A_i$
$A_i^{\text{ce}}$	area of circumscribed ellipse of $A_i$
$A_g$	geometric cross-sectional area
$A^{\text{insol}}$	surface area of an insoluble substance
$b$	coefficient of solute term of Köhler curve
$b_1, b_2$	constant for ventilation coefficients
$c, c_i$	polar radius of an ice particle
$c_{\text{pd}}, c_{\text{pv}}, c_{\text{p}}$	isobaric specific heat of dry air, water vapor, and moist air; $c_{\text{p}} := q_{\text{d}}c_{\text{pd}} + q_{\text{v}}c_{\text{pv}}$
$c^{\text{sulf}}, c^{\text{dust}}$	initial number concentration of ammonium bisulfate aerosol particles and mineral dust particles
$c^{\text{SP}}$	initial number concentration of super-particles
$C$	electric capacitance of a spheroid
$C_{\text{SC}}$	Cunningham slip correction factor
$d^{\text{dust}}$	mineral dust particle diameter
$D_i$	particle maximum dimension
$D_{\text{v}}$	diffusivity of water vapor in air
$e, e_i$	vapor pressure and ambient vapor pressure
$e_{\text{s}}^{\text{w}}, e_{\text{s}}^{\text{i}}$	saturation vapor pressure over planar liquid water surface, over planar ice surface
$e_{\text{si}}^{\text{w,eff}}$	effective saturation vapor pressure with respect to droplet surface
$E_{\text{coal}}, E_{\text{rime}}, E_{\text{agg}}$	collection efficiencies of collision-coalescence, -riming, and -aggregation
$\bar{f}_{\text{vnt}}, f_{\text{vnt}}$	ventilation coefficients for mass growth rate, and axis growth rate



$F_i^{\text{drg}}$	drag force from moist air on a particle
$F_k^i, F_d^i, F_k^w, F_d^w$	thermodynamic terms of a particle's diffusional growth
$g$	Earth's gravity
$\mathbf{G}, \mathbf{G}_i, \mathbf{G}_{lmn}$	state of moist air, state of ambient moist air, state of moist air at grid point $(l, m, n)$
$i, j, k$	index of particles or super-particles
$i_n^{\text{fz}}, i_n^{\text{melt}}, i_n^{\text{rime}}$	indices of the $n$ -th frozen droplet, melted ice particle, and rimed droplet
$I_r(t), I_s(t)$	set of all particle indices at time $t$ , set of all super-particle indices
$I_\alpha$	degree of a solute's ionic dissociation
$k$	thermal conductivity of moist air
$K, K_{\text{coal}}, K_{\text{rime}}, K_{\text{agg}}$	collision-coalescence, -riming, and -aggregation kernels
$L_v, L_s, L_f$	latent heat of vaporization, latent heat of sublimation, and latent heat of fusion
$m, m_i$	particle mass
$m^*$	normalized ice particle mass
$m_{\text{min}}^i$	arbitrary small mass
$m^{\text{rime}}, m_i^{\text{rime}}$	ice particle rime mass
$m_\alpha^{\text{sol}}, m_{\alpha i}^{\text{sol}}$	mass of a soluble substance contained in a particle; $\alpha = 1, \dots, N^{\text{sol}}$
$m_\alpha^{\text{insol}}, m_{\alpha i}^{\text{insol}}$	mass of an insoluble substance contained in a particle; $\alpha = 1, \dots, N^{\text{insol}}$
$M_\alpha^{\text{sol}}$	molecular weight of a solute
$n(\mathbf{a}, \mathbf{x}, t)$	particle distribution function
$n^{\text{sulf}}(\log r_{\text{dry}}^{\text{sulf}}, T^{\text{fz}})$	initial distribution function of ammonium bisulfate particles
$n^{\text{mono}}, n_i^{\text{mono}}$	number of monomers of an ice particle
$n_S(T)$	ice nucleation active surface site (INAS) density
$N_r(t), N_s(t)$	total number of particles at time $t$ , total number of super-particles at time $t$
$N_r^{\text{wP}}, N_s^{\text{wP}}$	total number of particles accumulated over the whole period, total number of accumulated super-particles



$N_{mFr}$	mixed Froude number
$N_{Sc}$	Schmidt number
$N^{insol}, N^{sol}$	number of insoluble substances, number of soluble substances
$N_{Rei}^i, N_{Rei}^{clm}, N_{Rei}^w$	Reynolds number of an ice particle, of an ice particle based on the column width, and of a droplet
$N_{St}^{i/w}, N_{St}^{w/i}$	Stokes impaction parameter when a droplet collects an ice particle and when an ice particle collects a droplet
$N^{sulf}(r_{dry}^{sulf})$	accumulated number of particles smaller than $r_{dry}^{sulf}$ per unit volume of air at $t = 0$
$p$	probability density
$p^{i/w}, p^{w/i}$	$p^{i/w} := r_j^i/r_k, p^{w/i} := r_k/r_j^i$
$P$	probability
$P_{INia}$	probability that a mineral dust particle is IN inactive; $P_{INia} := P(T^{fz} \leq -38^\circ C)$
$P_{INia}^{SP}$	fraction of super-particles used for IN inactive mineral dust particles
$P, P_i$	pressure, ambient pressure
$P_0$	reference pressure; $P_0 = 1000$ hPa
$P_{jk}$	probability of collision-coalescence, -riming, and -aggregation
$q_v, q_d$	specific humidity and mass of dry air per unit mass of moist air; $q_v := \rho_v/\rho, q_d := \rho_d/\rho$
$r, r_i$	radius of the volume-equivalent sphere of liquid water in a particle
$r_i^i$	radius of the volume-equivalent sphere of an ice particle; $r_i^i := (a_i^2 c_i)^{1/3}$
$r_{dry}^{sulf}$	dry radius of the ammonium bisulfate component
$R_d, R_v, R$	gas constants of dry air, vapor, and moist air; $R := q_d R_d + q_v R_v$
$s$	power-law exponent of area-dimension relationship



$s_v, s_s, s_f$	source terms by vaporization, sublimation, and fusion
$S_i^w, S_i^i$	ambient saturation ratio over liquid water, over ice; $S_i^w := e_i/e_s^w, S_i^i := e_i/e_s^i$
$t$	time
$\Delta t, \Delta t_{adv}, \Delta t_{fz/mlt}, \Delta t_{cnd/evp}, \Delta t_{dep/sbl}, \Delta t_{coal}, \Delta t_{dyn}$	common time step, time steps for advection of particles; freezing and melting; condensation and evaporation; deposition and sublimation; collision-coalescence, -riming, and -aggregation; and fluid dynamics
$t_n^{fz}, t_n^{mlt}, t_n^{rime}$	times of the $n$ -th freezing event, melting event, and riming event
$T, T_i$	temperature, ambient temperature
$T^{fz}, T_i^{fz}$	particle freezing temperature
$T_{min}^{fz}, T_{max}^{fz}$	$T_{min}^{fz} := -36^\circ\text{C}, T_{max}^{fz} := -12^\circ\text{C}$
$T_i^{sfc}$	particle surface temperature
$U, U_i$	wind velocity, ambient wind velocity; $U = (U, V, W)$
$v, v_i$	particle velocity
$v_{imp}$	impact velocity
$v_i^\infty$	particle terminal velocity
$V, V_i$	ice particle apparent volume
$V_{max}$	largest possible volume
$\Delta V$	well-mixed volume
$\mathbf{x}, \mathbf{x}_i$	particle position
$\Delta x, \Delta y, \Delta z$	grid size
$X$	$:= N_{Sc}^{1/3} (N_{Rei}^i)^{1/2}$
$Y, Y^\perp$	$Y := -r_k v_{imp} / T_j^{sfc}, Y^\perp := \min(Y, 3.5)$
$\hat{z}$	unit vector in the $z$ axis direction
$\alpha, \beta$	index of aerosol substances
$\beta$	power-law exponent of mass-dimension relationship
$\gamma$	constant for ventilation coefficients, coefficient of the artificial hyperdiffusion term



$\Gamma(T), \Gamma^*$	inherent growth ratio, effective inherent growth ratio; $\Gamma^* := \Gamma f_{vnt}$
$\delta^d(\boldsymbol{x})$	$d$ -dimensional Dirac's delta function
$\theta$	potential temperature of moist air; $\theta := T/\Pi$
$\kappa$	power exponent relating porosity to projected area
$\mu$	dynamic viscosity of moist air
$\xi_i$	super-particle multiplicity
$\Pi$	Exner function of moist air; $\Pi := (P/P_0)^{R/c_p}$
$\rho, \rho_i$	density of moist air, density of ambient moist air; $\rho := \rho_d + \rho_v$
$\rho_d$	density of dry air
$\rho_{dep}, \rho_{rime}, \rho_{sbl}$	deposition, rime, and sublimation densities
$\rho_v, \rho_{vi}$	vapor density, ambient vapor density
$\rho^i, \rho_i^i$	ice particle apparent density
$\rho_{crt}^i$	limiting value of the apparent density
$\bar{\rho}_{jk}^i$	volume weighted average density
$\rho_{jk}^{i,min}, \rho_{jk}^{i,max}$	minimum and maximum possible apparent density
$\rho_{true}^i$	ice crystal true density
$\rho_{vi}^{sfc}$	vapor density at a particle surface
$\rho^w$	density of liquid water
$\phi, \phi_i$	ice particle aspect ratio; $\phi := c/a$
$\partial \cdot / \partial t _{cm}$	coupling term from cloud microphysics to fluid dynamics of moist air
'	prime denotes a resultant particle

## Appendix B: List of abbreviations

Table B1 summarizes important abbreviations that are used in this study.



**Table B1.** List of abbreviations

Abbreviations	Full form
A72	Auer (1972)
ARM	atmospheric radiation measurement
BG74	Beard and Grover (1974)
CCN	cloud condensation nuclei
CFL	Courant-Friedrichs-Lewy
CL94	Chen and Lamb (1994a)
CRYSTAL-FACE	Cirrus Regional Study of Tropical Anvils and Cirrus Layers-Florida Area Cirrus Ex- periment
EM17	Erfani and Mitchell (2017)
H02	Heymsfield et al. (2002)
H72	Heymsfield (1972)
HK87	Heymsfield and Kajikawa (1987)
HP85	Heymsfield and Pflaum (1985)
IN	ice nucleation
INAS	ice nucleation active site
K89	Kajikawa (1989)
KH83	Knight and Heymsfield (1983)
LH74	Locatelli and Hobbs (1974)
M90	Mitchell et al. (1990)
M96	Mitchell (1996)
SC85	Starr and Cox (1985)
SDM	super-droplet method
SGS	sub-grid scale
W08	Westbrook et al. (2008)

*Code and data availability.* The source code of SCALE-SDM 0.2.5-2.2.0/2.2.1 is available from <https://doi.org/10.5281/zenodo.3483650>. All the data used for this study can be reproduced by following the instructions included in the above repository. The data are also deposited  
5 in local storage at the University of Hyogo in Kobe, Japan, and are available from the corresponding author upon request.

*Supplement.* The supplement related to this article is available online at: <https://doi.org/10.5281/zenodo.3478207>.



*Author contributions.* All the authors designed the model and numerical experiments. SS developed the model code and performed the simulations. SS prepared the manuscript with contributions from all co-authors.

*Competing interests.* The authors declare that they have no conflicts of interest.

*Acknowledgements.* S. Shima is grateful to Wojciech W. Grabowski, Sylwester Arabas, Dennis Niedermeier, Miklós Szakáll, Will H. Cantrell, Yutaka Tobo, and Hugh Morrison for informative discussions. This research partly used the computational resources of the K computer provided by the RIKEN Center for Computational Science (R-CCS) through the HPCI System Research Project (Project ID: hp150153) and the Computing Resources for Enhancement (Project ID: ra001010), and FX10 provided by Kyushu University through the HPCI System Research Project (Project ID: hp140094, hp160132). This work was supported by JSPS KAKENHI Grant Number 26286089; MEXT KAKENHI Grant Number 18H04448; the joint research program of the Institute for Space-Earth Environmental Research, Nagoya University; the Center for Cooperative Work on Computational Science, University of Hyogo; and the Department of HPC Support, Research Organization for Information Science & Technology (RIST) under the Optimization Support Program of the HPCI system. The authors would like to thank Enago ([www.enago.jp](http://www.enago.jp)) for the English language review.



## References

- Abade, G. C., Grabowski, W. W., and Pawlowska, H.: Broadening of cloud droplet spectra through eddy hopping: Turbulent entraining parcel simulations, *Journal of the Atmospheric Sciences*, 75, 3365–3379, <https://doi.org/10.1175/JAS-D-18-0078.1>, 2018.
- Andrejczuk, M., Reisner, J. M., Henson, B., Dubey, M. K., and Jeffery, C. A.: The potential impacts of pollution on a non-drizzling stratus deck: Does aerosol number matter more than type?, *Journal of Geophysical Research Atmospheres*, 113, <https://doi.org/10.1029/2007JD009445>, 2008.
- Andrejczuk, M., Grabowski, W. W., Reisner, J., and Gadian, A.: Cloud-aerosol interactions for boundary layer stratocumulus in the Lagrangian Cloud Model, *Journal of Geophysical Research Atmospheres*, 115, <https://doi.org/10.1029/2010JD014248>, 2010.
- Arabas, S. and Shima, S.-i.: Large-eddy simulations of trade wind cumuli using particle-based microphysics with monte Carlo coalescence, *Journal of the Atmospheric Sciences*, 70, 2768–2777, <https://doi.org/10.1175/JAS-D-12-0295.1>, 2013.
- Arabas, S. and Shima, S.-i.: On the CCN (de)activation nonlinearities, *Nonlinear Processes in Geophysics*, 24, 535–542, <https://doi.org/10.5194/npg-24-535-2017>, 2017.
- Auer, A. H.: Distribution of Graupel and Hail With Size, *Monthly Weather Review*, 100, 325–328, <https://doi.org/10.1175/1520-0493-100-05-0325>, 1972.
- 15 Bailey, M. and Hallett, J.: Growth rates and habits of ice crystals between -20° and -70°C, *Journal of the Atmospheric Sciences*, 61, 514–544, [https://doi.org/10.1175/1520-0469\(2004\)061<0514:GRAHOI>2.0.CO;2](https://doi.org/10.1175/1520-0469(2004)061<0514:GRAHOI>2.0.CO;2), 2004.
- Baran, A. J.: From the single-scattering properties of ice crystals to climate prediction: A way forward, <https://doi.org/10.1016/j.atmosres.2012.04.010>, 2012.
- Beard, K. V.: TERMINAL VELOCITY AND SHAPE OF CLOUD AND PRECIPITATION DROPS ALOFT., *Journal of the Atmospheric Sciences*, 33, 851–864, [https://doi.org/10.1175/1520-0469\(1976\)033<0851:TVASOC>2.0.CO;2](https://doi.org/10.1175/1520-0469(1976)033<0851:TVASOC>2.0.CO;2), 1976.
- 20 Beard, K. V. and Grover, S. N.: Numerical Collision Efficiencies for Small Raindrops Colliding with Micron Size Particles, *Journal of the Atmospheric Sciences*, 31, 543–550, [https://doi.org/10.1175/1520-0469\(1974\)031<0543:ncefsr>2.0.co;2](https://doi.org/10.1175/1520-0469(1974)031<0543:ncefsr>2.0.co;2), 1974.
- Böhm, H. P.: A general equation for the terminal fall speed of solid hydrometeors, *Journal of the Atmospheric Sciences*, 46, 2419–2427, [https://doi.org/10.1175/1520-0469\(1989\)046<2419:AGEFTT>2.0.CO;2](https://doi.org/10.1175/1520-0469(1989)046<2419:AGEFTT>2.0.CO;2), 1989.
- 25 Böhm, J. P.: A general hydrodynamic theory for mixed-phase microphysics. Part III: Riming and aggregation, *Atmospheric Research*, 28, 103–123, [https://doi.org/10.1016/0169-8095\(92\)90023-4](https://doi.org/10.1016/0169-8095(92)90023-4), 1992a.
- Böhm, J. P.: A general hydrodynamic theory for mixed-phase microphysics. Part II: collision kernels for coalescence, *Atmospheric Research*, 27, 275–290, [https://doi.org/10.1016/0169-8095\(92\)90036-A](https://doi.org/10.1016/0169-8095(92)90036-A), 1992b.
- Böhm, J. P.: A general hydrodynamic theory for mixed-phase microphysics. Part I: drag and fall speed of hydrometeors, *Atmospheric Research*, 27, 253–274, [https://doi.org/10.1016/0169-8095\(92\)90035-9](https://doi.org/10.1016/0169-8095(92)90035-9), 1992c.
- 30 Böhm, J. P.: Theoretical collision efficiencies for riming and aerosol impaction, *Atmospheric Research*, 32, 171–187, [https://doi.org/10.1016/0169-8095\(94\)90058-2](https://doi.org/10.1016/0169-8095(94)90058-2), 1994.
- Böhm, J. P.: Revision and clarification of 'a general hydrodynamic theory for mixed-phase microphysics', *Atmospheric Research*, 52, 167–176, [https://doi.org/10.1016/S0169-8095\(99\)00033-2](https://doi.org/10.1016/S0169-8095(99)00033-2), 1999.
- 35 Bott, A.: A flux method for the numerical solution of the stochastic collection equation, *Journal of the Atmospheric Sciences*, 55, 2284–2293, [https://doi.org/10.1175/1520-0469\(1998\)055<2284:AFMFTN>2.0.CO;2](https://doi.org/10.1175/1520-0469(1998)055<2284:AFMFTN>2.0.CO;2), 1998.



- Brdar, S. and Seifert, A.: McSnow: A Monte-Carlo Particle Model for Riming and Aggregation of Ice Particles in a Multidimensional Microphysical Phase Space, *Journal of Advances in Modeling Earth Systems*, 10, 187–206, <https://doi.org/10.1002/2017MS001167>, 2018.
- Brown, A. R., Derbyshire, S. H., and Mason, P. J.: Large-eddy simulation of stable atmospheric boundary layers with a revised stochastic subgrid model, *Quarterly Journal of the Royal Meteorological Society*, 120, 1485–1512, <https://doi.org/10.1002/qj.49712052004>, 1994.
- 5 Brown, P. R. A. and Francis, P. N.: Improved Measurements of the Ice Water Content in Cirrus Using a Total-Water Probe, *Journal of Atmospheric and Oceanic Technology*, 12, 410–414, [https://doi.org/10.1175/1520-0426\(1995\)012<0410:imotiw>2.0.co;2](https://doi.org/10.1175/1520-0426(1995)012<0410:imotiw>2.0.co;2), 1995.
- Chen, J.-P. and Lamb, D.: The Theoretical Basis for the Parameterization of Ice Crystal Habits: Growth by Vapor Deposition, *Journal of the Atmospheric Sciences*, 51, 1206–1222, [https://doi.org/10.1175/1520-0469\(1994\)051<1206:TTBFTP>2.0.CO;2](https://doi.org/10.1175/1520-0469(1994)051<1206:TTBFTP>2.0.CO;2), [http://journals.ametsoc.org/doi/abs/10.1175/1520-0469\(1994\)051<1206:TTBFTP>2.0.CO;2](http://journals.ametsoc.org/doi/abs/10.1175/1520-0469(1994)051<1206:TTBFTP>2.0.CO;2), 1994a.
- 10 Chen, J.-P. and Lamb, D.: Simulation of Cloud Microphysical and Chemical Processes Using a Multicomponent Framework. Part I: Description of the Microphysical Model, *Journal of the Atmospheric Sciences*, 51, 2613–2630, [https://doi.org/10.1175/1520-0469\(1994\)051<2613:socmac>2.0.co;2](https://doi.org/10.1175/1520-0469(1994)051<2613:socmac>2.0.co;2), 1994b.
- Chen, S., Yau, M. K., and Bartello, P.: Turbulence effects of collision efficiency and broadening of droplet size distribution in cumulus clouds, *Journal of the Atmospheric Sciences*, 75, 203–217, <https://doi.org/10.1175/JAS-D-17-0123.1>, 2018.
- 15 Connolly, P. J., Möhler, O., Field, P. R., Saathoff, H., Burgess, R., Choulaton, T., and Gallagher, M.: Studies of heterogeneous freezing by three different desert dust samples, *Atmospheric Chemistry and Physics*, 9, 2805–2824, <https://doi.org/10.5194/acp-9-2805-2009>, 2009.
- Connolly, P. J., Emersic, C., and Field, P. R.: A laboratory investigation into the aggregation efficiency of small ice crystals, *Atmospheric Chemistry and Physics*, 12, 2055–2076, <https://doi.org/10.5194/acp-12-2055-2012>, 2012.
- Cooper, W. A.: Effects of variable droplet growth histories on droplet size distributions. Part I: theory, *Journal of the Atmospheric Sciences*, 20 46, 1301–1311, [https://doi.org/10.1175/1520-0469\(1989\)046<1301:EOVDGH>2.0.CO;2](https://doi.org/10.1175/1520-0469(1989)046<1301:EOVDGH>2.0.CO;2), 1989.
- Cui, Z., Carslaw, K. S., Yin, Y., and Davies, S.: A numerical study of aerosol effects on the dynamics and microphysics of a deep convective cloud in a continental environment, *Journal of Geophysical Research Atmospheres*, 111, <https://doi.org/10.1029/2005JD005981>, 2006.
- Davis, M. H.: Collisions of Small Cloud Droplets: Gas Kinetic Effects, *Journal of the Atmospheric Sciences*, 29, 911–915, [https://doi.org/10.1175/1520-0469\(1972\)029<0911:coscdg>2.0.co;2](https://doi.org/10.1175/1520-0469(1972)029<0911:coscdg>2.0.co;2), 1972.
- 25 De Boer, G., Morrison, H., Shupe, M. D., and Hildner, R.: Evidence of liquid dependent ice nucleation in high-latitude stratiform clouds from surface remote sensors, *Geophysical Research Letters*, 38, <https://doi.org/10.1029/2010GL046016>, 2011.
- Demange, G., Zapolsky, H., Patte, R., and Brunel, M.: A phase field model for snow crystal growth in three dimensions, *npj Computational Materials*, 3, <https://doi.org/10.1038/s41524-017-0015-1>, 2017.
- DeVile, R. E., Riemer, N., and West, M.: Weighted Flow Algorithms (WFA) for stochastic particle coagulation, *Journal of Computational Physics*, 230, 8427–8451, <https://doi.org/10.1016/j.jcp.2011.07.027>, 2011.
- 30 Durant, A. J. and Shaw, R. A.: Evaporation freezing by contact nucleation inside-out, *Geophysical Research Letters*, 32, 1–4, <https://doi.org/10.1029/2005GL024175>, 2005.
- Dziekan, P. and Pawlowska, H.: Stochastic coalescence in Lagrangian cloud microphysics, *Atmospheric Chemistry and Physics*, 17, 13 509–13 520, <https://doi.org/10.5194/acp-17-13509-2017>, 2017.
- 35 Dziekan, P., Waruszewski, M., and Pawlowska, H.: University of Warsaw Lagrangian Cloud Model (UWLCM) 1.0: a modern Large-Eddy Simulation tool for warm cloud modeling with Lagrangian microphysics, *Geoscientific Model Development Discussions*, pp. 1–26, <https://doi.org/10.5194/gmd-2018-281>, <https://www.geosci-model-dev-discuss.net/gmd-2018-281/>, 2019.



- Erfani, E. and Mitchell, D. L.: Growth of ice particle mass and projected area during riming, *Atmospheric Chemistry and Physics*, 17, 1241–1257, <https://doi.org/10.5194/acp-17-1241-2017>, 2017.
- Field, P. R., Heymsfield, A. J., and Bansemer, A.: A test of ice self-collection kernels using aircraft data, *Journal of the Atmospheric Sciences*, 63, 651–666, <https://doi.org/10.1175/JAS3653.1>, 2006.
- 5 Field, P. R., Lawson, R. P., Brown, P. R. A., Lloyd, G., Westbrook, C., Moisseev, D., Miltenberger, A., Nenes, A., Blyth, A., Choulaton, T., Connolly, P., Buehl, J., Crosier, J., Cui, Z., Dearden, C., DeMott, P., Flossmann, A., Heymsfield, A., Huang, Y., Kalesse, H., Kanji, Z. A., Korolev, A., Kirchgaessner, A., Lasher-Trapp, S., Leisner, T., McFarquhar, G., Phillips, V., Stith, J., and Sullivan, S.: Secondary Ice Production: Current State of the Science and Recommendations for the Future, *Meteorological Monographs*, 58, 7.1–7.20, <https://doi.org/10.1175/AMSMONOGRAPHIS-D-16-0014.1>, <https://doi.org/10.1175/AMSMONOGRAPHIS-D-16-0014.1>, 2017.
- 10 Findeisen, W. and Findeisen, E.: Investigations on the ice splinter formation on rime layers (A contribution to the origin of storm electricity and to the microstructure of cumulonimbi), *Meteor. Z.*, 60, 145–154, 1943.
- Fletcher, N. H.: Active Sites and Ice Crystal Nucleation, *Journal of the Atmospheric Sciences*, 26, 1266–1271, [https://doi.org/10.1175/1520-0469\(1969\)026<1266:asaicn>2.0.co;2](https://doi.org/10.1175/1520-0469(1969)026<1266:asaicn>2.0.co;2), 1969.
- Gillespie, D. T.: The Stochastic Coalescence Model for Cloud Droplet Growth, *Journal of the Atmospheric Sciences*, 29, 1496–1510, [https://doi.org/10.1175/1520-0469\(1972\)029<1496:tscmfc>2.0.co;2](https://doi.org/10.1175/1520-0469(1972)029<1496:tscmfc>2.0.co;2), 1972.
- 15 Grabowski, W. W. and Abade, G. C.: Broadening of Cloud Droplet Spectra through Eddy Hopping: Turbulent Adiabatic Parcel Simulations, *Journal of the Atmospheric Sciences*, 74, 1485–1493, <https://doi.org/10.1175/JAS-D-17-0043.1>, <http://journals.ametsoc.org/doi/10.1175/JAS-D-17-0043.1>, 2017.
- Grabowski, W. W., Dziekan, P., and Pawlowska, H.: Lagrangian condensation microphysics with Twomey CCN activation, *Geoscientific Model Development*, 11, 103–120, <https://doi.org/10.5194/gmd-11-103-2018>, <https://www.geosci-model-dev.net/11/103/2018/>, 2018.
- Grabowski, W. W., Morrison, H., Shima, S.-i., Abade, G. C., Dziekan, P., and Pawlowska, H.: Modeling of cloud microphysics: Can we do better?, *Bulletin of the American Meteorological Society*, 100, 655–672, <https://doi.org/10.1175/BAMS-D-18-0005.1>, 2019.
- Hall, W. D.: A Detailed Microphysical Model Within a Two-Dimensional Dynamic Framework: Model Description and Preliminary Results, *Journal of the Atmospheric Sciences*, 37, 2486–2507, [https://doi.org/10.1175/1520-0469\(1980\)037<2486:admmwa>2.0.co;2](https://doi.org/10.1175/1520-0469(1980)037<2486:admmwa>2.0.co;2), 1980.
- 25 Hall, W. D. and Pruppacher, H. R.: SURVIVAL OF ICE PARTICLES FALLING FROM CIRRUS CLOUDS IN SUBSATURATED AIR., *Journal of the Atmospheric Sciences*, 33, 1995–2006, [https://doi.org/10.1175/1520-0469\(1976\)033<1995:TSOIPF>2.0.CO;2](https://doi.org/10.1175/1520-0469(1976)033<1995:TSOIPF>2.0.CO;2), 1976.
- Hallett, J. and Mason, B. J.: The influence of temperature and supersaturation on the habit of ice crystals grown from the vapour, *Proceedings of the Royal Society of London. Series A. Mathematical and Physical Sciences*, 247, 440–453, <https://doi.org/10.1098/rspa.1958.0199>, 1958.
- 30 Hallett, J. and Mossop, S. C.: Production of secondary ice particles during the riming process, *Nature*, 249, 26–28, <https://doi.org/10.1038/249026a0>, 1974.
- Harrington, J. Y., Moyle, A., Hanson, L. E., and Morrison, H.: On calculating deposition coefficients and aspect-ratio evolution in approximate models of ice crystal vapor growth, *Journal of the Atmospheric Sciences*, 76, 1609–1625, <https://doi.org/10.1175/JAS-D-18-0319.1>, 2019.
- 35 Hashino, T. and Tripoli, G. J.: The Spectral Ice Habit Prediction System (SHIPS). Part I: Model description and simulation of the vapor deposition process, *Journal of the Atmospheric Sciences*, 64, 2210–2237, <https://doi.org/10.1175/JAS3963.1>, 2007.
- Hashino, T. and Tripoli, G. J.: The spectral ice habit prediction system (SHIPS). Part II: Simulation of nucleation and depositional growth of polycrystals, *Journal of the Atmospheric Sciences*, 65, 3071–3094, <https://doi.org/10.1175/2008JAS2615.1>, 2008.



- Hashino, T. and Tripoli, G. J.: The Spectral Ice Habit Prediction System (SHIPS). Part III: Description of the ice particle model and the habit-dependent aggregation model, *Journal of the Atmospheric Sciences*, 68, 1125–1141, <https://doi.org/10.1175/2011JAS3666.1>, 2011a.
- Hashino, T. and Tripoli, G. J.: The Spectral Ice Habit Prediction System (SHIPS). Part IV: Box model simulations of the habit-dependent aggregation process, *Journal of the Atmospheric Sciences*, 68, 1142–1161, <https://doi.org/10.1175/2011JAS3667.1>, 2011b.
- 5 Heymsfield, A.: Ice Crystal Terminal Velocities, *Journal of the Atmospheric Sciences*, 29, 1348–1357, [https://doi.org/10.1175/1520-0469\(1972\)029<1348:ictv>2.0.co;2](https://doi.org/10.1175/1520-0469(1972)029<1348:ictv>2.0.co;2), 1972.
- Heymsfield, A. J.: The Characteristics of Graupel Particles in Northeastern Colorado Cumulus Congestus Clouds, *Journal of the Atmospheric Sciences*, 35, 284–295, [https://doi.org/10.1175/1520-0469\(1978\)035<0284:TCOGPI>2.0.CO;2](https://doi.org/10.1175/1520-0469(1978)035<0284:TCOGPI>2.0.CO;2), [https://journals.ametsoc.org/doi/abs/10.1175/1520-0469\(1978\)035<0284:TCOGPI>2.0.CO;2](https://journals.ametsoc.org/doi/abs/10.1175/1520-0469(1978)035<0284:TCOGPI>2.0.CO;2), 1978.
- 10 Heymsfield, A. J.: A comparative study of the rates of development of potential graupel and hail embryos in High Plains storms., *Journal of the Atmospheric Sciences*, 39, 2867–2897, [https://doi.org/10.1175/1520-0469\(1982\)039<2867:ACSOTR>2.0.CO;2](https://doi.org/10.1175/1520-0469(1982)039<2867:ACSOTR>2.0.CO;2), 1982.
- Heymsfield, A. J. and Kajikawa, M.: IMPROVED APPROACH TO CALCULATING TERMINAL VELOCITIES OF PLATE-LIKE CRYSTALS AND GRAUPEL., *Journal of the Atmospheric Sciences*, 44, 1088–1099, [https://doi.org/10.1175/1520-0469\(1987\)044<1088:AIATCT>2.0.CO;2](https://doi.org/10.1175/1520-0469(1987)044<1088:AIATCT>2.0.CO;2), 1987.
- 15 Heymsfield, A. J. and Pflaum, J. C.: A quantitative assessment of the accuracy of techniques for calculating graupel growth., *Journal of the Atmospheric Sciences*, 42, 2264–2274, [https://doi.org/10.1175/1520-0469\(1985\)042<2264:AQAOTA>2.0.CO;2](https://doi.org/10.1175/1520-0469(1985)042<2264:AQAOTA>2.0.CO;2), 1985.
- Heymsfield, A. J., Lewis, S., Bansemer, A., Iaquinta, J., Miloshevich, L. M., Kajikawa, M., Twohy, C., and Poellot, M. R.: A general approach for deriving the properties of cirrus and stratiform ice cloud particles, *Journal of the Atmospheric Sciences*, 59, 3–29, [https://doi.org/10.1175/1520-0469\(2002\)059<0003:AGAFDT>2.0.CO;2](https://doi.org/10.1175/1520-0469(2002)059<0003:AGAFDT>2.0.CO;2), 2002.
- 20 Heymsfield, A. J., Schmitt, C., Bansemer, A., and Twohy, C. H.: Improved representation of ice particle masses based on observations in natural clouds, *Journal of the Atmospheric Sciences*, 67, 3303–3318, <https://doi.org/10.1175/2010JAS3507.1>, 2010.
- Higuchi, K.: ON THE COALESCENCE BETWEEN PLANE SNOW CRYSTALS, *Journal of Meteorology*, 17, 239–243, [https://doi.org/10.1175/1520-0469\(1960\)017<0239:otcbps>2.0.co;2](https://doi.org/10.1175/1520-0469(1960)017<0239:otcbps>2.0.co;2), 1960.
- Hoffmann, F.: On the limits of Köhler activation theory: How do collision and coalescence affect the activation of aerosols?, *Atmospheric Chemistry and Physics*, 17, 8343–8356, <https://doi.org/10.5194/acp-17-8343-2017>, 2017.
- 25 Hoffmann, F., Yamaguchi, T., and Feingold, G.: Inhomogeneous mixing in lagrangian cloud models: Effects on the production of precipitation embryos, *Journal of the Atmospheric Sciences*, 76, 113–133, <https://doi.org/10.1175/JAS-D-18-0087.1>, 2019.
- Hoose, C. and Möhler, O.: Heterogeneous ice nucleation on atmospheric aerosols: A review of results from laboratory experiments, <https://doi.org/10.5194/acp-12-9817-2012>, 2012.
- 30 Hubbard, J. B. and Douglas, J. F.: Hydrodynamic friction of arbitrarily shaped Brownian particles, *Physical Review E*, 47, <https://doi.org/10.1103/PhysRevE.47.R2983>, 1993.
- Jaruga, A. and Pawlowska, H.: Libcloudph++ 2.0: Aqueous-phase chemistry extension of the particle-based cloud microphysics scheme, *Geoscientific Model Development*, 11, 3623–3645, <https://doi.org/10.5194/gmd-11-3623-2018>, 2018.
- Jensen, A. A. and Harrington, J. Y.: Modeling ice crystal aspect ratio evolution during riming: A single-particle growth model, *Journal of the Atmospheric Sciences*, 72, 2569–2590, <https://doi.org/10.1175/JAS-D-14-0297.1>, 2015.
- 35 Jensen, E. and Pfister, L.: Transport and freeze-drying in the tropical tropopause layer, *Journal of Geophysical Research: Atmospheres*, 109, <https://doi.org/10.1029/2003JD004022>, <https://agupubs.onlinelibrary.wiley.com/doi/abs/10.1029/2003JD004022>, 2004.



- Jiang, Z., Oue, M., Verlinde, J., Clothiaux, E. E., Aydin, K., Botta, G., and Lu, Y.: What can we conclude about the real aspect ratios of ice particle aggregates from two-dimensional images?, *Journal of Applied Meteorology and Climatology*, 56, 725–734, <https://doi.org/10.1175/JAMC-D-16-0248.1>, 2017.
- Jonas, P. R.: The collision efficiency of small drops, *Quarterly Journal of the Royal Meteorological Society*, 98, 681–683, <https://doi.org/10.1002/qj.49709841717>, <http://doi.wiley.com/10.1002/qj.49709841717>, 1972.
- 5 Kajikawa, M.: Observation of the Falling Motion of Early Snowflakes., *Journal of the Meteorological Society of Japan. Ser. II*, 67, 731–738, [https://doi.org/10.2151/jmsj1965.67.5\\_731](https://doi.org/10.2151/jmsj1965.67.5_731), 1989.
- Kajikawa, M.: Characteristics of the aggregation of needle snow crystals, *Journal of the Japanese Society of Snow and Ice*, 57, 349–355, 1995.
- 10 Kajikawa, M. and Heymsfield, A. J.: Aggregation of ice crystals in cirrus, *Journal of the Atmospheric Sciences*, 46, 3108–3121, [https://doi.org/10.1175/1520-0469\(1989\)046<3108:AOICIC>2.0.CO;2](https://doi.org/10.1175/1520-0469(1989)046<3108:AOICIC>2.0.CO;2), 1989.
- Kajikawa, M., Narita, E., Ichinoseki, K., Kudo, T., and Sasaki, R.: Observation of composition factors of snowflakes, *Journal of the Japanese Society of Snow and Ice*, 64, 69–76, 2002.
- Kamra, A. K., Bhalwankar, R. V., and Sathe, A. B.: Spontaneous breakup of charged and uncharged water drops freely suspended in a wind tunnel, *Journal of Geophysical Research*, 96, 17 159, <https://doi.org/10.1029/91jd01475>, 1991.
- 15 Kanji, Z. A., Ladino, L. A., Wex, H., Boose, Y., Burkert-Kohn, M., Cziczko, D. J., and Krämer, M.: Overview of Ice Nucleating Particles, *Meteorological Monographs*, 58, 1.1–1.33, <https://doi.org/10.1175/amsmonographs-d-16-0006.1>, 2017.
- Khain, A., Pokrovsky, A., Pinsky, M., Seifert, A., and Phillips, V.: Simulation of effects of atmospheric aerosols on deep turbulent convective clouds using a spectral microphysics mixed-phase cumulus cloud model. Part I: Model description and possible applications, *Journal of the Atmospheric Sciences*, 61, 2963–2982, <https://doi.org/10.1175/JAS-3350.1>, 2004.
- 20 Khain, A. P. and Pinsky, M.: *Physical Processes in Clouds and Cloud Modeling*, Cambridge University Press, <https://doi.org/10.1017/9781139049481>, 2018.
- Khain, A. P., Beheng, K. D., Heymsfield, A., Korolev, A., Krichak, S. O., Levin, Z., Pinsky, M., Phillips, V., Prabhakaran, T., Teller, A., Van Den Heever, S. C., and Yano, J. I.: Representation of microphysical processes in cloud-resolving models: Spectral (bin) microphysics versus bulk parameterization, <https://doi.org/10.1002/2014RG000468>, 2015.
- 25 Khvorostyanov, V. I. and Curry, J. A.: The theory of ice nucleation by heterogeneous freezing of deliquescent mixed CCN. Part I: Critical radius, energy and nucleation rate, *Journal of the Atmospheric Sciences*, 61, 2676–2691, <https://doi.org/10.1175/JAS3266.1>, 2004.
- Khvorostyanov, V. I. and Curry, J. A.: The theory of ice nucleation by heterogeneous freezing of deliquescent mixed CCN. Part II: Parcel model simulation, *Journal of the Atmospheric Sciences*, 62, 261–285, <https://doi.org/10.1175/JAS-3367.1>, 2005.
- 30 Khvorostyanov, V. I. and Curry, J. A.: *Thermodynamics, kinetics, and microphysics of clouds*, Cambridge University Press, <https://doi.org/10.1017/CBO9781139060004>, 2014.
- Kikuchi, K., Kameda, T., Higuchi, K., and Yamashita, A.: A global classification of snow crystals, ice crystals, and solid precipitation based on observations from middle latitudes to polar regions, *Atmospheric Research*, 132-133, 460–472, <https://doi.org/10.1016/j.atmosres.2013.06.006>, 2013.
- 35 Knight, N. C. and Heymsfield, A. J.: Measurement and interpretation of hailstone density and terminal velocity., *Journal of the Atmospheric Sciences*, 40, 1510–1516, [https://doi.org/10.1175/1520-0469\(1983\)040<1510:MAIOHD>2.0.CO;2](https://doi.org/10.1175/1520-0469(1983)040<1510:MAIOHD>2.0.CO;2), 1983.
- Kobayashi, T.: The growth of snow crystals at low supersaturations, *Philosophical Magazine*, 6, 1363–1370, <https://doi.org/10.1080/14786436108241231>, 1961.



- Kogan, Y. L.: The simulation of a convective cloud in a 3-D model with explicit microphysics. Part I: model description and sensitivity experiments, *Journal of the Atmospheric Sciences*, 48, 1160–1189, [https://doi.org/10.1175/1520-0469\(1991\)048<1160:TSOACC>2.0.CO;2](https://doi.org/10.1175/1520-0469(1991)048<1160:TSOACC>2.0.CO;2), 1991.
- Köhler, H.: The nucleus in and the growth of hygroscopic droplets, *Transactions of the Faraday Society*, 32, 1152–1161, <https://doi.org/10.1039/TF9363201152>, 1936.
- Koop, T., Luo, B., Tsias, A., and Peter, T.: Water activity as the determinant for homogeneous ice nucleation in aqueous solutions, *Nature*, 406, 611–614, <https://doi.org/10.1038/35020537>, 2000.
- Korolev, A. and Isaac, G.: Roundness and aspect ratio of particles in ice clouds, *Journal of the Atmospheric Sciences*, 60, 1795–1808, [https://doi.org/10.1175/1520-0469\(2003\)060<1795:RAAROP>2.0.CO;2](https://doi.org/10.1175/1520-0469(2003)060<1795:RAAROP>2.0.CO;2), 2003.
- 10 Korolev, A., McFarquhar, G., Field, P. R., Franklin, C., Lawson, P., Wang, Z., Williams, E., Abel, S. J., Axisa, D., Borrmann, S., Crosier, J., Fugal, J., Krämer, M., Lohmann, U., Schlenzcek, O., Schnaiter, M., and Wendisch, M.: Mixed-Phase Clouds: Progress and Challenges, *Meteorological Monographs*, 58, 5.1–5.50, <https://doi.org/10.1175/amsmonographs-d-17-0001.1>, 2017.
- Kumai, M.: Formation of Ice Crystals and Dissipation of Supercooled Fog by Artificial Nucleation, and Variations of Crystal Habit at Early Growth Stages, *Journal of Applied Meteorology*, 21, 579–587, [https://doi.org/10.1175/1520-0450\(1982\)021<0579:FOICAD>2.0.CO;2](https://doi.org/10.1175/1520-0450(1982)021<0579:FOICAD>2.0.CO;2), [http://journals.ametsoc.org/doi/abs/10.1175/1520-0450\(1982\)021<0579:FOICAD>2.0.CO;2](http://journals.ametsoc.org/doi/abs/10.1175/1520-0450(1982)021<0579:FOICAD>2.0.CO;2), 1982.
- 15 Lawson, R. P., Pilson, B., Baker, B., Mo, Q., Jensen, E., Pfister, L., and Bui, P.: Aircraft measurements of microphysical properties of subvisible cirrus in the tropical tropopause layer, *Atmospheric Chemistry and Physics*, 8, 1609–1620, <https://doi.org/10.5194/acp-8-1609-2008>, 2008.
- Levine, J.: Statistical explanation of spontaneous freezing of water droplets, NACA Tech. Notes, p. no. 2234, 1950.
- 20 Lew, J. K. and Pruppacher, H. R.: A Theoretical Determination of the Capture Efficiency of Small Columnar Ice Crystals by Large Cloud Drops, *Journal of the Atmospheric Sciences*, 40, 139–145, [https://doi.org/10.1175/1520-0469\(1983\)040<0139:ATDOTC>2.0.CO;2](https://doi.org/10.1175/1520-0469(1983)040<0139:ATDOTC>2.0.CO;2), [http://journals.ametsoc.org/doi/abs/10.1175/1520-0469\(1983\)040<0139:ATDOTC>2.0.CO;2](http://journals.ametsoc.org/doi/abs/10.1175/1520-0469(1983)040<0139:ATDOTC>2.0.CO;2), 1983.
- Lew, J. K., Kingsmill, D. E., and Montague, D. C.: A Theoretical Study of the Collision Efficiency of Small Planar Ice Crystals Colliding with Large Supercooled Water Drops, *Journal of the Atmospheric Sciences*, 42, 857–862, [https://doi.org/10.1175/1520-0469\(1985\)042<0857:atsotc>2.0.co;2](https://doi.org/10.1175/1520-0469(1985)042<0857:atsotc>2.0.co;2), 1985.
- 25 Lilly, D. K.: On the numerical simulation of buoyant convection, *Tellus*, 14, 148–172, <https://doi.org/10.1111/j.2153-3490.1962.tb00128.x>, <http://tellusa.net/index.php/tellusa/article/view/9537>, 1962.
- Locatelli, J. D. and Hobbs, P. V.: Fall speeds and masses of solid precipitation particles, *Journal of Geophysical Research*, 79, 2185–2197, <https://doi.org/10.1029/jc079i015p02185>, 1974.
- 30 Low, R. D. H.: A Generalized Equation for the Solution Effect in Droplet Growth, *Journal of the Atmospheric Sciences*, 26, 608–611, [https://doi.org/10.1175/1520-0469\(1969\)026<0608:agefts>2.0.co;2](https://doi.org/10.1175/1520-0469(1969)026<0608:agefts>2.0.co;2), 1969.
- Magono, C. and Lee, C. W.: Meteorological Classification of Natural Snow Crystals, *Journal of the Faculty of Science, Hokkaido University. Series 7, Geophysics, II*, 321–335, 1966.
- Magono, C. and Nakamura, T.: Aerodynamic Studies of Falling Snowflakes, *Journal of the Meteorological Society of Japan. Ser. II*, 43, 139–147, [https://doi.org/10.2151/jmsj1965.43.3\\_139](https://doi.org/10.2151/jmsj1965.43.3_139), 1965.
- 35 Marcolli, C.: Deposition nucleation viewed as homogeneous or immersion freezing in pores and cavities, *Atmospheric Chemistry and Physics*, 14, 2071–2104, <https://doi.org/10.5194/acp-14-2071-2014>, 2014.



- Maruyama, K. I. and Fujiyoshi, Y.: Monte Carlo simulation of the formation of snowflakes, *Journal of the Atmospheric Sciences*, 62, 1529–1544, <https://doi.org/10.1175/JAS3416.1>, 2005.
- Mazloomi Moqaddam, A., Chikatamarla, S. S., and Karlin, I. V.: Simulation of Droplets Collisions Using Two-Phase Entropic Lattice Boltzmann Method, *Journal of Statistical Physics*, 161, 1420–1433, <https://doi.org/10.1007/s10955-015-1329-3>, 2015.
- 5 Milbrandt, J. A. and Morrison, H.: Parameterization of cloud microphysics based on the prediction of bulk ice particle properties. Part III: Introduction of multiple free categories, *Journal of the Atmospheric Sciences*, 73, 975–995, <https://doi.org/10.1175/JAS-D-15-0204.1>, 2016.
- Miller, T. L. and Young, K. C.: A Numerical Simulation of Ice Crystal Growth from the Vapor Phase, *Journal of the Atmospheric Sciences*, 36, 458–469, [https://doi.org/10.1175/1520-0469\(1979\)036<0458:ansoic>2.0.co;2](https://doi.org/10.1175/1520-0469(1979)036<0458:ansoic>2.0.co;2), 1979.
- 10 Misumi, R., Hashimoto, A., Murakami, M., Kuba, N., Orikasa, N., Saito, A., Tajiri, T., Yamashita, K., and Chen, J. P.: Microphysical structure of a developing convective snow cloud simulated by an improved version of the multi-dimensional bin model, *Atmospheric Science Letters*, 11, 186–191, <https://doi.org/10.1002/asl.268>, 2010.
- Mitchell, D. L.: Use of mass- and area-dimensional power laws for determining precipitation particle terminal velocities, *Journal of the Atmospheric Sciences*, 53, 1710–1723, [https://doi.org/10.1175/1520-0469\(1996\)053<1710:UOMAAD>2.0.CO;2](https://doi.org/10.1175/1520-0469(1996)053<1710:UOMAAD>2.0.CO;2), 1996.
- 15 Mitchell, D. L., Zhang, R., and Pitter, R. L.: Mass-dimensional relationships for ice particles and the influence of riming on snowfall rates, *Journal of Applied Meteorology*, 29, 153–163, [https://doi.org/10.1175/1520-0450\(1990\)029<0153:MDRFIP>2.0.CO;2](https://doi.org/10.1175/1520-0450(1990)029<0153:MDRFIP>2.0.CO;2), 1990.
- Morrison, H. and Grabowski, W. W.: A novel approach for representing ice microphysics in models: Description and tests using a kinematic framework, *Journal of the Atmospheric Sciences*, 65, 1528–1548, <https://doi.org/10.1175/2007JAS2491.1>, 2008.
- Morrison, H. and Grabowski, W. W.: An improved representation of rimed snow and conversion to graupel in a multicomponent bin microphysics scheme, *Journal of the Atmospheric Sciences*, 67, 1337–1360, <https://doi.org/10.1175/2010JAS3250.1>, 2010.
- Morrison, H. and Milbrandt, J. A.: Parameterization of cloud microphysics based on the prediction of bulk ice particle properties. Part I: Scheme description and idealized tests, *Journal of the Atmospheric Sciences*, 72, 287–311, <https://doi.org/10.1175/JAS-D-14-0065.1>, 2015.
- Mosimann, L., Weingartner, E., and Waldvogel, A.: An Analysis of Accreted Drop Sizes and Mass on Rimed Snow Crystals, *Journal of the Atmospheric Sciences*, 51, 1548–1558, [https://doi.org/10.1175/1520-0469\(1994\)051<1548:aaoads>2.0.co;2](https://doi.org/10.1175/1520-0469(1994)051<1548:aaoads>2.0.co;2), 1994.
- 25 Murray, B. J., O’Sullivan, D., Atkinson, J. D., and Webb, M. E.: Ice nucleation by particles immersed in supercooled cloud droplets, <https://doi.org/10.1039/c2cs35200a>, 2012.
- Murray, W. A. and List, R.: Freezing of Water Drops, *Journal of Glaciology*, 11, 415–429, <https://doi.org/10.3189/s0022143000022371>, 1972.
- 30 Nakaya, U.: *Snow Crystals : Natural and Artificial*, Harvard Univ. Press, 1954.
- Niedermeier, D., Shaw, R. A., Hartmann, S., Wex, H., Clauss, T., Voigtländer, J., and Stratmann, F.: Heterogeneous ice nucleation: Exploring the transition from stochastic to singular freezing behavior, *Atmospheric Chemistry and Physics*, 11, 8767–8775, <https://doi.org/10.5194/acp-11-8767-2011>, 2011.
- Niedermeier, D., Ervens, B., Clauss, T., Voigtländer, J., Wex, H., Hartmann, S., and Stratmann, F.: A computationally efficient description of heterogeneous freezing: A simplified version of the Soccer ball model, *Geophysical Research Letters*, 41, 736–741, <https://doi.org/10.1002/2013GL058684>, 2014.



- Niedermeier, D., Augustin-Bauditz, S., Hartmann, S., Wex, H., Ignatius, K., and Stratmann, F.: Can we define an asymptotic value for the ice active surface site density for heterogeneous ice nucleation?, *Journal of Geophysical Research*, 120, 5036–5046, <https://doi.org/10.1002/2014JD022814>, 2015.
- Niederreiter, H.: Quasi-Monte Carlo methods and pseudo-random numbers, *Bull. Amer. Math. Soc.*, 84, 957–1041, <https://projecteuclid.org:443/euclid.bams/1183541461>, 1978.
- Niehaus, J., Becker, J. G., Kostinski, A., and Cantrell, W.: Laboratory measurements of contact freezing by dust and bacteria at temperatures of mixed-phase clouds, *Journal of the Atmospheric Sciences*, 71, 3659–3667, <https://doi.org/10.1175/JAS-D-14-0022.1>, 2014.
- Niemand, M., Möhler, O., Vogel, B., Vogel, H., Hoose, C., Connolly, P., Klein, H., Bingemer, H., Demott, P., Skrotzki, J., and Leisner, T.: A particle-surface-area-based parameterization of immersion freezing on desert dust particles, *Journal of the Atmospheric Sciences*, 69, 3077–3092, <https://doi.org/10.1175/JAS-D-11-0249.1>, 2012.
- Nishizawa, S., Yashiro, H., Sato, Y., Miyamoto, Y., and Tomita, H.: Influence of grid aspect ratio on planetary boundary layer turbulence in large-eddy simulations, *Geoscientific Model Development*, 8, 3393–3419, <https://doi.org/10.5194/gmd-8-3393-2015>, 2015.
- Noh, Y., Oh, D., Hoffmann, F., and Raasch, S.: A cloud microphysics parameterization for shallow cumulus clouds based on Lagrangian cloud model simulations, *Journal of the Atmospheric Sciences*, 75, 4031–4047, <https://doi.org/10.1175/JAS-D-18-0080.1>, 2018.
- Okawa, D.: Improvement of the super-droplet method using recursive multiple collision algorithm, Master’s thesis, University of Hyogo, 2015.
- Onishi, R. and Seifert, A.: Reynolds-number dependence of turbulence enhancement on collision growth, *Atmospheric Chemistry and Physics*, 16, 12441–12455, <https://doi.org/10.5194/acp-16-12441-2016>, 2016.
- Ormel, C. W. and Spaans, M.: Monte Carlo Simulation of Particle Interactions at High Dynamic Range: Advancing beyond the Googol, *The Astrophysical Journal*, 684, 1291–1309, <https://doi.org/10.1086/590052>, 2008.
- O’Rourke, P. J.: Collective drop effects on vaporizing liquid sprays, Ph.d. thesis, Princeton University, 1981.
- Paoli, R., Hélie, J., and Poinot, T.: Contrail formation in aircraft wakes, *Journal of Fluid Mechanics*, 502, 361–373, <https://doi.org/10.1017/S0022112003007808>, 2004.
- Petters, M. D. and Kreidenweis, S. M.: A single parameter representation of hygroscopic growth and cloud condensation nucleus activity, *Atmospheric Chemistry and Physics*, 7, 1961–1971, <https://doi.org/10.5194/acp-7-1961-2007>, <http://www.atmos-chem-phys.net/7/1961/2007/>, 2007.
- Phillips, V. T., Pokrovsky, A., and Khain, A.: The influence of time-dependent melting on the dynamics and precipitation production in maritime and continental storm clouds, *Journal of the Atmospheric Sciences*, 64, 338–359, <https://doi.org/10.1175/JAS3832.1>, 2007.
- Phillips, V. T., Formenton, M., Bansemer, A., Kudzotsa, I., and Lienert, B.: A parameterization of sticking efficiency for collisions of snow and graupel with ice crystals: Theory and comparison with observations, *Journal of the Atmospheric Sciences*, 72, 4885–4902, <https://doi.org/10.1175/JAS-D-14-0096.1>, 2015.
- Phillips, V. T., Yano, J. I., and Khain, A.: Ice multiplication by breakup in ice-ice collisions. Part I: Theoretical formulation, *Journal of the Atmospheric Sciences*, 74, 1705–1719, <https://doi.org/10.1175/JAS-D-16-0224.1>, 2017.
- Pope, S. B.: Lagrangian PDF Methods for Turbulent Flows, *Annual Review of Fluid Mechanics*, 26, 23–63, <https://doi.org/10.1146/annurev.fl.26.010194.000323>, <http://www.annualreviews.org/doi/10.1146/annurev.fl.26.010194.000323>, 1994.
- Pruppacher, H. R. and Klett, J. D.: *Microphysics of clouds and precipitation*, Kluwer Academic Publishers, 1997.



- Przybylo, V. M., Sulia, K. J., Schmitt, C. G., Lebo, Z. J., and May, W. C.: The ice Particle and Aggregate Simulator (IPAS). Part I: Extracting dimensional properties of ice-ice aggregates for microphysical parameterization, *Journal of the Atmospheric Sciences*, 76, 1661–1676, <https://doi.org/10.1175/JAS-D-18-0187.1>, 2019.
- Rasmussen, R. and Pruppacher, H. R.: A wind tunnel and theoretical study of the melting behavior of atmospheric ice particles. I: a wind tunnel study of frozen drops of radius less than 500 micrometers., *Journal of the Atmospheric Sciences*, 39, 152–158, [https://doi.org/10.1175/1520-0469\(1982\)039<0152:AWTATS>2.0.CO;2](https://doi.org/10.1175/1520-0469(1982)039<0152:AWTATS>2.0.CO;2), 1982.
- Rasmussen, R. M. and Heymsfield, A. J.: A generalized form for impact velocities used to determine graupel accretional densities., *Journal of the Atmospheric Sciences*, 42, 2275–2279, [https://doi.org/10.1175/1520-0469\(1985\)042<2275:AGFFIV>2.0.CO;2](https://doi.org/10.1175/1520-0469(1985)042<2275:AGFFIV>2.0.CO;2), 1985.
- Rasmussen, R. M. and Heymsfield, A. J.: Melting and Shedding of Graupel and Hail. Part I: Model Physics, *Journal of the Atmospheric Sciences*, 44, 2754–2763, [https://doi.org/10.1175/1520-0469\(1987\)044<2754:masoga>2.0.co;2](https://doi.org/10.1175/1520-0469(1987)044<2754:masoga>2.0.co;2), 1987.
- Riechelmann, T., Noh, Y., and Raasch, S.: A new method for large-eddy simulations of clouds with Lagrangian droplets including the effects of turbulent collision, *New Journal of Physics*, 14, <https://doi.org/10.1088/1367-2630/14/6/065008>, 2012.
- Rogers, R. R. and Yau, M. K.: *A Short Course in Cloud Physics*, Butterworth-Heinemann, third edn., 1989.
- Roscoe, R.: XXXI. The flow of viscous fluids round plane obstacles, *The London, Edinburgh, and Dublin Philosophical Magazine and Journal of Science*, 40, 338–351, <https://doi.org/10.1080/14786444908561255>, <https://doi.org/10.1080/14786444908561255>, 1949.
- Sato, Y., Nishizawa, S., Yashiro, H., Miyamoto, Y., Kajikawa, Y., and Tomita, H.: Impacts of cloud microphysics on trade wind cumulus: which cloud microphysics processes contribute to the diversity in a large eddy simulation?, *Progress in Earth and Planetary Science*, 2, <https://doi.org/10.1186/s40645-015-0053-6>, 2015.
- Sato, Y., Shima, S.-i., and Tomita, H.: A grid refinement study of trade wind cumuli simulated by a Lagrangian cloud microphysical model: the super-droplet method, *Atmospheric Science Letters*, 18, 359–365, <https://doi.org/10.1002/asl.764>, 2017.
- Sato, Y., Shima, S.-i., and Tomita, H.: Numerical Convergence of Shallow Convection Cloud Field Simulations: Comparison Between Double-Moment Eulerian and Particle-Based Lagrangian Microphysics Coupled to the Same Dynamical Core, *Journal of Advances in Modeling Earth Systems*, 10, 1495–1512, <https://doi.org/10.1029/2018MS001285>, 2018.
- Schilling, V., Siano, S., and Etling, D.: Dispersion of aircraft emissions due to wake vortices in stratified shear flows: A two-dimensional numerical study, *Journal of Geophysical Research: Atmospheres*, 101, 20965–20974, <https://doi.org/10.1029/96JD02013>, <http://doi.wiley.com/10.1029/96JD02013>, 1996.
- Schmidt, D. P. and Rutland, C. J.: A New Droplet Collision Algorithm, *Journal of Computational Physics*, 164, 62–80, <https://doi.org/10.1006/jcph.2000.6568>, 2000.
- Schmitt, C. G. and Heymsfield, A. J.: The dimensional characteristics of ice crystal aggregates from fractal geometry, *Journal of the Atmospheric Sciences*, 67, 1605–1616, <https://doi.org/10.1175/2009JAS3187.1>, 2010.
- Scotti, A., Meneveau, C., and Lilly, D. K.: Generalized Smagorinsky model for anisotropic grids, *Physics of Fluids A: Fluid Dynamics*, 5, 2306–2308, <https://doi.org/10.1063/1.858537>, <http://aip.scitation.org/doi/10.1063/1.858537>, 1993.
- Seeßelberg, M., Trautmann, T., and Thorn, M.: Stochastic simulations as a benchmark for mathematical methods solving the coalescence equation, *Atmospheric Research*, 40, 33–48, [https://doi.org/10.1016/0169-8095\(95\)00024-0](https://doi.org/10.1016/0169-8095(95)00024-0), 1996.
- Seifert, A., Khain, A., Blahak, U., and Beheng, K. D.: Possible effects of collisional breakup on mixed-phase deep convection simulated by a spectral (bin) cloud model, *Journal of the Atmospheric Sciences*, 62, 1917–1931, <https://doi.org/10.1175/JAS3432.1>, 2005.
- Seifert, A., Leinonen, J., Siewert, C., and Kneifel, S.: The Geometry of Rimed Aggregate Snowflakes: A Modeling Study, *Journal of Advances in Modeling Earth Systems*, 11, 712–731, <https://doi.org/10.1029/2018MS001519>, 2019.



- Seiki, T. and Nakajima, T.: Aerosol effects of the condensation process on a convective cloud simulation, *Journal of the Atmospheric Sciences*, 71, 833–853, <https://doi.org/10.1175/JAS-D-12-0195.1>, 2014.
- Shaw, R. A., Durant, A. J., and Mi, Y.: Heterogeneous surface crystallization observed in undercooled water, *Journal of Physical Chemistry B*, 109, 9865–9868, <https://doi.org/10.1021/jp0506336>, 2005.
- 5 Shima, S., Kusano, K., Kawano, A., Sugiyama, T., and Kawahara, S.: The super-droplet method for the numerical simulation of clouds and precipitation: A particle-based and probabilistic microphysics model coupled with a non-hydrostatic model, *Quarterly Journal of the Royal Meteorological Society*, 135, 1307–1320, <https://doi.org/10.1002/qj.441>, 2009.
- Shima, S.-i., Hasegawa, K., and Kusano, K.: Preliminary numerical study on the cumulus-stratus transition induced by the increase of formation rate of aerosols, *Low Temperature Science*, 72, 249–264, <http://hdl.handle.net/2115/55063>, 2014.
- 10 Shirgaonkar, A. and Lele, S.: Large Eddy Simulation of Early Stage Contrails: Effect of Atmospheric Properties, in: 44th AIAA Aerospace Sciences Meeting and Exhibit, American Institute of Aeronautics and Astronautics, Reston, Virginia, <https://doi.org/10.2514/6.2006-1414>, <http://arc.aiaa.org/doi/10.2514/6.2006-1414>, 2006.
- Shupe, M. D., Daniel, J. S., de Boer, G., Eloranta, E. W., Kollias, P., Long, C. N., Luke, E. P., Turner, D. D., and Verlinde, J.: A focus on mixed-phase clouds, *Bulletin of the American Meteorological Society*, 89, 1549–1562, <https://doi.org/10.1175/2008BAMS2378.1>, 2008.
- 15 Smagorinsky, J.: GENERAL CIRCULATION EXPERIMENTS WITH THE PRIMITIVE EQUATIONS, *Monthly Weather Review*, 91, 99–164, [https://doi.org/10.1175/1520-0493\(1963\)091<0099:GCEWTP>2.3.CO;2](https://doi.org/10.1175/1520-0493(1963)091<0099:GCEWTP>2.3.CO;2), [https://doi.org/10.1175/1520-0493\(1963\)091{%}3C0099:GCEWTP{%}3E2.3.COhttp://0.0.0.2,1963](https://doi.org/10.1175/1520-0493(1963)091{%}3C0099:GCEWTP{%}3E2.3.COhttp://0.0.0.2,1963).
- Smoluchowski, M.: Drei Vorträge über Diffusion, Brownsche Molekularbewegung und Koagulation von Kolloidteilchen, *Physik. Z.*, 17, 557–571 (part I); 585–599 (part II), 1916.
- 20 Sölch, I. and Kärcher, B.: A large-eddy model for cirrus clouds with explicit aerosol and ice microphysics and Lagrangian ice particle tracking, *Quarterly Journal of the Royal Meteorological Society*, 136, 2074–2093, <https://doi.org/10.1002/qj.689>, 2010.
- Starr, D. O. and Cox, S. K.: Cirrus clouds. Part I: a cirrus cloud model., *Journal of the Atmospheric Sciences*, 42, 2663–2681, [https://doi.org/10.1175/1520-0469\(1985\)042<2663:CCPIAC>2.0.CO;2](https://doi.org/10.1175/1520-0469(1985)042<2663:CCPIAC>2.0.CO;2), 1985.
- Steinke, I., Hoose, C., Möhler, O., Connolly, P., and Leisner, T.: A new temperature- and humidity-dependent surface site density approach for deposition ice nucleation, *Atmospheric Chemistry and Physics*, 15, 3703–3717, <https://doi.org/10.5194/acp-15-3703-2015>, 2015.
- 25 Takahashi, T., Endoh, T., Wakahama, G., and Fukuta, N.: Vapor diffusional growth of free-falling snow crystals between -3 and -23 °C, *Journal of the Meteorological Society of Japan. Ser. II*, 69, 15–30, 1991.
- Ullrich, R., Hoose, C., Möhler, O., Niemand, M., Wagner, R., Höhler, K., Hiranuma, N., Saathoff, H., and Leisner, T.: A new ice nucleation active site parameterization for desert dust and soot, *Journal of the Atmospheric Sciences*, 74, 699–717, <https://doi.org/10.1175/JAS-D-16-0074.1>, 2017.
- 30 Unterstrasser, S. and Sölch, I.: Optimisation of the simulation particle number in a Lagrangian ice microphysical model, *Geoscientific Model Development*, 7, 695–709, <https://doi.org/10.5194/gmd-7-695-2014>, 2014.
- Unterstrasser, S., Hoffmann, F., and Lerch, M.: Collection/aggregation algorithms in Lagrangian cloud microphysical models: Rigorous evaluation in box model simulations, *Geoscientific Model Development*, 10, 1521–1548, <https://doi.org/10.5194/gmd-10-1521-2017>, 2017.
- 35 VanZanten, M. C., Stevens, B., Nuijens, L., Siebesma, A. P., Ackerman, A. S., Burnet, F., Cheng, A., Couvreux, F., Jiang, H., Khairoutdinov, M., Kogan, Y., Lewellen, D. C., Mechem, D., Nakamura, K., Noda, A., Shipway, B. J., Slawinska, J., Wang, S., and Wyszogrodzki, A.: Controls on precipitation and cloudiness in simulations of trade-wind cumulus as observed during RICO, *Journal of Advances in Modeling Earth Systems*, 3, <https://doi.org/10.1029/2011MS000056>, 2011.



- Vardiman, L.: The Generation of Secondary Ice Particles in Clouds by Crystal–Crystal Collision, *Journal of the Atmospheric Sciences*, 35, 2168–2180, [https://doi.org/10.1175/1520-0469\(1978\)035<2168:tgosip>2.0.co;2](https://doi.org/10.1175/1520-0469(1978)035<2168:tgosip>2.0.co;2), 1978.
- von Blohn, N., Diehl, K., Mitra, S. K., and Borrmann, S.: Riming of graupel: Wind tunnel investigations of collection kernels and growth regimes, *Journal of the Atmospheric Sciences*, 66, 2359–2366, <https://doi.org/10.1175/2009JAS2969.1>, 2009.
- 5 Wang, L. P., Ayala, O., Rosa, B., and Grabowski, W. W.: Turbulent collision efficiency of heavy particles relevant to cloud droplets, *New Journal of Physics*, 10, <https://doi.org/10.1088/1367-2630/10/7/075013>, 2008.
- Wang, P. K. and Ji, W.: Collision efficiencies of ice crystals at low-intermediate Reynolds numbers colliding with supercooled cloud droplets: A numerical study, *Journal of the Atmospheric Sciences*, 57, 1001–1009, [https://doi.org/10.1175/1520-0469\(2000\)057<1001:CEOICA>2.0.CO;2](https://doi.org/10.1175/1520-0469(2000)057<1001:CEOICA>2.0.CO;2), 2000.
- 10 Westbrook, C. D., Ball, R. C., Field, P. R., and Heymsfield, A. J.: Theory of growth by differential sedimentation, with application to snowflake formation, *Physical Review E - Statistical Physics, Plasmas, Fluids, and Related Interdisciplinary Topics*, 70, 7, <https://doi.org/10.1103/PhysRevE.70.021403>, 2004a.
- Westbrook, C. D., Ball, R. C., Field, P. R., and Heymsfield, A. J.: Universality in snowflake aggregation, *Geophysical Research Letters*, 31, <https://doi.org/10.1029/2004GL020363>, 2004b.
- 15 Westbrook, C. D., Hogan, R. J., and Illingworth, A. J.: The capacitance of pristine ice crystals and aggregate snowflakes, *Journal of the Atmospheric Sciences*, 65, 206–219, <https://doi.org/10.1175/2007JAS2315.1>, 2008.
- Wex, H., Demott, P. J., Tobo, Y., Hartmann, S., Rösch, M., Clauss, T., Tomsche, L., Niedermeier, D., and Stratmann, F.: Kaolinite particles as ice nuclei: Learning from the use of different kaolinite samples and different coatings, *Atmospheric Chemistry and Physics*, 14, 5529–5546, <https://doi.org/10.5194/acp-14-5529-2014>, 2014.
- 20 Wex, H., Augustin-Bauditz, S., Boose, Y., Budke, C., Curtius, J., Diehl, K., Dreyer, A., Frank, F., Hartmann, S., Hiranuma, N., Jantsch, E., Kanji, Z. A., Kiselev, A., Koop, T., Möhler, O., Niedermeier, D., Nillius, B., Rösch, M., Rose, D., Schmidt, C., Steinke, I., and Stratmann, F.: Intercomparing different devices for the investigation of ice nucleating particles using Snomax® as test substance, *Atmospheric Chemistry and Physics*, 15, 1463–1485, <https://doi.org/10.5194/acp-15-1463-2015>, 2015.
- Wicker, L. J. and Skamarock, W. C.: Time-splitting methods for elastic models using forward time schemes, *Monthly Weather Review*, 130, 2088–2097, [https://doi.org/10.1175/1520-0493\(2002\)130<2088:TSMFEM>2.0.CO;2](https://doi.org/10.1175/1520-0493(2002)130<2088:TSMFEM>2.0.CO;2), 2002.
- 25 Xue, L., Fan, J., Lebo, Z. J., Wu, W., Morrison, H., Grabowski, W. W., Chu, X., Geresdi, I., North, K., Stenz, R., Gao, Y., Lou, X., Bansemer, A., Heymsfield, A. J., McFarquhar, G. M., and Rasmussen, R. M.: Idealized simulations of a squall line from the MC3E field campaign applying three bin microphysics schemes: Dynamic and thermodynamic structure, *Monthly Weather Review*, 145, 4789–4812, <https://doi.org/10.1175/MWR-D-16-0385.1>, 2017.
- 30 Zalesak, S. T.: Fully multidimensional flux-corrected transport algorithms for fluids, *Journal of Computational Physics*, 31, 335–362, [https://doi.org/10.1016/0021-9991\(79\)90051-2](https://doi.org/10.1016/0021-9991(79)90051-2), 1979.
- Zsom, A. and Dullemond, C. P.: A representative particle approach to coagulation and fragmentation of dust aggregates and fluid droplets, *Astronomy and Astrophysics*, 489, 931–941, <https://doi.org/10.1051/0004-6361:200809921>, 2008.